JOSÉ AUGUSTO DE CARVALHO DIAS

Comportamento elástico e aeroelástico de estruturas eletromecânicas em casos de colheita de energia e controle de propriedades estruturais considerando não linearidades piezelétricas

São Carlos

2019

JOSÉ AUGUSTO DE CARVALHO DIAS

Comportamento elástico e aeroelástico de estruturas eletromecânicas em casos de colheita de energia e controle de propriedades estruturais considerando não linearidades piezelétricas

Tese apresentada à Escola de Engenharia de São Carlos da Universidade de São Paulo, como parte dos requisitos para obtenção do título de Doutor em Ciências.

Área de Concentração: Aeronaves

Orientador: Prof. Dr. Carlos De Marqui Junior
Co-Orientador: Prof. Dr. Alper Erturk

ESTE EXEMPLAR TRATA-SE DA VERSÃO CORRIGIDA. A VERSÃO ORIGINAL ENCONTRA-SE DISPONÍVEL JUNTO AO DEPARTAMENTO DE ENGENHARIA MECÂNICA DA EESC-USP.

São Carlos

2019

Ficha catalográfica elaborada pela Biblioteca Prof. Dr. Sérgio Rodrigues Fontes da EESC/USP com os dados inseridos pelo(a) autor(a).

de Carvalho Dias, José Augusto
83c Comportamento elástico e aeroelástico de estruturas eletromecânicas em casos de colheita de energia e controle de propriedades estruturais considerando não linearidades piezelétricas / José Augusto de Carvalho Dias; orientador Carlos De Marqui Júnior; coorientador Alper Erturk. São Carlos, 2019.

Tese (Doutorado) - Programa de Pós-Graduação em Engenharia Mecânica e Área de Concentração em Aeronáutica -- Escola de Engenharia de São Carlos da Universidade de São Paulo, 2019.

1. Vibrações mecânicas. 2. Aeroelasticidade. 3. Geração de energia. 4. Estrutura bio-inspirada. 5. Não linearidade piezelétrica. I. Título.

Eduardo Graziosi Silva - CRB - 8/8907

FOLHA DE JULGAMENTO

Candidato: Engenheiro **JOSÉ AUGUSTO DE CARVALHO DIAS.**

Título da tese: "Comportamento elástico e aeroelástico de estruturas eletromecânicas em casos de colheita de energia e controle de propriedades estruturais considerando não linearidades piezelétricas".

Data da defesa: 15/04/2019.

Comissão Julgadora:	**Resultado**:
Prof. Associado **Carlos de Marqui Junior** **(Orientador)** (Escola de Engenharia de São Carlos/EESC)	Aprovado
Prof. Dr. **Renato Pavanello** (Universidade Estadual de Campinas/UNICAMP)	APROVADO
Prof. Dr. **José Maria Campos ds Santos** (Universidade Estadual de Campinas/UNICAMP)	APROVADO
Prof. Dr. **Douglas Domingues Bueno** (Universidade Estadual Paulista "Júlio de Mesquita Filho"/UNESP – Ilha Solteira)	Aprovado
Prof. Dr. **Ricardo Afonso Angélico** (Escola de Engenharia de São Carlos/EESC)	Aprovado

Coordenador do Programa de Pós-Graduação em Engenharia Mecânica:
Prof. Associado **Carlos de Marqui Junior**

Presidente da Comissão de Pós-Graduação:
Prof. Titular **Murilo Araujo Romero**

To my family.

ACKNOWLEDGMENTS

First and foremost, I praise God Almighty for giving me the strength, knowledge, ability and opportunity to undertake this research study and to persevere and complete it satisfactorily. Without his blessings, this achievement would not have been possible.

I would like to thank to my wife Caroline for her patience, support, for her understanding and love during the past few years. Her support and encouragement was in the end what made this dissertation possible. My parents, Denise and Sidney, receive my deepest gratitude and love for their dedication and the many years of support during my undergraduate studies that provided the foundation for this work. To all my family, my safe harbor at all times, because without their constant faith in my capacities and their undying love I would not have come to be the person I am today. Thank you for supporting me even when everything seemed lost and I thought about giving up.

Special thanks to Dr. Carlos De Marqui Junior for his guidance, friendship and patience while supervising my graduate studies since 2011. His help is greatly appreciated. I would not have accomplished this dissertation without his able assistance and active direction. Many of the ideas in this study have been inspired by our conversations. Indeed he has been more than an advisor to me and I am proud to be a Ph.D. student under his guidance. I have had more than an advisor but an academic role model: hard-working, present, in touch with the current events, and more importantly, compassionate. No words can express fully how grateful I am for his help and friendship.

Thanks to the Department of Aeronautical Engineering at the São Carlos School of Engineering of the University of São Paulo. Thanks to all of the professors (in particular to Marcello Faraco, Volnei Tita, Ricardo Angélico and Marcelo Leite) and employees (Gisele, João, Cláudio, Iara and many others). Since undergraduate studies, they have directed my knowledge. However, far beyond teachers and staff, they are friends who provided my personal and academic growth. Many thanks to my laboratory friends Vagner, Tarcísio, Marcel, Douglas, Wander, Pagani, Gabriela, João and Gabriel.

I would like to thank to Dr. Alper Erturk, Associate Professor in the George W. Woodruff School of Mechanical Engineering at Georgia Institute of Technology (Atlanta, GA - USA), for receiving me in his lab during an year. I also would like to thank to all of his students that I had the opportunity of meeting there for being great lab-mates and friends during my staying at their lab.

Thanks to the University of São Paulo for allowing me to research in such a prestigious institution, since my undergraduate studies.

I would like to express my gratitude to many friends that believed in me, encouraged me and prayed for me throughout the time of my research.

This study was financed in part by the Coordenação de Aperfeiçoamento de Pessoal de Nível Superior - Brasil (CAPES) - Finance Code 001. I also would like to thank the São Paulo Research Foundation (FAPESP) who provided financial support for my PhD research project (grant number 2014/21827-3) and during my research internship abroad in United States (grant number 2016/13717-9) and to Conselho Nacional de Desenvolvimento Científico e Tecnológico (CNPq) for the initial financial support (grant number 141452/2014-5).

May the Almighty God richly bless all of you.

The greater our knowledge increases the more our ignorance unfolds.

John F. Kennedy

Resumo

DIAS, J. A. C. **Comportamento elástico e aeroelástico de estruturas eletromecânicas em casos de colheita de energia e controle de propriedades estruturais considerando não linearidades piezelétricas**. 2019. 131f. Doutorado – Escola de Engenharia de São Carlos, Universidade de São Paulo, São Carlos, 2019.

Diversos grupos de pesquisa têm investigado extensivamente materiais inteligentes ao longo das últimas décadas. As aplicações se estendem desde sensoriamento e atuação, assim como a combinação de ambos no controle de vibrações e mais recentemente em problemas de coleta de energia. Entre os diferentes materiais inteligentes disponíveis, os piezelétricos têm recebido grande atenção na literatura. Eles podem ser aplicados em uma grande e útil faixa de frequências sendo disponibilizados comercialmente em diversas configurações. Entre as diversas aplicações, a engenharia aeronáutica tem se beneficiado dos estudos relacionados aos materiais inteligentes. Em particular, estes materiais têm proporcionado avanços no desenvolvimento de estruturas bio-inspiradas, ou até mesmo o controle de propriedades estruturais da asa para aprimorar a performance aerodinâmica assim como na coleta de energia do escoamento. O equacionamento constitutivo linear da piezeletricidade foi considerado para a modelagem de tais sistemas na maioria dos casos. Entretanto, a literatura recente demonstra que manifestações não lineares de materiais piezelétricos são relevantes e podem significantemente modificar o comportamento do sistema eletromecanicamente acoplado em problemas de atuação e sensoriamento. Neste trabalho, um modelo de elementos finitos de placa não linear foi desenvolvido para obter as equações que governam o comportamento de sistemas eletromecanicamente acoplados. O modelo também considera o comportamento não linear de materiais piezelétricos em baixos campos elétricos. Os resultados do modelo eletroelástico não linear são verificados em relação a dados experimentais em casos de coleta de energia com excitação de base. Posteriormente, o modelo estrutural não linear é combinado a um modelo aerodinâmico não estacionário. Os efeitos da piezeletricidade não linear são investigados considerando uma asa flexível eletromecanicamente acoplada. A alteração ativa de rigidez induzida pela atuação piezelétrica também é investigada como uma técnica de controle aeroelástico.

Palavras-chave: Vibrações mecânicas. Aeroelasticidade. Geração de energia. Estrutura bio-inspirada. Não linearidade piezelétrica.

Abstract

DIAS, J. A. C. **Elastic and aeroelastic behavior of electromechanical coupled structures in cases of energy harvesting and structural control considering piezoelectric nonlinearities**. 2019. 131f. Tese (Doutorado) – Escola de Engenharia de São Carlos, Universidade de São Paulo, São Carlos, 2019.

Several research groups have extensively investigated smart materials over the last decades. Applications range from sensing and actuation, the combination of both in vibrations control and more recently, in energy harvesting problems. Among the different smart materials available, piezoelectric one has received great attention in the literature. They can be employed over a large and useful range of frequencies and different configurations are commercially available. Among different applications, aeronautical engineering has benefited from the researches related to smart materials. In particular, these materials have provided advances in the development of bio-inspired structures, control of structural properties in order to improve the aeroelastic performance as well as in wind energy harvesting. Linear constitutive equation of piezoelectricity has been considered in most cases for the modeling of such systems. However, recent literature shows that nonlinear manifestations of piezoelectric materials are relevant and can significantly modify the behavior of an electromechanically coupled system both in actuation or sensing problems. In this work, a nonlinear plate finite element model has been developed in order to obtain the governing equations of electromechanically coupled systems. The model also considers the nonlinear behavior piezoelectric material under weak electric fields. The nonlinear electroelastic model results are verified against experimental data in actuation and vibration based energy harvesting cases. Later, the nonlinear structural model is combined to an unsteady aerodynamic model. The effects of nonlinear piezoelectricity are investigated considering an electromechanically coupled flexible wing. The active stiffness change induced by piezoelectric actuation is also investigated as an aeroelastic control technique.

Keywords: Mechanical vibrations. Aeroelasticity. Energy harvesting. Bio-inspired structure. Piezoelectric nonlinearity.

List of Figures

List of Tables

Acronyms

SSDSL	Smart Structures and Dynamical Systems Laboratory, p. 33
MFC	Macro Fiber Composite, p. 35
NASA	National Aeronautics and Space Administration, p. 35
MEMS	Micro-electro-mechanical systems, p. 37
FEM	Finite element method, p. 49
DOF	Degree of freedom, p. 50
CFD	Computational fluid dynamics, p. 66
DVM	Discrete Vortex Method, p. 66
VPM	Vortex Particle Method, p. 66
VLM	Vortex lattice method, p. 67
DLM	Doublet lattice method, p. 67
WLL	Wagner Lifting Line, p. 67
PDV	Portable digital vibrometers, p. 75
FRF	Frequency response function, p. 76
ODE	Ordinary Differential Equation, p. 86
RVE	Representative volume element, p. 130

List of Symbols

T	Stress, p. 36
S	Strain, p. 37
E	Electric field, p. 37
c	Linear elastic constant, p. 37
e	Piezoelectric constant, p. 37
H	Electric enthalpy density, p. 37
U_{dis}	Energy dissipation per cycle, p. 38
$\lvert \quad \rvert$	Modulus or absolute operator, p. 38
L	Lagrangian, p. 45
T_{ke}	Kinetic energy density, p. 45
H	Electric enthalpy density, p. 45
δW	Virtual work, p. 45
ρ	Mass density, p. 46
$\dot{\mathbf{u}}$	Generalized velocity field, p. 46
T	Superscript denoting transpose, p. 46
$\mathbf{S}$	Strain vector, p. 46
$\mathbf{C}_p$	Piezoelectric elastic stiffness constants matrix, p. 46
$\mathbf{e}$	Piezoelectric constant matrix, p. 46
$\boldsymbol{\varepsilon}$	Electric permittivity constant matrix, p. 46
$\mathbf{E}$	Electric field vector, p. 46
E	Superscript denoting parameter measured at constant electric field, p. 46
S	Superscript denoting parameter measured at constant strain, p. 46
$\mathbf{f}$	Mechanical forces vector, p. 46
$\mathbf{q}$	Electric charge outputs vector, p. 46
$\boldsymbol{\phi}$	Electric potential outputs vector, p. 46
V	Volume of the element, p. 46
s	Subscripts denoting parameter related to the substructure, p. 46

p	Subscripts denoting parameter parameter related to the MFCs layers, p. 46
$\mathbf{u}$	Mechanical displacements vector, p. 46
$\mathbf{C}_s$	Substructure elastic stiffness constants matrix, p. 46
W_D	Work done by damping forces, p. 46
$\mathbf{C}_1$	Nonlinear elasticity matrix, p. 48
$\boldsymbol{\gamma}_{11}$	Nonlinear coupling matrix, p. 48
$\mathbf{I}$	Identity matrix, p. 48
α	Percentage of softening of the MFC stiffness, p. 48
β	Piezoelectric softening rate, p. 48
τ	Softening to strain ratio (negative), p. 48
$\mathbf{T}$	Stress vector, p. 48
$\mathbf{D}^e$	Electrical displacement, p. 48
u	Displacement in span direction, p. 50
v	Displacement in chord direction, p. 50
w	Perpendicular displacement to the reference plane, p. 50
z	Perpendicular level from the reference plane, p. 51
$\mathbf{P}$	Polynomial shape function terms, p. 52
$\boldsymbol{\mu}$	Generalized coordinates vector, p. 52
$\mathbf{u}$	Element degrees of freedom, p. 52
$\mathbf{A}$	Finite element transformation matrix, p. 52
$\mathbf{w}$	Nodal approximations for the transverse deflection, p. 52
$\boldsymbol{\Gamma}$	Element shape function, p. 52
$\mathbf{E}$	Electric field, p. 53
b_{mfc}	Distance between MFC electrodes, p. 53
v_p	Resultant voltage output across the load resistance, p. 53
R_l	Load resistance, p. 53
ϕ	Electric potential, p. 53
h_p	Thickness of the active layer, p. 53
$\mathbf{v}_p$	Voltage output vector across the load resistance, p. 54
$\mathbf{M}$	Global mass matrix, p. 54
$\mathbf{K}$	Global stiffness matrix, p. 54

$\boldsymbol{\Theta}$	Effective electromechanical coupling matrix, p. 54
$\mathbf{C}_{cap}$	Effective capacitance matrix, p. 55
$\mathbf{D}$	Global damping matrix, p. 55
$\mathbf{f_{ae}}$	Global aerodynamic force vector, p. 55
$\mathbf{f_{el}}$	Global mechanical force vector, p. 55
α^*	Damping proportional parameter related to mass matrix, p. 55
β^*	Damping proportional parameter related to stiffness matrix, p. 55
ne	Number of elements, p. 56
$\tilde{\boldsymbol{\Theta}}$	Reduced global coupling matrix, p. 56
$\tilde{\mathbf{C}}_{cap}$	Reduced global coupling matrix, p. 56
Ω	Element domain, p. 56
ξ	Natural coordinate on x direction, p. 57
η	Natural coordinate on x direction, p. 57
$\mathbf{J}$	Jacobian first order matrix, p. 57
$\mathrm{d}A$	Element area, p. 58
$\mathbf{J}_2$	Second order jacobian matrix, p. 59
$\mathbf{K}(\mathbf{u})$	Global nonlinear stiffness matrix, p. 60
$\boldsymbol{\Theta}(\mathbf{u})$	Global nonlinear coupling matrix, p. 60
$\mathbf{S}^p$	Deformation in plane , p. 62
$\mathbf{S}^b$	Curvature changes due to bending, p. 62
$\mathbf{u}_\alpha$	Nodal displacement parameters vector, p. 63
$\tilde{\mathbf{T}}$	Effective stress vector, p. 63
$\tilde{\mathbf{M}}$	Effective moment vector, p. 63
$\bar{\mathbf{B}}_\alpha$	Deformation matrix, p. 63
$\mathbf{K}_M$	Tangent stiffness matrix part related with the material, p. 64
$\bar{\mathbf{C}}$	Effective elasticity matrix, p. 64
$\mathbf{K}_M^L$	Stiffness coupling matrix between the membrane stiffness and the flexural strength, p. 64
$\mathbf{K}_G$	Tangent stiffness matrix part related with geometry, p. 65
$\mathbf{K}_T$	Tangent stiffness matrix, p. 65
Δp	Differential pressure, p. 68

V_∞	Freestream velocity, p. 68
ρ_∞	Air density, p. 68
A_w	Wing area, p. 68
Ke	Kernel function, p. 68
ω	Excitation frequency, p. 68
M	Mach number, p. 68
$\mathbf{AIC}$	Aerodynamic influence coefficients matrix, p. 68
$\mathbf{w_{wa}}$	Downwash vector, p. 68
G_{am}	Spline connecting aerodynamic and structural mesh, p. 69
G_{ma}	Spline connecting structural and aerodynamic mesh, p. 69
$\boldsymbol{\Phi}$	Modal shape matrix, p. 69
$\boldsymbol{\eta}$	Modal coordinates vector, p. 69
$\mathbf{X}_1$	Modal amplitudes vector, p. 69
$\mathbf{X}_2$	Modal amplitudes first time derivative vector, p. 69
$\mathbf{X}_S$	Aerodynamic lag state vector, p. 69
b	Semi-chord of the wing, p. 69
λ_{ae}	Lag aerodynamic root, p. 70

Content

CHAPTER
1

Introduction

The literature of energy harvesting exhibits a great number of papers reporting geometrically scalable and simple wind energy harvesters. The motivation is to power small electronic components employed in different engineering applications located in high wind areas by converting flow energy into usable electrical energy. While wind turbines are explored for large scale cases, the conversion of persistent flow induced oscillations of airfoils (ERTURK et al., 2010; SOUSA; JUNIOR, 2015; DIAS; JUNIOR; ERTURK, 2013; BAE; INMAN, 2014; ABDELKEFI; NAYFEH; HAJJ, 2012a, 2012d), elastic wings (De Marqui Junior; ERTURK; INMAN, 2010; JUNIOR et al., 2011; XIANG; WU; LI, 2015; BRUNI et al., 2017) or beams in axial flow (TANG; PAÏDOUSSIS; JIANG, 2009; DUNNMON et al., 2011; MICHELIN; DOARÉ, 2013; JUNIOR; TAN; ERTURK, 2018) by using the piezoelectric materials as transduction mechanism are among the linear aeroelastic energy harvesters concepts and configurations available in the literature.

The typical linear flutter behavior is well known from the classical literature of aeroelasticity (THEODORSEN, 1935; BISPLINGHOFF; ASHLEY; HALFMAN, 1996). Since persistent oscillations are observed only at the flutter boundary (linear flutter speed) in that scenario, the operation envelope of linear wind energy harvesters is limited to a single airflow speed. Nonlinear aeroelastic systems, on the other hand, can offer persistent oscillations over ranges of airflow speeds due to different sources of nonlinearities, such as the presence of concentrated or distributed structural nonlinearities and aerodynamic nonlinearities (DOWELL; TANG, 2002). Moreover, since real world applications often involve nonlinearities, there has been growing research interest in nonlinear aeroelastic energy harvesters over the past few years (ABDELKEFI; NAYFEH; HAJJ, 2012a; JUNIOR; TAN; ERTURK, 2018; SOUSA et al., 2011; ABDELKEFI; HAJJ, 2013; BAE; INMAN, 2014; SOUSA; JUNIOR, 2015; JAVED; DAI; ABDELKEFI, 2015) in order to overcome the limitations of linear aeroelastic energy harvesters.

The linear and nonlinear piezoaeroelastic wind energy harvesters discussed in the literature to date have considered the use of monolithic piezoelectric materials (using 31 mode of piezoelectricity) or piezoelectric fiber composites, such as Macro-Fiber Composites (using the 33 mode of piezoelectricity). In all cases, linear piezoelectric constitutive equations (IEEE, 1988) are taken into account during the derivation of the governing equations of linear as well as nonlinear wind energy harvesters. However, nonlinearities of piezoelectric materials have been observed in sensing and/or actuation cases as well as in energy harvesting applications, modifying significantly the dynamics of electroelastic structures (compared to the linear counterparts).

Most of the nonlinear modeling of piezoelectric materials has considered stiff and brittle monolithic piezoelectric materials, such as the geometrically linear and materially nonlinear framework presented by Leadenham and Erturk (2015) for energy harvesting, sensing and actuation. In previous studies in the literature dealing with electroelastic structures (AURELLE et al., 1996; ABDELKEFI; NAYFEH; HAJJ, 2012c; WOLF; GOTTLIEB, 2001; WAGNER; HAGEDORN, 2002; MAHMOODI; JALILI; DAQAQ, 2008; HU et al., 2006; GOLDSCHMIDTBOEING et al., 2011), piezoelectric nonlinearities were explored for separate problems of actuation or sensing and similar patterns of piezoelectric softening were related to different sources (nonlinear elasticity and nonlinear coupling simultaneously or separately). Leadenham and Erturk (2015) present a detailed review on piezoelectric nonlinearities. More recently, Tan, Yavarow and Erturk (2018) presented a geometrically and materially nonlinear framework for mechanical excitation of a MFC bimorph for nonlinear energy harvesting purposes. Simulations are compared to experimental results showing that the nonlinear model properly represented the experimentally observed nonlinear behavior.

The effects of nonlinear piezoelectricity on the piezoaeroelastic behavior of a generator wing for wind energy harvesting is investigated in this dissertation. The piezoaeroelastic model is obtained by combining an unsteady aerodynamic model with an electromechanically coupled nonlinear finite element (FE) model. The subsonic unsteady aerodynamic model is based on the Doublet-Lattice method (DLM) (ALBANO; RODDEN, 1969). The electromechanically coupled FE model considers the Von Karman plate theory that includes the Green-Lagrange Strain in the strain-displacement relation (although a linear version assuming the well-known Kirchhoff plate theory was also developed for reference solutions). The electromechanically coupled FE model also includes the nonlinear behavior of piezoelectric MFCs, being one of the contributions of the present work. First, the nonlinear FE model is validated against experimental results for an actuation case (actuation by the MFCs) as well as for a base excited MFC double bimorph. Later, the energy harvesting performance and the aeroelastic behavior of a nonlinear generator wing are investigated for a set of load resistances considering both the linear and nonlinear MFC models. This is the first wind energy harvesting investigation in the literature to take into account the effects of piezoelectric nonlinearity, a contribution of the present work. In the end, as an additional case study, the effects of active stiffness change (due to static actuation of MFC actuators on a plate-like wing) is investigated.

1.1 Content Overview

This dissertation presents the contents of a research project developed in the Laboratory of Aeroelasticity of Sao Carlos School of Engineering (University of Sao Paulo) and the Smart Structures and Dynamical Systems Laboratory (SSDSL) of Georgia Institute of Technology. In this chapter, an introduction and also the contributions of the present work are reported. Chapter 2 provides a literature review showing several researches on linear and nonlinear electroelastic structures.

Chapter 3 presents the modeling of the nonlinear aeroelectromechanically coupled system. In this chapter, the modeling of the linear and nonlinear coupled fields (aerodynamic, elastic and electric) are pointed out as well as the coupling mechanism between then.

Chapter 4 includes numerical and experimental results for electromechanically coupled structures. In this chapter the model is validated against nonlinear electroelastic actuation experimental results developed in this work and it is also validated against experimental energy harvesting data presented in the literature. Two different cases of wind energy harvesting are presented and the effects of piezoelectric nonlinearity on the electroaeroelastic behavior of wind energy harvesters are highlighted. The effects of active stiffness control due to in plane actuation of MFCs on the aeroelastic behavior of an electromechanically coupled plate-like wing is discussed.

Chapter 5 presents the final considerations. A brief review of the proposed model along with the most pertinent findings is presented. Suggestions for future work are also briefly discussed.

1.2 Objectives

The goal in this work is to investigate the effects of piezoelectric material nonlinearities on the behavior of electromechanically coupled systems considering piezoelectric actuation, piezoelectric sensing and energy harvesting cases. In particular, the effects of piezoelectric material nonlinearities on the behavior of electromechanically coupled flexible plates under wind excitation for energy harvesting is considered the main focus and motivation of this work. Therefore, a new expression for electric enthalpy density is presented to properly predict the nonlinear behavior of piezoelectric material. This expression, combined with a nonlinear Finite Element formulation, is employed in the Hamilton's principle to obtain the nonlinear equations of motion that are employed in the different cases explored in this work.

CHAPTER

2

Literature Review

Piezoelectric ceramics can be used for actuation and sensing over a wide range of frequencies. This type of material allows the conversion between electrical energy and mechanical energy (structural deformations). The conversion of mechanical into electric energy is due to the direct piezoelectric effect. The opposite conversion, that is, of electric energy into mechanical energy, is defined as the inverse piezoelectric effect. These materials have the ability to use simultaneous or separately the direct and reverse piezoelectric effects. Thus, the same structure composed of piezoelectric material can be used as a sensor and actuator simultaneously (ZHAO et al., 2010; WANG; INMAN, 2011; LEADENHAM; ERTURK, 2015). With this, the piezoelectric actuators have been applied to control vibrations, shape control, flow control, aeroelastic control, energy harvesting among other applications.

Although different types of piezoelectric ceramics (ranging from stack piezoelectric material to piezoceramic plates and discs) are available, the provided large forces with limited deformation are not suitable for certain applications. The Macro Fiber Composite (MFC) piezoelectric technology developed at the National Aeronautics and Space Administration (NASA) is a lightweight piezoelectric composite that consists of piezoelectric fibers (employing the 33-mode of piezoelectricity), interdigitated electrodes, epoxy, and Kapton layers. Over the last decades, MFCs have been investigated for various applications including sensing (SODANO; PARK; INMAN, 2004; MATT; SCALEA, 2007; CASTRO et al., 2017), energy harvesting (YANG; TANG; LI, 2009; MUDUPU et al., 2008; SHI; HALLETT; ZHU, 2017; TAN; YA-

VAROW; ERTURK, 2018), actuation (MUDUPU et al., 2008; KOVALOVS; BARKANOV; GLUHIHS, 2007; SAMUR, 2013; ZHOU; XU; YANG, 2019), and vibration control (COBB et al., 2009; ZIPPO et al., 2015). In addition to the advantages of the conventional piezoelectric actuators, MFCs also provide high strain and stress performance combined to flexibility, endurance and they are available in several sizes (fig. 1). In the next section, contributions of different authors to model piezoelectric nonlinearities of piezoceramics as well as of MFCs are reported and discussed.

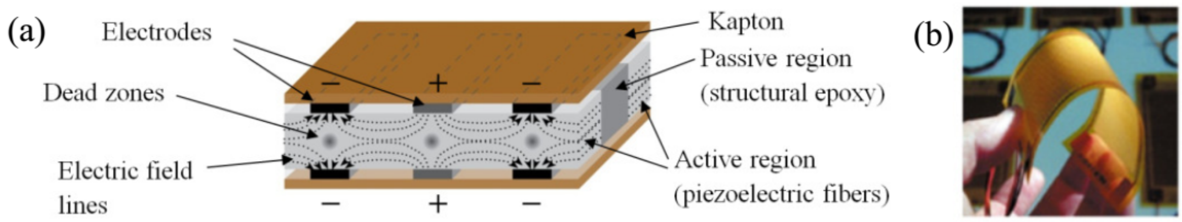

Figure 1 – (a) Schematic of the MFC structure and (b) a picture from the manufacturer (Smart Material Corp.) demonstrating its flexibility (SAMUR, 2013).

2.1 Piezoelectric material nonlinearity

It is important to note that nonlinearities of piezoelectric materials are manifested in several engineering applications including sensing and/or actuation, as well as their combined applications. Different authors have investigated the problems of nonlinear mechanical and electrical excitation (sensing and actuation, respectively) separately and the nonlinear resonance trends have been assumed to be due to different additional terms in the piezoelectric constitutive equations. Similar patterns of softening nonlinearities in electromechanical systems have been attributed by some authors to purely elastic nonlinear terms, electromechanical coupling nonlinearities, or both of these effects. After early investigation by Maugin (1986) and Tiersten (1993) into nonlinear electromechanical effects of piezoelectric materials, the nonlinear analysis of actuated piezoelectric beams started to gain momentum. Aurelle et al. (1996) studied the contribution of strain and electromechanical coupling to the nonlinear response of an actuated beam under low electric field excitation with stress T_1 modeled as,

$$T_1 = c_{11}S_1 - e_{31}E_3 + \alpha_{111}S_1^2 + \gamma_{311}S_1E_3, \tag{2.1}$$

where S is the strain, E is the electric field, c and e are the linear elastic and piezoelectric constants, and α and γ are the nonlinear constants. The subscript 1 and 3 stand for the length and transverse direction of the beam. The experimentally observed amplitude attenuation beyond the linear damping was attributed to the nonlinear electromechanical coupling term γ_{311}. Recently Abdelkefi, Nayfeh and Hajj (2012c, 2012b) used the constitutive equations suggested by (AURELLE et al., 1996) for nonlinear piezoelectric energy harvesting investigations.

Wolf and Gottlieb (2001) also attributed to elasticity the nonlinear phenomenon of a piezoelectric actuated cantilever in both symmetric (bimorph) and asymmetric (unimorph) configurations by considering an electric enthalpy density (H) defined as,

$$H = \frac{1}{2}c_{11}S_1^2 - e_{31}E_3S_1 - \frac{1}{2}\varepsilon_{33}E_3^2 + \frac{1}{6}c_3S_1^3 + \frac{1}{24}c_4S_1^4, \tag{2.2}$$

which results in second and third-order elastic dependence in the stress equation ($T = \partial H/\partial S$) related to c_3 and c_4 coefficients (depending on the symmetry with respect to the reference surface, bimorph or unimorph arrangement) along with a linear dependence on electric field and electromechanical coupling. Wagner and Hagedorn (2002) derived an electric enthalpy density formula to take into account quadratic and cubic nonlinearities of strain and coupling. The resulting electric enthalpy density expression was

$$H = \frac{1}{2}c_0S_1^2 + \frac{1}{3}c_1S_1^3 + \frac{1}{4}c_1S_1^4 - \gamma_0S_1E_3 - \frac{1}{2}\gamma_1S_1^2E_3 - \frac{1}{3}\gamma_2S_1^3E_3 - \frac{1}{2}\upsilon_2E_3^2, \tag{2.3}$$

where c_1, c_2, γ_1 and γ_2 are the nonlinear parameters. Also taking a purely geometric nonlinear approach, Mahmoodi, Jalili and Daqaq (2008) analyzed a micro-electro-mechanical (MEMS) piezoelectrically coupled cantilever that was validated by assuming low electric field and that material nonlinearities due to strain were an order of magnitude larger than coupling parameters.

Hu et al. (2006) analyzed the nonlinear behavior of a shear vibration piezoelectric energy harvester by applying the cubic theory of the displacement gradient initially introduced by Maugin (1986) and Tiersten (1993). Higher order electromechanical coupling and electric field terms were neglected due to the weak electric field assumption. Stanton et al. (2010a, 2010b) studied the results of higher order strain and electromechanical coupling and attributed experimentally shown peak attenuation at higher excitation levels to a nonlinear quadratic damping term. As an alternative to the model presented by Wagner and Hagedorn (2002) and Stanton et al. (2010a), Goldschmidtboeing et al. (2011) recently explored the effect of ferroelastic (stress-strain) hysteresis on piezoelectric cantilever beams. In their work, higher order nonlinear elasticity and nonlinear coupling terms were ignored, and the observed nonlinear effects were entirely attributed to hysteresis. These assumptions resulted in a constitutive equation and a per cycle energy dissipation U_{dis} relation, respectively, as

$$T_1 = c_{11}(1 - \alpha_{11}\,|S_1|)S_1 - e_{31}E_3 \tag{2.4}$$

$$U_{dis} = \frac{4}{3}\gamma c_{11}|S_1|^3, \tag{2.5}$$

where $|\quad|$ denotes the modulus, and α_{11} and γ are the parameters that quantify the hysteretic softening and dissipation effects. This model provided a single physical explanation for both the observed nonlinear stiffness and damping effects.

Due to the discrepancy within and between the actuation and sensing (including energy harvesting cases) analyses, Leadenham and Erturk (2015) presented a unified model of a piezoelectrically coupled beam using a nonlinear constitutive equation that is valid for both sensing and actuation cases (two-way coupling). The investigated system was a symmetric piezoelectric bimorph cantilever with two piezoelectric layers on either side of a metal central layer. The piezoelectric layers are poled in opposite directions, with the top and bottom surfaces forming the electrodes. The following nonlinear electric enthalpy density expression was employed along with a nonlinear structural energy dissipation,

$$H = \frac{1}{2}c_{11}S_1^2 + \frac{1}{3}c_{111}S_1^3\mathrm{sgn}(S_1) - e_{31}S_1E_3 - \frac{1}{2}e_{311}S_1^2\mathrm{sgn}(S_1)E_3 - \frac{1}{2}\varepsilon_{33}E_3^2 \qquad (2.6)$$

$$U_{dis} \propto |S_1|^3, \qquad (2.7)$$

which follows the works of Wagner and Hagedorn (2002) and Goldschmidtboeing et al. (2011). The common practice in the literature was to express the enthalpy as a polynomial in the strain and electric field. When using such a model to a symmetric structure, terms proportional to second order nonlinear coefficients vanish, resulting only in third order nonlinear terms to represent any nonlinear behavior. The electric enthalpy density presented by Leadenham is expressed as a polynomial in the strain magnitude. Therefore, second order terms do not vanish unlike the previous works presented in the literature (WAGNER; HAGEDORN, 2002). This fact is relevant since experimental data published in the literature show that electromechanically coupled systems exhibit first-order backbone curve (curve which connects the peaks of frequency response curves at all excitation amplitudes) trends (GOLDSCHMIDTBOEING et al., 2011; MAHMOODI; JALILI; DAQAQ, 2008) and, therefore, a model that does not allow second order stiffness and electromechanical coupling terms to vanish was required.

While both quadratic and cubic models can exhibit the same type of nonlinearities (hardening or softening), the two models are qualitatively different. This is apparent by examining the backbone curve of a nonlinear resonator displayed in figure 2. A quadratic model predicts a backbone curve that changes linearly with the response amplitude (figure 2(a), similar to the experimental results reported in the literature considering piezoelectric materials) while a cubic model predicts a quadratic variation of the peak response frequency with response amplitude.

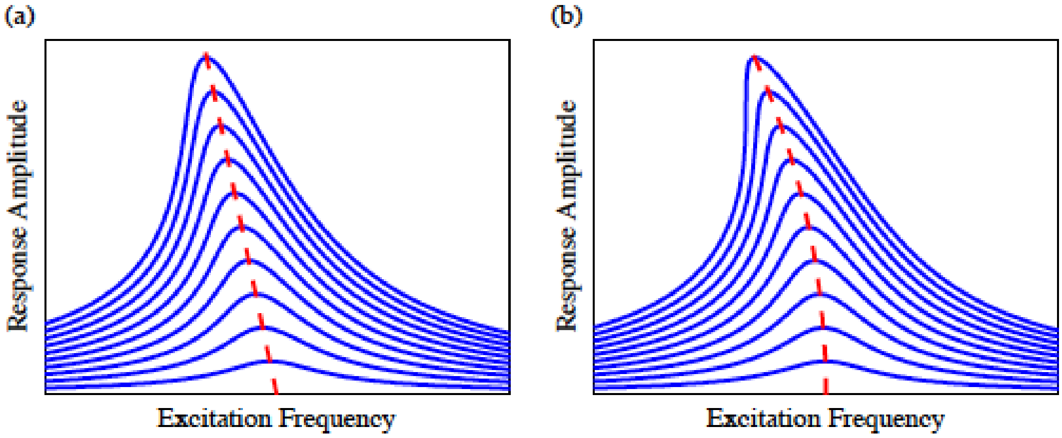

Figure 2 – Response of an oscillator with quadratic (a) and cubic (b) softening nonlinearity (LEADENHAM; ERTURK, 2015).

For the case of energy harvesting and sensing, the resulting nonlinear governing equations for an electromechanically coupled beam presented by Leadenham and Erturk (2015) are,

$$m\ddot{x}+d_1(\dot{x})+d_2(\dot{x})^2\mathrm{sgn}(\dot{x})+k_1x+k_2x^2\mathrm{sgn}(x)-[\theta_1+\theta_2\mathrm{sgn}(x)]\upsilon=-m\ddot{z}(t) \tag{2.8}$$

$$C\dot{\upsilon}+\frac{\upsilon}{R}+[\theta_1+\theta_2\mathrm{sgn}(\dot{x})]\dot{x}=0, \tag{2.9}$$

while the governing equations for the dynamic actuation case are,

$$m\ddot{x}+d_1(\dot{x})+d_2(\dot{x})^2\mathrm{sgn}(\dot{x})+k_1x+k_2x^2\mathrm{sgn}(x)=-[\theta_1+\theta_2\mathrm{sgn}(x)]\upsilon(t) \tag{2.10}$$

$$C\dot{\upsilon}+i+[\theta_1+\theta_2\mathrm{sgn}(\dot{x})]\dot{x}=0 \tag{2.11}$$

where d_1, k_1, and θ_1 are the linear damping, stiffness, and electromechanical coupling constants, respectively. The parameters d_2, k_2, and θ_2 represent the nonlinear damping, stiffness, and electromechanical coupling effects.

Figure 3 shows that the model presented by Leadenham and Erturk (2015) including stiffness, damping and electromechanical coupling nonlinearities predicts correctly the nonlinear experimental behavior of an electromechanically coupled beam in a base excitation problem (sensor) considering low to moderate base acceleration levels (Fig. 3a) and also predicts the experimental behavior in an actuation problem (Fig. 3b). Since low to moderate levels of excitation are considered in both cases, the nonlinear behavior is mostly due to the nonlinear behavior of the piezoelectric material, which is correctly represented from the proposed nonlinear enthalpy equation.

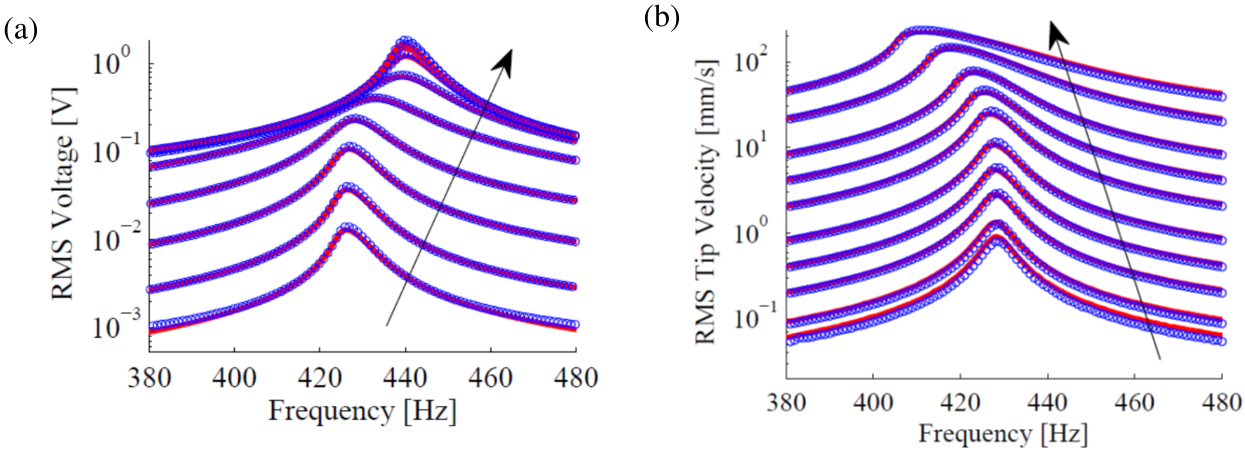

Figure 3 – Nonlinear (a) voltage output of the bimorph beam under harmonic base excitation ($0.1g$) for a range of load resistances and (b) tip velocity of the bimorph under dynamic actuation for voltage amplitudes ranging from $0.01V$ to $10V$. Blue circles are experimental data and red curves represent model predictions (LEADENHAM; ERTURK, 2015).

In a recent paper, Tan, Yavarow and Erturk (2018) studied the nonlinear behavior of a MFC bimorph cantilever under resonant base excitation for the primary resonance behavior. The nonlinearities considered by the researchers include a quadratic softening due to piezoelectric nonlinearity with cubic geometric hardening. Figure 4 shows that the model presented by Tan, Yavarow and Erturk (2018) predicts the nonlinear experimental behavior of an electromechanically coupled bimorph in low to moderate base acceleration levels. The damping and electromechanical coupling nonlinearities were neglected in their study. Taking this into consideration, the electric enthalpy density previously presented in the work of Leadenham and Erturk (2015) (equation 2.6) for the piezoelectric material (d_{33} mode) was simplified as,

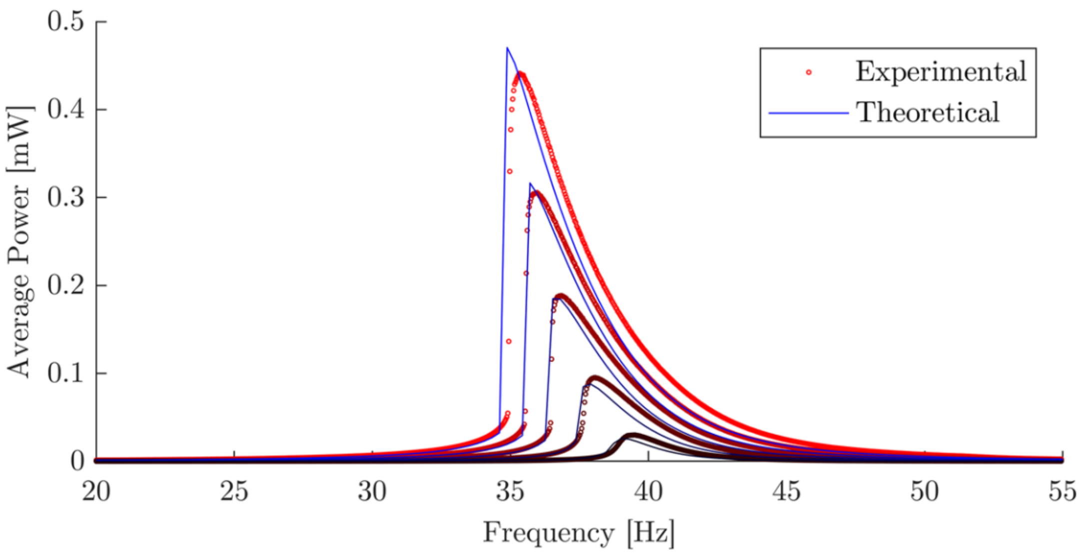

Figure 4 – Experimental and theorical average power at RMS base acceleration levels of $0.1g$, $0.2g$, $0.3g$, $0.4g$ and $0.5g$ using downward frequency sweep harmonic balance method (TAN; YAVAROW; ERTURK, 2018)

$$H = \frac{1}{2}c_{33}S_3^2 + \frac{1}{3}\gamma |S_3| S_3^2 - e_{33}S_3E_3 - \frac{1}{2}\varepsilon_{33}E_3^2 \tag{2.12}$$

where the subscript 3 stand for the length direction of the MFCs and γ is the nonlinear electric parameter that defines the backbone of the bimorph, which is not linear anymore. Furthermore, their experimental results show an opposite behavior from the oscillator with cubic softening (presented at figure 2b). Therefore, the researchers took into consideration two new terms in the nonlinear governing equations to account for nonlinear geometric hardening and the inertial softening. For the case of sensing, the resulting nonlinear governing equations for an electro-mechanically coupled beam presented by Tan, Yavarow and Erturk (2018) are,

$$m\ddot{w} + c\dot{w} + k\left(1-\gamma|w|\right)w + \frac{\alpha_1}{L^2}w^3 + \frac{\beta_1}{L^2}\left(w\dot{w}^2 + w^2\ddot{w}\right) - \theta_p \upsilon - \frac{\theta_{NL}}{\phi^2\left(L_m\right)}\upsilon w^2 = -m\ddot{z} \tag{2.13}$$

$$C_p\dot{\upsilon} + \frac{\upsilon}{R} + \frac{\theta_p}{\phi\left(L_m\right)}\dot{w} + \frac{\theta_{NL}}{\phi^3\left(L_m\right)}w^2\dot{w} = 0 \tag{2.14}$$

where α_1 and β_1 stand for the geometric hardening and the inertial softening coefficients, respectively, θ_{NL} is the nonlinear electromechanical coupling coefficient resulting from nonlinear strain. These parameters were then experimentally determined in order to reproduce the experimental nonlinear behavior displayed in figure 4.

2.1.1 Hysteresis

One of the major nonlinear phenomenon that occur on the analysis of piezoceramics is the hysteretic behavior exhibited by the material. The change of the polarization influences the piezoelectric effect, changing the coupling matrix, which also depends on the temperature, voltage and time. The temperature dependence can be neglected when temperature is roughly constant during the experiments. The time dependence is the creep that will be later discussed in this dissertation. The variation of electrical voltage, even considering small levels, changes the polarization of the piezoceramics. This change results in modified electromechanical coupling.

Several models in the literature take into account the physics of the hysteresis problem (SMITH; OUNAIES, 2000; SMITH et al., 2006; HASSANI; TJAHJOWIDODO; DO, 2014). Although these models are precise, they add a lot of complexity to the formulation. However, there is the possibility to describe mathematically the behavior of the hysteresis. Some of the available models include for example: Preisach, Prandtl-Ishlinskii and Maxwell slip models.

Another possibility is to assume a small, or even no hysteresis, in the actuation charge-strain relationship. (COMSTOCK, 1979) control the charge applied in the piezoceramics instead of the electrical voltage to reduce the hysteresis effects. In the present work, the focus is in the time analysis of the system and in the modulation at low frequencies. The aeroelectroelastic energy harvesting cases, presented in this work, are also exploited considering low frequency vibrations. Therefore, the hysteresis effects in the wing behavior will be neglected.

2.1.2 Depolarization

In the manufacturing process of piezoelectric ceramics, the material must be poled by applying high electric fields while the material is under high temperatures and, later, the material start to exhibit enhanced piezoelectric properties. In some cases, the electrical voltage of polarization is low, making the operational voltage even lower. If the operation of the piezoelectric material is out of the recommended range, the material polarization suddenly switch, as reported in Kushnir and Rabinovitch (2008) and Shindo et al. (2011). To prevent this type of nonlinearity, the domain of actuation must be between the maximum and minimum operational voltages. Once this condition is assured this type of nonlinearity can be neglected.

2.1.3 Creeping

Creep is a phenomenon related to the piezoelectric ceramic nature and its structure. When there is a change in the polarization in the ceramics, due to the ferroelectric domain, a change in the strain is observed. However, this change on the strain keeps happening even if the voltage does not change, meaning that the material will reach equilibrium later than expected. As mentioned before the coupling matrix, changes with the temperature, the voltage and time. Time constant of the creep decrease logarithmically with time and can go up to a hundred seconds (HUDEK, 2013).

For the actuation case of the present work creeping is really pronounced and influences in the final and transient form of the system (as observed during the experiments that will be later discussed). It was observed in almost all cases that the static actuation generates creeping during deformation and when the voltage is released, another creeping curve happens, and the final deformation is different from the initial deformation of the wing. This deeply influences the mechanical behavior of the electromechanically coupled system and deserves more detailed investigation in the future.

CHAPTER 3

Modeling of the nonlinear electromechanically coupled structure

In this work, the Finite Element method (REDDY, 2002; ZIENKIEWICZ; TAYLOR, 2000) is employed to model the piezoelastic coupled system. The method consists in a discretization of classical variational methods to smaller and simpler subdomains called finite elements. In this work, linear and nonlinear models of an electromechanically coupled plates were developed. The electroelastic finite element model is later combined to a DLM code developed in the research group in order to obtain the piezoaeroelastic model.

3.1 Electromechanically coupled plate formulation

The equations of motion of the coupled system are obtained from Hamilton's principle, which in the absence of electromagnetic field is defined as,

$$\delta \int_{t_0}^{t_1} \left(\int_V L dV \right) dt + \int_{t_0}^{t_1} \delta W dt = 0 \tag{3.1}$$

where L is the Lagrangian defined in terms of the kinetic energy (T_{ke}) and electrical enthalpy density (H) as $L = (T_{ke} - H)$, and δW is the virtual work due to external mechanical and electrical forces that will be later defined. The kinetic energy is

$$T_{ke} = \frac{1}{2}\rho \dot{\mathbf{u}}^{\mathrm{T}}\dot{\mathbf{u}} \tag{3.2}$$

where ρ is the mass density, and $\dot{\mathbf{u}}$ is the generalized velocity field. The superscript T stand for transpose. Assuming linear piezoelectricity (linear-electroelastic constitutive relation for the piezoceramic material) (IEEE, 1988), the enthalpy density is

$$H_{lin} = \frac{1}{2}\mathbf{S}^{\mathrm{T}}\mathbf{C}_p^{\mathrm{E}}\mathbf{S} - \mathbf{E}^{\mathrm{T}}\mathbf{e}\mathbf{S} - \frac{1}{2}\mathbf{E}^{\mathrm{T}}\boldsymbol{\varepsilon}^{\mathrm{S}}\mathbf{E} \tag{3.3}$$

where $\mathbf{S}$ is the strain vector, $\mathbf{C}_p$ is the matrix of piezoelectric elastic stiffness constants, $\mathbf{e}$ is the matrix of piezoelectric constants, $\boldsymbol{\varepsilon}$ is the matrix of electric permittivity constants, $\mathbf{E}$ is the electric field vector, the superscripts E and S denote that the parameters are measured at constant electric field and constant strain, respectively. The variation of mechanically applied work due to a set of discrete mechanical forces $\mathbf{f}$ and the variation of electrically extracted work for a set of discrete electric charge outputs $\mathbf{q}$, is presented as,

$$\delta W = \int_V \delta\mathbf{u}^{\mathrm{T}}\mathbf{f}\mathrm{d}V + \int_{V_p} \delta\boldsymbol{\phi}^{\mathrm{T}}\mathbf{q}\mathrm{d}V_p \tag{3.4}$$

where $\boldsymbol{\phi}$, is the vector of electrical potential, V is the volume of the element, subscripts $_s$ and $_p$ stand for the substructure and piezoceramic layers.

Using equations (3.2), (3.3), (3.4) and the linear enthalpy for the substructure, the generalized Hamilton's principle for a linear electromechanically coupled structure becomes

$$\begin{aligned}\int_{t_0}^{t_1} \Big[&- \int_{V_s} \delta\mathbf{S}^{\mathrm{T}}\mathbf{C}_s\mathbf{S}\mathrm{d}V_s - \int_{V_p} \delta\mathbf{S}^{\mathrm{T}}\left(\mathbf{C}_p^{\mathrm{E}}\mathbf{S} - \mathbf{e}^{\mathrm{T}}\mathbf{E}\right)\mathrm{d}V_p + \int_{V_p} \delta\mathbf{E}^{\mathrm{T}}\left(\mathbf{e}\mathbf{S} + \boldsymbol{\varepsilon}^{\mathrm{S}}\mathbf{E}\right)\mathrm{d}V_p \\ &+ \int_{V_s} \frac{1}{2}\rho_s\delta\mathbf{u}^{\mathrm{T}}\dot{\mathbf{u}}\mathrm{d}V_s + \int_{V_p} \frac{1}{2}\rho_p\delta\mathbf{u}^{\mathrm{T}}\dot{\mathbf{u}}\mathrm{d}V_p + \delta W + \delta W_D \Big] dt = 0\end{aligned} \tag{3.5}$$

where $\mathbf{u}$ is the vector of mechanical displacements, $\mathbf{C}_s$ is the matrix of substructure elastic stiffness constants and the over-dot represents differentiation with respect to time. δW_D denotes the work done by damping forces described as

$$\delta W_D = \int_V -\delta \mathbf{u}^{\mathrm{T}} \mathbf{D}_{Damp} \dot{\mathbf{u}} \mathrm{d}V \tag{3.6}$$

By assuming, for example, a finite element formulation equation (3.5) leads to the equation of motion of a linear electromechanically coupled system. Kirchhoff's plate theory is considered in this work for the linear behavior of the strain-displacement relation, as well as, the Von Karman plate theory which considers the Green-Lagrange Strain in the nonlinear behavior of the strain-displacement relation.

3.1.1 Nonlinear electric formulation

In this work, a plate model is combined with a nonlinear MFC model. The literature review presented in Section 2.1 of this dissertation shows that different authors discussed different modeling assumptions to represent the nonlinear behavior of electromechanically coupled system. Most of them discuss the modeling of electromechanically coupled beams considering piezoceramics. In the current work, a plate model is developed as well as the nonlinear behavior of MFCs is included, making the problem more complex than cases usually available in the literature. Several models based on deformation and electric field (when applied to symmetrical structures, as in a bimorph case) result in the cancelation of second order terms (LEADENHAM; ERTURK, 2015). This work proposes the modeling of the electric enthalpy density based on the deformation modulus. Although not reported here in details, several approaches were investigated in this work until the final solution was obtained.

Initially in this work, quadratic softening of piezoelectric material, as proposed by Leadenham and Erturk (2015), alongside with nonlinear geometric Von Karman model was assumed. However, in such case, the softening behavior is stronger for low strain levels and significantly reduced for larger strain levels. Therefore, under these assumptions, the model could not properly predict the experimental results for an electromechanically coupled flexible structure under bending and torsion actuation. Another approach was to model the enthalpy as a power function of the strain modulus, multiplying the linear term. Assuming the exponent of the power function as 0.25, the model could properly predict the experimental results for low strain levels (until 30V of bending actuation). For larger strain levels, piezoelectric softening was more significant than nonlinear geometric hardening and the numerical model failed to predict experiments. Therefore, a different approach is assumed, to properly predict the nonlinear piezoelectric material behavior, the enthalpy is modeled as an exponential function as

$$\begin{aligned} H_{nonl} =& \frac{1}{2}\mathbf{S}^{\mathrm{T}}\mathbf{C}_p^{\mathrm{E}}\mathbf{S} + \mathbf{S}^{\mathrm{T}}\mathbf{C}_1^{\mathrm{E}}\alpha\left\{\mathbf{I} - \mathrm{diag}\left[\exp\left(|\mathbf{S}|^{\beta}\tau\right)\right]\right\}\mathbf{S} \\ & -\mathbf{E}^{\mathrm{T}}\mathbf{e}\mathbf{S} - \frac{1}{2}\mathbf{E}^{\mathrm{T}}\boldsymbol{\gamma}_{11}\mathbf{S}\,|\mathbf{S}| - \frac{1}{2}\mathbf{E}^{\mathrm{T}}\boldsymbol{\varepsilon}^{\mathrm{S}}\mathbf{E} \end{aligned} \tag{3.7}$$

where $\mathbf{C}_1$ is the nonlinear elasticity matrix, $\boldsymbol{\gamma}_{11}$ the nonlinear quadratic coupling matrix, $\mathbf{I}$ the nonlinear quadratic coupling matrix, α is the percentage of softening of the MFC stiffness, β is the coefficient that regulates the piezoelectric softening with increasing strain and τ is the negative coefficient that regulates the maximum softening and strain relation.

To model the nonlinear behavior of the piezoelectric material, the enthalpy of equation (3.7) is adopted. This equation is already an expansion for the plate case. Through the compatibility relations ($\mathbf{T}_i = \partial H/\partial \mathbf{S}_i$ and $\mathbf{D}^e = -\partial H/\partial \mathbf{E}$), the stress vector $\mathbf{T}$ is defined as

$$\begin{aligned} \mathbf{T} =& \mathbf{C}_p^{\mathrm{E}}\mathbf{S} - \mathbf{e}^{\mathrm{T}}\mathbf{E} - \mathrm{diag}\left(|\mathbf{S}|\right)\boldsymbol{\gamma}_{11}{}^{\mathrm{T}}\mathbf{E} \\ & +2\mathbf{C}_1^{\mathrm{E}}\alpha\left\{\mathbf{I} - \mathrm{diag}\left[\exp\left(|\mathbf{S}|^{\beta}\tau\right)\right]\left[\mathbf{I} - \mathrm{diag}\left(\frac{1}{2}\beta\tau\mathbf{S}^2|\mathbf{S}|^{\beta-2}\right)\right]\right\}\mathbf{S} \end{aligned} \tag{3.8}$$

and the electrical displacement $\mathbf{D}^e$ is defined as

$$\mathbf{D}^{\mathbf{e}} = \mathbf{e}\mathbf{S} + \frac{1}{2}\boldsymbol{\gamma}_{11}\mathrm{diag}\left(|\mathbf{S}|\right)\mathbf{S} + \boldsymbol{\varepsilon}^{\mathrm{S}}\mathbf{E} \tag{3.9}$$

Considering the nonlinear (exponential) piezoelectric elasticity matrix ($\mathbf{C}_1$), in an approximation, equal to the half of the linear stiffness matrix and moderate strains, the stress vector given by equation (3.8) can be simplified as

$$\mathbf{T} = \mathbf{C}_p^{\mathrm{E}}\mathbf{S} - \mathbf{e}^{\mathrm{T}}\mathbf{E} - \mathrm{diag}\left(|\mathbf{S}|\right)\boldsymbol{\gamma}_{11}{}^{\mathrm{T}}\mathbf{E} + \mathbf{C}_p^{\mathrm{E}}\alpha\left\{\mathbf{I} - \mathrm{diag}\left[\exp\left(|\mathbf{S}|^{\beta}\tau\right)\right]\right\}\mathbf{S} \tag{3.10}$$

The generalized Hamilton's principle (equation 3.1) for the nonlinear case can be written as

$$
\begin{aligned}
\int_{t_0}^{t_1} \Bigg[& -\int_{V_p} \delta \mathbf{S}^{\mathrm{T}} \left(\mathbf{C}_p^{\mathrm{E}} \mathbf{S} + \mathbf{C}_p^{\mathrm{E}} \alpha \left\{ \mathbf{I} - \mathrm{diag} \left[\exp \left(|\mathbf{S}|^{\beta} \tau \right) \right] \right\} \mathbf{S} - \mathbf{S}\mathrm{diag}\left(|\mathbf{S}|\right) \boldsymbol{\gamma}_{11}{}^{\mathrm{T}} \mathbf{E} \right. \\
& \left. - \mathbf{e}^{\mathrm{T}} \mathbf{E} \right) \mathrm{d}V_p - \int_{V_s} \delta \mathbf{S}^{\mathrm{T}} \mathbf{C}_s \mathbf{S} \mathrm{d}V_s - \int_{V_p} \delta \mathbf{E}^{\mathrm{T}} \left(-\mathbf{e}\mathbf{S} - \frac{1}{2} \boldsymbol{\gamma}_{11} \mathbf{S}\mathrm{diag}\left(|\mathbf{S}|\right) - \boldsymbol{\varepsilon}^{\mathrm{S}} \mathbf{E} \right) \mathrm{d}V_p \\
& + \int_{V_s} \frac{1}{2} \rho_s \delta \mathbf{u}^{\mathrm{T}} \dot{\mathbf{u}} \mathrm{d}V_s + \int_{V_p} \frac{1}{2} \rho_p \delta \mathbf{u}^{\mathrm{T}} \dot{\mathbf{u}} \mathrm{d}V_p + \delta W + \delta W_D \Bigg] dt = 0
\end{aligned}
\tag{3.11}
$$

and the use of this equation (eq. 3.11) to obtain the nonlinear electric model of this work is discussed in subsection 3.3.1. First, the solution of the linear electroelastic equation (3.5) is obtained through Finite Element method presented next.

3.2 Finite Element Method

The Finite Element Method (FEM) models the structure to be analyzed by a finite number of structural elements known as finite elements that are interconnected by nodes where unknown quantities are defined (in the case of the electroelastic structure the unknowns are the displacement components and the electric potential defined by element). With these nodal variables it is possible to find a local solution for each element, where the equation is simpler than the global structure considering the more complex boundary conditions. These variables are defined by interpolation functions in order to map the nodal quantities along the element. Bhatti (2005) cites the following steps in applying the FEM to a problem:

- Develop equations for the element;
- Discretize the solution domain within a finite element mesh;
- Assemble the equations of the elements;
- Add the boundary conditions (physical and/or geometric constraints);
- Solve the problem for unknown nodes;

- Calculate the solution for each element.

Figure 5 shows the discretization in finite elements of the main structure that is modeled and studied in this work. It represents an elastic substructure, set along the nodes of the y-axis and with two pairs of piezoelectric material bimorphs (one macro fiber composite, MFC, on the upper and other in the lower surface of the substructure) near the sides of the plate (MFCs are represented in red in the figure). The MFCs layers are considered perfectly bonded to the elastic substructure and only the active area of the MFCs are considered in the model (the inactive Kapton layers surrounding the MFC are neglected). The electrodes are considered perfect conductors and the element properties are based on the mixing rules (Appendix B).

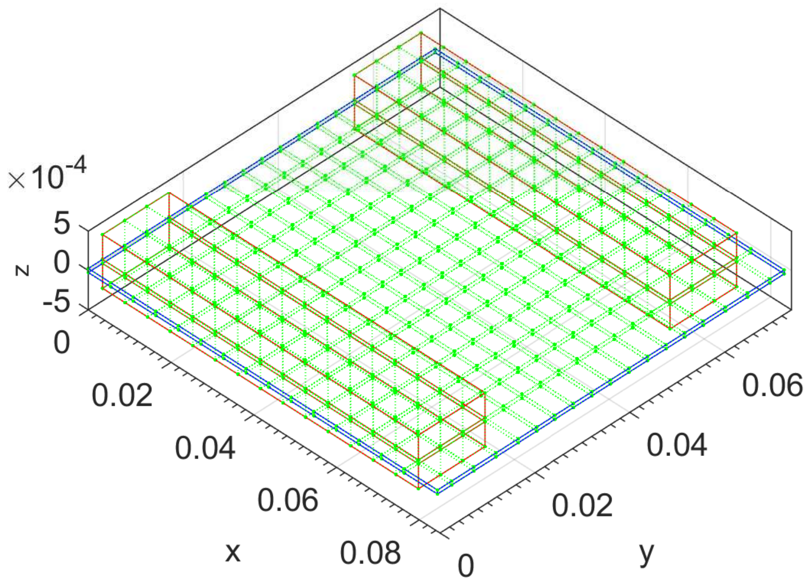

Figure 5 – Double bimorph wing finite element mesh

For the linear case, the classical theory of the Kirchhoff plate is used in the formulation as mentioned before. The linear finite element is represented by a rectangular plate-like element with four nodes at the ends and three degrees of freedom (DOF): u, v and w are the displacements in the x, y and z directions, respectively, and one electrical DOF (Figure 6).

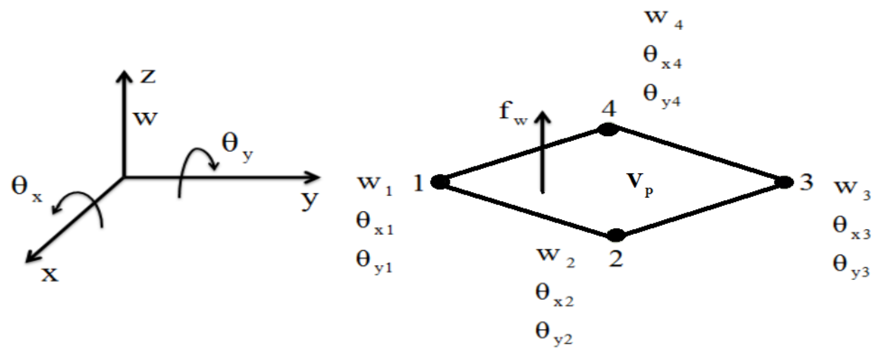

Figure 6 – Linear finite element with 12 mechanical degrees of freedom and 1 electrical degree of freedom

The shear deformations and rotational inertia of the finite elements are neglected based on Kirchhoff's plate theory, and the displacements in the plane (u and v) have their origin given only the rotation of the plate cross section (ZIENKIEWICZ; TAYLOR, 2000). Therefore, the displacement field can be described as:

$$\begin{Bmatrix} u \\ v \\ w \end{Bmatrix} = \begin{Bmatrix} -z\frac{\partial w}{\partial x} & -z\frac{\partial w}{\partial y} & w \end{Bmatrix}^{\mathrm{T}}, \tag{3.12}$$

where z is the perpendicular level to the plate from the reference plane, the deformations are described in nodal displacement terms as

$$\mathbf{S} = \begin{Bmatrix} \frac{\partial u}{\partial x} & \frac{\partial v}{\partial y} & \frac{\partial u}{\partial y} + \frac{\partial v}{\partial x} \end{Bmatrix}^{\mathrm{T}} = -z\begin{Bmatrix} \frac{\partial^2 w}{\partial x^2} & \frac{\partial^2 w}{\partial y^2} & 2\frac{\partial^2 w}{\partial x \partial y} \end{Bmatrix}^{\mathrm{T}} \tag{3.13}$$

The transverse displacement of the kth node of the finite element is described in the polynomial

$$w_k = w|_{x_k y_k} = \mathbf{P}|_{x_k y_k} \boldsymbol{\mu} \tag{3.14}$$

and the rotations in each kth node is given by

$$\theta_{xk} = \left.\frac{\partial w}{\partial y}\right|_{x_k y_k} = \left.\frac{\partial \mathbf{P}}{\partial y}\right|_{x_k y_k} \boldsymbol{\mu} \tag{3.15}$$

$$\theta_{yk} = \left.\frac{\partial w}{\partial x}\right|_{x_k y_k} = -\left.\frac{\partial \mathbf{P}}{\partial x}\right|_{x_k y_k} \boldsymbol{\mu} \tag{3.16}$$

where the polynomial terms, $\mathbf{P}$, are

$$\mathbf{P} = \left\{ \begin{array}{cccccccccccc} 1 & x & y & x^2 & xy & y^2 & x^3 & x^2y & xy^2 & y^3 & x^3y & xy^3 \end{array} \right\} \tag{3.17}$$

and the generalized coordinates vector, $\boldsymbol{\mu}$, is

$$\boldsymbol{\mu}^{\mathrm{T}} = \left\{ \begin{array}{cccccccccccc} a_1 & a_2 & a_3 & a_4 & a_5 & a_6 & a_7 & a_8 & a_9 & a_{10} & a_{11} & a_{12} \end{array} \right\} \tag{3.18}$$

The element DOFs $(\mathbf{u})$ (see figure 6) can be expressed as

$$\mathbf{u}^{\mathrm{T}} = \left\{ \begin{array}{cccccccccccc} w_1 & \theta_{x1} & \theta_{y1} & w_2 & \theta_{x2} & \theta_{y2} & w_3 & \theta_{x3} & \theta_{y3} & w_4 & \theta_{x4} & \theta_{y4} \end{array} \right\} \tag{3.19}$$

and

$$\mathbf{u} = \mathbf{A}\boldsymbol{\mu} \tag{3.20}$$

where $\mathbf{A}$ is the transformation matrix given by $\mathbf{P}$ and it derivatives. The nodal approximations for the transverse deflection as a function of the nodal variables, $\mathbf{w}$, are

$$\mathbf{w} \cong \mathbf{w}_k = \boldsymbol{\Gamma}\mathbf{u} \tag{3.21}$$

where $\boldsymbol{\Gamma}$ is the shape function defined as $\boldsymbol{\Gamma} = \mathbf{P}\mathbf{A}^{-1}$.

Thus the vector of transverse displacements and curvature vector can be described as

$$\left\{ \begin{array}{ccc} w & \frac{\partial w}{\partial y} & \frac{\partial w}{\partial x} \end{array} \right\}^{\mathrm{T}} = \mathbf{B}_{\eta}\mathbf{u} \tag{3.22}$$

$$\left\{ \begin{array}{ccc} 2\frac{\partial^2 w}{\partial x \partial y} & \frac{\partial^2 w}{\partial y^2} & \frac{\partial^2 w}{\partial x^2} \end{array} \right\}^{\mathrm{T}} = \mathbf{B}_{K}\mathbf{u} \tag{3.23}$$

where

$$\mathbf{B}_{\eta} = \left\{ \begin{array}{ccc} \mathbf{\Gamma} & \frac{\partial \mathbf{\Gamma}}{\partial y} & \frac{\partial \mathbf{\Gamma}}{\partial x} \end{array} \right\}^{\mathrm{T}} \tag{3.24}$$

$$\mathbf{B}_{K} = \left\{ \begin{array}{ccc} 2\frac{\partial^2 \mathbf{\Gamma}}{\partial x \partial y} & \frac{\partial^2 \mathbf{\Gamma}}{\partial y^2} & \frac{\partial^2 \mathbf{\Gamma}}{\partial x^2} \end{array} \right\}^{\mathrm{T}} \tag{3.25}$$

As the MFC (d_{33}) is polarized in the length direction, the non-zero component of the electric field (which is assumed uniform along the length) can be represented as,

$$\mathbf{E}_x = -\frac{\partial \phi}{\partial x} = -\frac{v_p}{b_{mfc}} \tag{3.26}$$

where $\mathbf{E}$ is the electric field, b_{mfc} is the distance between electrodes, v_p is the resultant voltage output across a load resistance (R_l) in each MFC electrical circuit and the electric potential ϕ, is assumed to vary linearly between the pairs of electrodes. An important point if piezoceramics or even d_{31} MFCs models are considered, is that the electrodes are considered alongside the thickness of the active layer changing b_{mfc} with h_p (thickness of the active layer) and the partial derivative will be in relation to the z instead of x (see eq. 3.26). In this way the electric field of the problem can be defined as:

$$\mathbf{E} = -\mathbf{B}_E v_p \tag{3.27}$$

where

$$\mathbf{B}_E = \left\{ \begin{array}{ccc} 0 & 0 & \frac{1}{b_{mfc}} \end{array} \right\}^{\mathrm{T}} \tag{3.28}$$

By combining the formulation presented in this section into the Hamilton's generalized principle, equation (3.5), one should obtain,

$$\begin{aligned}
&\delta W_{ext} + \mathbf{v}_p^{\mathrm{T}} \int_{V_p} q \mathrm{d}V_p = -\delta \mathbf{u}_i{}^{\mathrm{T}} \int_{V_p} z \mathbf{B}_K{}^{\mathrm{T}} \mathbf{e}^{\mathrm{T}} \mathbf{B}_E \mathbf{v}_p \mathrm{d}V_p + \delta W_D \\
&+ \delta \mathbf{u}_i{}^{\mathrm{T}} \int_{V_s} \left(\mathbf{B}_\eta{}^{\mathrm{T}} \mathbf{Z}^{\mathrm{T}} \rho_s \mathbf{Z} \mathbf{B}_\eta \ddot{\mathbf{u}}_i + z^2 \mathbf{B}_K{}^{\mathrm{T}} \mathbf{C}_s \mathbf{B}_K \mathbf{u}_i \right) \mathrm{d}V_s \\
&+ \delta \mathbf{u}_i{}^{\mathrm{T}} \int_{V_p} \left(\mathbf{B}_\eta{}^{\mathrm{T}} \mathbf{Z}^{\mathrm{T}} \rho_p \mathbf{Z} \mathbf{B}_\eta \ddot{\mathbf{u}}_i + z^2 \mathbf{B}_K{}^{\mathrm{T}} \mathbf{C}_p^{\mathrm{E}} \mathbf{B}_K \mathbf{u}_i \right) \mathrm{d}V_p \\
&- \mathbf{v}_p^{\mathrm{T}} \int_{V_p} \left(z \mathbf{B}_E{}^{\mathrm{T}} \mathbf{e} \mathbf{B}_K \mathbf{u} + \mathbf{B}_E{}^{\mathrm{T}} \boldsymbol{\varepsilon}^{\mathrm{S}} \mathbf{B}_E \mathbf{v}_p \right) \mathrm{d}V_p
\end{aligned} \tag{3.29}$$

when the linear elastic, linear MFC finite element formulation is considered. The resultant voltage output vector across the load resistances is represented as $\mathbf{v}_p$. In equation (3.29), $\mathbf{Z}$ is the matrix defined as

$$\mathbf{Z} = \begin{bmatrix} 1 & 0 & 0 \\ 0 & -z & 0 \\ 0 & 0 & -z \end{bmatrix} \tag{3.30}$$

Collecting the terms with $\delta \mathbf{u}_i{}^{\mathrm{T}}$, and $\mathbf{v}_p^{\mathrm{T}}$ equating these separately to zero yields to the element equations, where the element matrices are obtained from each term. The global equations of motion, obtained by assembling the element matrices, are given by

$$\mathbf{M}\ddot{\mathbf{u}} + \mathbf{D}\dot{\mathbf{u}} + \mathbf{K}\mathbf{u} - \boldsymbol{\Theta}\mathbf{v}_p = \mathbf{f_{ae}} + \mathbf{f_{el}} \tag{3.31}$$

$$\boldsymbol{\Theta}^{\mathbf{T}}\dot{\mathbf{u}} + \mathbf{C}_{cap}\dot{\mathbf{v}}_p + \frac{\mathbf{1}}{R_l}\mathbf{v}_p = \mathbf{0} \tag{3.32}$$

where $\mathbf{M}$ is the global mass matrix, $\mathbf{K}$ is the global stiffness matrix, $\boldsymbol{\Theta}$ is the effective electromechanical coupling matrix, $\mathbf{C}_{cap}$ is the effective capacitance matrix of the MFCs and $\mathbf{D}$ is the global damping matrix (assumed here as proportional to the mass and stiffness matrices). The right-hand-side terms $\mathbf{f_{ae}}$ and $\mathbf{f_{el}}$ are the global aerodynamic and mechanical (composed as the base excitation forces) force vectors.

The global motion matrices described above are obtained from the assembly of the elementary matrices given by equations (3.33)-(3.37).

$$\mathbf{M}_i = \int_{V_p} \mathbf{B}_\eta{}^{\mathrm{T}} \mathbf{Z}^{\mathrm{T}} \rho_p \mathbf{Z} \mathbf{B}_\eta \mathrm{d}V_p + \int_{V_s} \mathbf{B}_\eta{}^{\mathrm{T}} \mathbf{Z}^{\mathrm{T}} \rho_s \mathbf{Z} \mathbf{B}_\eta \mathrm{d}V_s \tag{3.33}$$

$$\mathbf{K}_i = \int_{V_p} z^2 \mathbf{B}_K{}^{\mathrm{T}} \mathbf{C}_p^{\mathrm{E}} \mathbf{B}_K \mathrm{d}V_p + \int_{V_s} z^2 \mathbf{B}_K{}^{\mathrm{T}} \mathbf{C}_s \mathbf{B}_K \mathrm{d}V_s \tag{3.34}$$

$$\mathbf{\Theta}_i = -\int_{V_p} z \mathbf{B}_K{}^{\mathrm{T}} \mathbf{e}^{\mathrm{T}} \mathbf{B}_E \mathrm{d}V_p \tag{3.35}$$

$$\mathbf{C}_{cap,i} = -\int_{V_p} \mathbf{B}_E{}^{\mathrm{T}} \boldsymbol{\varepsilon}^{\mathrm{S}} \mathbf{B}_E \mathrm{d}V_p \tag{3.36}$$

$$\mathbf{D}_i = \alpha^* \mathbf{M}_i + \beta^* \mathbf{K}_i \tag{3.37}$$

where α^* is the damping proportional parameter related to the mass matrix and β^* is the damping proportional parameter related to the stiffness matrix.

As the electrodes are considered conductive and continuous for each MFC/piezoceramic, the size of the electric output vector should be reduced to one per piezoelectric layer/MFC. In this way for each layer/MFC there is a transformation matrix considering all the elements of the vector $\mathbf{v}_p$ equal to

$$\mathbf{v}_p = \begin{Bmatrix} v_1 & v_2 & \cdots & v_{ne} \end{Bmatrix}^{\mathrm{T}} = \begin{Bmatrix} 1 & 1 & \cdots & 1 \end{Bmatrix}^{\mathrm{T}} v_p \tag{3.38}$$

where *ne* is the number of elements in the finite element mesh. Similarly is possible to calculate the overall coupling and the capacitance matrix for each piezoceramic layer/MFC as respectively

$$\tilde{\mathbf{\Theta}} = \left\{ \begin{array}{cccc} 1 & 1 & \cdots & 1 \end{array} \right\}^{\mathrm{T}} \mathbf{\Theta} \tag{3.39}$$

$$\tilde{\mathbf{C}}_{cap} = \sum\nolimits_{1}^{ne} \mathbf{C}_{cap} \tag{3.40}$$

where $\tilde{\mathbf{\Theta}}$ is the reduced global coupling matrix and $\tilde{\mathbf{C}}_{cap}$ is the reduced global capacitance matrix.

3.2.1 Isoparametric 4-node element for bending plates

Despite the explicit element formulation previously adopted in this work, only the CST (triangular well-known element) have been used in the literature to model nonlinearities explicitly. Taking this into consideration, the isoparametric element with similar formulation has been adopted. The element is presented in Zienkiewicz and Taylor (2000) and the basic formulation will be briefly discussed.

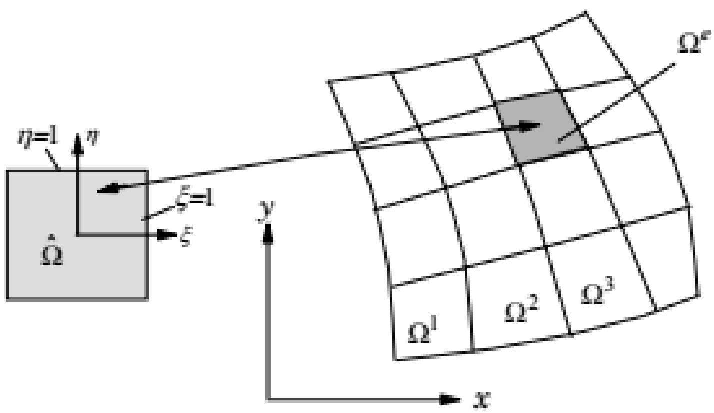

Figure 7 – Transformation of quadrilateral elements between natural and global coordinates (REDDY, 2002) where Ω, represents the element domain.

Before introducing the quadrilateral element, it is introduced the natural coordinate system for the geometry. The natural coordinates for a quadrilateral element are represented by ξ and η, illustrated in figure 7. The coordinates vary from -1 to 1 at both directions.

The shape functions (ZIENKIEWICZ; TAYLOR, 2000) are defined at the four nodes for the transverse displacement as:

$$\mathbf{\Gamma}_w = \begin{bmatrix} -\left((\eta-1)(\xi-1)\left(\eta^2+\eta+\xi^2+\xi-2\right)\right)/8 \\ \left((\eta-1)(\xi+1)\left(\eta^2+\eta+\xi^2-\xi-2\right)\right)/8 \\ \left((\eta+1)(\xi+1)\left(-\eta^2+\eta-\xi^2+\xi+2\right)\right)/8 \\ \left((\eta+1)(\xi-1)\left(\eta^2-\eta+\xi^2+\xi-2\right)\right)/8 \end{bmatrix} \tag{3.41}$$

and the rotational angles as

$$\mathbf{\Gamma}_{\theta x} = \begin{bmatrix} -\left((\eta-1)^2(\eta+1)(\xi-1)\right)/8 \\ \left((\eta-1)^2(\eta+1)(\xi+1)\right)/8 \\ \left((\eta-1)(\eta+1)^2(\xi+1)\right)/8 \\ -\left((\eta-1)(\eta+1)^2(\xi-1)\right)/8 \end{bmatrix} \tag{3.42}$$

$$\mathbf{\Gamma}_{\theta y} = \begin{bmatrix} \left((\xi-1)^2(\xi+1)(\eta-1)\right)/8 \\ \left((\xi-1)(\xi+1)^2(\eta-1)\right)/8 \\ -\left((\xi-1)(\xi+1)^2(\eta+1)\right)/8 \\ -\left((\xi-1)^2(\xi+1)(\eta+1)\right)/8 \end{bmatrix} \tag{3.43}$$

The shape functions are easily differentiated with respect to the natural coordinates, although the finite element calculations are with respect to the global coordinates. To solve this problem, chain rule of differentiation is used as

$$\left\{ \begin{array}{c} \frac{\partial \mathbf{\Gamma}}{\partial \xi} \\ \frac{\partial \mathbf{\Gamma}}{\partial \eta} \end{array} \right\} = \begin{bmatrix} \frac{\partial x}{\partial \xi} & \frac{\partial y}{\partial \xi} \\ \frac{\partial x}{\partial \eta} & \frac{\partial y}{\partial \eta} \end{bmatrix} \left\{ \begin{array}{c} \frac{\partial \mathbf{\Gamma}}{\partial x} \\ \frac{\partial \mathbf{\Gamma}}{\partial x} \end{array} \right\} = \mathbf{J} \left\{ \begin{array}{c} \frac{\partial \mathbf{\Gamma}}{\partial x} \\ \frac{\partial \mathbf{\Gamma}}{\partial x} \end{array} \right\} \tag{3.44}$$

where $\mathbf{J}$, is the first order Jacobian matrix of the transformation between both coordinates. Since it is easier to obtain the derivatives with respect to the natural coordinates, equation (3.44) can be rewritten as follows

$$\left\{ \begin{array}{c} \frac{\partial \mathbf{\Gamma}}{\partial x} \\ \frac{\partial \mathbf{\Gamma}}{\partial x} \end{array} \right\} = \mathbf{J}^{-1} \left\{ \begin{array}{c} \frac{\partial \mathbf{\Gamma}}{\partial \xi} \\ \frac{\partial \mathbf{\Gamma}}{\partial \eta} \end{array} \right\} \tag{3.45}$$

The integral over the transverse coordinate (z) remains the same and the element area ($\mathrm{d}A = \mathrm{d}x\mathrm{d}y$) is transformed to

$$\mathrm{d}A = |\mathbf{J}|\,\mathrm{d}\xi\mathrm{d}\eta \tag{3.46}$$

For the plate bending equations the second derivative with respect to the global coordinates is also required. The second-order Cartesian derivatives of the shape functions are given as

$$\begin{aligned}
\frac{\partial^2 \mathbf{\Gamma}}{\partial x^2} &= \frac{\partial^2 \mathbf{\Gamma}}{\partial \xi^2}\left(\frac{\partial \xi}{\partial x}\right)^2 + 2\frac{\partial^2 \mathbf{\Gamma}}{\partial \xi \partial \eta}\frac{\partial \xi}{\partial x}\frac{\partial \eta}{\partial x} + \frac{\partial^2 \mathbf{\Gamma}}{\partial \eta^2}\left(\frac{\partial \eta}{\partial x}\right)^2 + \frac{\partial \mathbf{\Gamma}}{\partial \xi}\frac{\partial^2 \xi}{\partial x^2} + \frac{\partial \mathbf{\Gamma}}{\partial \eta}\frac{\partial^2 \eta}{\partial x^2} \\
\frac{\partial^2 \mathbf{\Gamma}}{\partial y^2} &= \frac{\partial^2 \mathbf{\Gamma}}{\partial \xi^2}\left(\frac{\partial \xi}{\partial y}\right)^2 + 2\frac{\partial^2 \mathbf{\Gamma}}{\partial \xi \partial \eta}\frac{\partial \xi}{\partial y}\frac{\partial \eta}{\partial y} + \frac{\partial^2 \mathbf{\Gamma}}{\partial \eta^2}\left(\frac{\partial \eta}{\partial y}\right)^2 + \frac{\partial \mathbf{\Gamma}}{\partial \xi}\frac{\partial^2 \xi}{\partial y^2} + \frac{\partial \mathbf{\Gamma}}{\partial \eta}\frac{\partial^2 \eta}{\partial y^2} \\
\frac{\partial^2 \mathbf{\Gamma}}{\partial x \partial y} &= \frac{\partial^2 \mathbf{\Gamma}}{\partial \xi^2}\frac{\partial^2 \xi}{\partial x \partial y} + \frac{\partial^2 \mathbf{\Gamma}}{\partial \xi \partial \eta}\left(\frac{\partial \xi}{\partial x}\frac{\partial \eta}{\partial y} + \frac{\partial \xi}{\partial y}\frac{\partial \eta}{\partial x}\right) + \frac{\partial^2 \mathbf{\Gamma}}{\partial \eta^2}\frac{\partial^2 \eta}{\partial x \partial y} + \frac{\partial \mathbf{\Gamma}}{\partial \xi}\frac{\partial^2 \xi}{\partial x \partial y} + \frac{\partial \mathbf{\Gamma}}{\partial \eta}\frac{\partial^2 \eta}{\partial x \partial y}
\end{aligned} \tag{3.47}$$

Using the first order Jacobian matrix (3.44) it is possible to write,

$$\begin{aligned}
\frac{\partial}{\partial \xi}\left(\frac{\partial \eta}{\partial x}\right) &= \frac{\partial^2 \mathbf{\Gamma}}{\partial x^2}\frac{\partial x}{\partial \xi} + \frac{\partial^2 \mathbf{\Gamma}}{\partial x dy}\frac{\partial y}{\partial \xi} \\
\frac{\partial}{\partial \eta}\left(\frac{\partial \eta}{\partial x}\right) &= \frac{\partial^2 \mathbf{\Gamma}}{\partial x^2}\frac{\partial x}{\partial \eta} + \frac{\partial^2 \mathbf{\Gamma}}{\partial x dy}\frac{\partial y}{\partial \eta} \\
\frac{\partial}{\partial \xi}\left(\frac{\partial \eta}{\partial y}\right) &= \frac{\partial^2 \mathbf{\Gamma}}{\partial y^2}\frac{\partial y}{\partial \xi} + \frac{\partial^2 \mathbf{\Gamma}}{\partial x dy}\frac{\partial x}{\partial \xi} \\
\frac{\partial}{\partial \eta}\left(\frac{\partial \eta}{\partial y}\right) &= \frac{\partial^2 \mathbf{\Gamma}}{\partial y^2}\frac{\partial y}{\partial \eta} + \frac{\partial^2 \mathbf{\Gamma}}{\partial x dy}\frac{\partial x}{\partial \eta}
\end{aligned} \tag{3.48}$$

and solving the system equation (substituting the second-order Cartesian derivatives of the shape functions in this system of equations and considering a parallelogram element in the global coordinates), results in the second-order Cartesian derivatives as:

$$\left\{\begin{array}{c}\frac{\partial^2\mathbf{\Gamma}}{\partial\xi^2}\\\frac{\partial^2\mathbf{\Gamma}}{\partial\eta^2}\\\frac{\partial^2\mathbf{\Gamma}}{\partial\xi\partial\eta}\end{array}\right\}=\begin{bmatrix}\left(\frac{\partial x}{\partial\xi}\right)^2 & \left(\frac{\partial y}{\partial\xi}\right)^2 & 2\frac{\partial x}{\partial\xi}\frac{\partial y}{\partial\xi}\\\left(\frac{\partial x}{\partial\eta}\right)^2 & \left(\frac{\partial y}{\partial\eta}\right)^2 & 2\frac{\partial x}{\partial\eta}\frac{\partial y}{\partial\eta}\\\frac{\partial x}{\partial\xi}\frac{\partial x}{\partial\eta} & \frac{\partial y}{\partial\xi}\frac{\partial y}{\partial\eta} & \frac{\partial x}{\partial\xi}\frac{\partial y}{\partial\eta}+\frac{\partial x}{\partial\eta}\frac{\partial y}{\partial\xi}\end{bmatrix}\left\{\begin{array}{c}\frac{\partial^2\mathbf{\Gamma}}{\partial x^2}\\\frac{\partial^2\mathbf{\Gamma}}{\partial y^2}\\\frac{\partial^2\mathbf{\Gamma}}{\partial x\partial y}\end{array}\right\}=\mathbf{J}_2\left\{\begin{array}{c}\frac{\partial^2\mathbf{\Gamma}}{\partial x^2}\\\frac{\partial^2\mathbf{\Gamma}}{\partial y^2}\\\frac{\partial^2\mathbf{\Gamma}}{\partial x\partial y}\end{array}\right\} \tag{3.49}$$

where $\mathbf{J}_2$ is the second-order Jacobian matrix of the transformation between natural and global coordinates. Inverting this second order matrix, results

$$\left\{\begin{array}{c}\frac{\partial^2\mathbf{\Gamma}}{\partial x^2}\\\frac{\partial^2\mathbf{\Gamma}}{\partial y^2}\\\frac{\partial^2\mathbf{\Gamma}}{\partial x\partial y}\end{array}\right\}=\mathbf{J}_2^{-1}\left\{\begin{array}{c}\frac{\partial^2\mathbf{\Gamma}}{\partial\xi^2}\\\frac{\partial^2\mathbf{\Gamma}}{\partial\eta^2}\\\frac{\partial^2\mathbf{\Gamma}}{\partial\xi\partial\eta}\end{array}\right\} \tag{3.50}$$

These results can now be implemented in the shape functions (eq. 3.21) for the system matrices. The nonlinear finite element models (electric and geometric) can now be investigated with the implicit element presented.

3.3 Nonlinear modeling of the electromechanically coupled structure

3.3.1 Piezoelectric material nonlinearity

To model the nonlinear behavior of the piezoelectric material, the enthalpy of equation (3.7) is adopted. The generalized Hamilton's principle for the nonlinear electroelastic case, presented in equation (3.11), with the finite element formulation is modified to

$$
\begin{aligned}
&\delta W_{ext} + \mathbf{v}_p^{\mathrm{T}} \int_{V_p} q \mathrm{d}V_p = \delta W_D + \delta \mathbf{u}_i{}^{\mathrm{T}} \int_{V_s} \left(\mathbf{B}_\eta{}^{\mathrm{T}} \mathbf{Z}^{\mathrm{T}} \rho_s \mathbf{Z} \mathbf{B}_\eta \ddot{\mathbf{u}}_i + z^2 \mathbf{B}_K{}^{\mathrm{T}} \mathbf{C}_s \mathbf{B}_K \mathbf{u}_i \right) \mathrm{d}V_s \\
&+ \delta \mathbf{u}_i{}^{\mathrm{T}} \int_{V_p} \left(z^2 \mathbf{B}_K{}^{\mathrm{T}} \mathbf{C}_p^{\mathrm{E}} \mathbf{B}_K \mathbf{u}_i + \mathbf{B}_K \mathbf{C}_p^{\mathrm{E}} \alpha \left\{ \mathbf{I} - \mathrm{diag} \left[\exp \left(|\mathbf{S}|^\beta \tau \right) \right] \right\} \mathbf{B}_K \mathbf{u}_i \right. \\
&+ \mathbf{B}_\eta{}^{\mathrm{T}} \mathbf{Z}^{\mathrm{T}} \rho_p \mathbf{Z} \mathbf{B}_\eta \ddot{\mathbf{u}}_i - z \mathbf{B}_K{}^{\mathrm{T}} \mathbf{e}^{\mathrm{T}} \mathbf{B}_E \mathbf{v}_p - z \mathbf{B}_K{}^{\mathrm{T}} \mathrm{diag} \left(|\mathbf{S}| \right) \boldsymbol{\gamma}_{11}{}^{\mathrm{T}} \mathbf{B}_E \mathbf{v}_p \Big) \mathrm{d}V_p \\
&- \mathbf{v}_p^{\mathrm{T}} \int_{V_p} \left(\frac{1}{2} z \mathbf{B}_E{}^{\mathrm{T}} \boldsymbol{\gamma}_{11} \mathrm{diag} \left(|\mathbf{S}| \right) \mathbf{B}_K \mathbf{u}_i + z \mathbf{B}_E{}^{\mathrm{T}} \mathbf{e} \mathbf{B}_K \mathbf{u}_i + \mathbf{B}_E{}^{\mathrm{T}} \boldsymbol{\varepsilon}^{\mathrm{S}} \mathbf{B}_E \mathbf{v}_p \right) \mathrm{d}V_p
\end{aligned}
\tag{3.51}
$$

that in the same way of the linear case, equation (3.51) is written in a matrix form obtaining the same equation as the one obtained in the linear case (equations 3.31 and 3.32). However, the nonlinear stiffness matrix, $\mathbf{K}(\mathbf{u})$, and the nonlinear coupling matrix, $\boldsymbol{\Theta}(\mathbf{u})$, are defined in terms of their element matrices respectively as,

$$
\mathbf{K}_i(\mathbf{u}) = \int_{V_s} z^2 \mathbf{B}_K{}^{\mathrm{T}} \mathbf{C}_s \mathbf{B}_K \mathrm{dV_s} + \int_{V_p} z^2 \mathbf{B}_K{}^{\mathrm{T}} \mathbf{C}_p^{\mathrm{E}} \left(\mathbf{I} + \alpha \left\{ \mathbf{I} - \mathrm{diag} \left[\exp \left(|\mathbf{S}|^\beta \tau \right) \right] \right\} \right) \mathbf{B}_K \mathrm{dV_p} \tag{3.52}
$$

$$
\boldsymbol{\Theta}_i(\mathbf{u}) = - \int_{V_p} \left[z \mathbf{B}_K{}^{\mathrm{T}} \left(\mathbf{e}^{\mathrm{T}} + \mathrm{diag} \left(|\mathbf{S}| \right) \boldsymbol{\gamma}_{11}{}^{\mathrm{T}} \right) \mathbf{B}_E \right] \mathrm{dV}_p \tag{3.53}
$$

and the other terms (mass, capacitance and damping matrices) are described by the same way as in the linear case (equations 3.33, 3.36 and 3.37). Note that the matrices above (equations 3.52 and 3.53) depend on the solution of the problem itself. That is, the terms containing the nonlinear stiffness and the nonlinear coupling are dependent on the deformation, which is obtained only after solving the coupled equations. To solve the nonlinear equations, the Newton Raphson method is adopted (Appendix A).

3.3.2 Geometric nonlinearity

In this work, a nonlinear piezoelectrically coupled structure is considered in each case study. When displacements are moderately high over a plate, the interaction between the membrane and transverse displacement (due to the bending) should be considered. Therefore, a geometric nonlinear model is also included in the formulation.

In general, the physical nonlinearities of the material may occur due to large displacements or material behavior. Since flexible structures are considered in this work, the material remains in the linear elastic regime and the nonlinear elastic behavior is exclusively due to the geometric nonlinearity. In this way, this work also includes the development of a finite element model with geometric nonlinearity. The von Karman plate theory, which is valid for moderate displacements, is considered in the model formulation.

When the displacements are moderately large, then an interaction between the membrane and bending effects is initiated due to the transverse displacements. Karman (1910) first studied this effect. In Von Karman's theory, this effect is incorporated using a simplified form of the Green-Lagrange deformations obtained when the nonlinear terms associated with the components of the displacement in the in-plane directions, u_x and u_y, are neglected (CRISFIELD, 1997).

Considering the Green deformations,

$$\begin{aligned} S_{xx} &= \frac{\partial u}{\partial x} + \frac{1}{2}\left[\left(\frac{\partial u}{\partial x}\right)^2 + \left(\frac{\partial v}{\partial x}\right)^2 + \left(\frac{\partial w}{\partial x}\right)^2\right] \\ S_{yy} &= \frac{\partial v}{\partial y} + \frac{1}{2}\left[\left(\frac{\partial u}{\partial y}\right)^2 + \left(\frac{\partial v}{\partial y}\right)^2 + \left(\frac{\partial w}{\partial y}\right)^2\right] \\ S_{xy} &= \frac{1}{2}\left[\frac{\partial u}{\partial y} + \frac{\partial v}{\partial x} + \frac{\partial u}{\partial x}\frac{\partial u}{\partial y} + \frac{\partial v}{\partial x}\frac{\partial v}{\partial y} + \frac{\partial w}{\partial x}\frac{\partial w}{\partial y}\right] \end{aligned} \tag{3.54}$$

where the nonlinear terms couple the in-plane and out of plane displacements of the plate.

Considering the in-plane deformations, the displacement field becomes:

$$\left\{\begin{array}{c} u \\ v \\ w \end{array}\right\} = \left\{\begin{array}{c} u\,(x,y) \\ v\,(x,y) \\ w\,(x,y) \end{array}\right\} - z\left\{\begin{array}{c} w_{,x}\,(x,y) \\ w_{,y}\,(x,y) \\ 0 \end{array}\right\} \tag{3.55}$$

From this point, the next equations introduce a new notation, where the derivatives with respect to a variable are denoted in the subscript after the comma ($\partial * / \partial x \ = *_{,x}$).

Thus the deformation becomes:

$$\mathbf{S}_{Green} = \left\{ \begin{array}{c} S_{xx} \\ S_{yy} \\ 2S_{xy} \end{array} \right\} = \left\{ \begin{array}{c} u_{,x} + {w_{,x}}^2/2 \\ v_{,y} + {w_{,y}}^2/2 \\ u_{,y} + v_{,x} + w_{,x} w_{,y} \end{array} \right\} - z \left\{ \begin{array}{c} w_{,x^2} \\ w_{,y^2} \\ 2w_{,xy} \end{array} \right\} = \mathbf{S}^p - z\mathbf{S}^b \tag{3.56}$$

where $\mathbf{S}^p$ denotes the in plane deformation and $\mathbf{S}^b$ the curvature changes due to the bending. In this equation the quadratic terms with quadratic derivatives are neglected. The deformation variationals are:

$$\delta\mathbf{S}^p = \left\{ \begin{array}{c} \delta u_{,x} \\ \delta v_{,y} \\ \delta u_{,y} + \delta v_{,x} \end{array} \right\} + \begin{bmatrix} w_{,x} & 0 \\ 0 & w_{,y} \\ w_{,y} & w_{,x} \end{bmatrix} \left\{ \begin{array}{c} \delta w_{,x} \\ \delta w_{,y} \end{array} \right\} \tag{3.57}$$

$$\delta\mathbf{S}^b = \left\{ \begin{array}{c} \delta w_{,x^2} \\ \delta w_{,y^2} \\ 2\delta w_{,xy} \end{array} \right\} \tag{3.58}$$

The finite element approach for the geometrically nonlinear problem is developed based on the model for thin plate proposed by Zienkiewicz and Taylor (2000) adopting the Von Karman approximation of Green-Lagrange deformation. For the finite element model, it is possible to rewrite the deformation variationals as

$$\begin{aligned} \delta\mathbf{S}^p = \mathbf{B}^\alpha \delta\mathbf{u}_\alpha &= \begin{bmatrix} \mathbf{\Gamma}_{\alpha,x} & \mathbf{0} \\ \mathbf{0} & \mathbf{\Gamma}_{\alpha,y} \\ \mathbf{\Gamma}_{\alpha,y} & \mathbf{\Gamma}_{\alpha,x} \end{bmatrix} \left\{ \begin{array}{c} \delta u_\alpha \\ \delta v_\alpha \end{array} \right\} + \begin{bmatrix} w_{,x} & 0 \\ 0 & w_{,y} \\ w_{,y} & w_{,x} \end{bmatrix} \mathbf{G}_\alpha \left\{ \begin{array}{c} \delta w_\alpha \\ \delta\theta_{x\alpha} \\ \delta\theta_{y\alpha} \end{array} \right\} \\ &= \mathbf{B}_P^\alpha \delta\tilde{\mathbf{u}}_\alpha + \mathbf{B}_L^\alpha \delta\tilde{\mathbf{w}}_\alpha \end{aligned} \tag{3.59}$$

$$\delta\mathbf{S}^b = \begin{bmatrix} \mathbf{\Gamma}^w_{\alpha,xx} & \mathbf{\Gamma}^{\theta x}_{\alpha,xx} & \mathbf{\Gamma}^{\theta y}_{\alpha,xx} \\ \mathbf{\Gamma}^w_{\alpha,yy} & \mathbf{\Gamma}^{\theta x}_{\alpha,yy} & \mathbf{\Gamma}^{\theta y}_{\alpha,yy} \\ 2\mathbf{\Gamma}^w_{\alpha,xy} & 2\mathbf{\Gamma}^{\theta x}_{\alpha,xy} & 2\mathbf{\Gamma}^{\theta y}_{\alpha,xy} \end{bmatrix} \left\{ \begin{array}{c} \delta w_\alpha \\ \delta\theta_{x\alpha} \\ \delta\theta_{y\alpha} \end{array} \right\} = \mathbf{B}_K^\alpha \delta\tilde{\mathbf{w}}_\alpha \tag{3.60}$$

where

$$\mathbf{G}_{\alpha} = \begin{bmatrix} \mathbf{\Gamma}^{w}_{\alpha,x} & \mathbf{\Gamma}^{\theta x}_{\alpha,x} & \mathbf{\Gamma}^{\theta y}_{\alpha,x} \\ \mathbf{\Gamma}^{w}_{\alpha,y} & \mathbf{\Gamma}^{\theta x}_{\alpha,y} & \mathbf{\Gamma}^{\theta x}_{\alpha,y} \end{bmatrix} \tag{3.61}$$

with nodal displacement parameters $\mathbf{u}_{\alpha}$ defined as

$$\mathbf{u}^{\mathrm{T}}_{\alpha} = \begin{bmatrix} \left\{ \begin{matrix} u_{\alpha} & v_{\alpha} \end{matrix} \right\} & \left\{ \begin{matrix} w_{\alpha} & \theta_{x\alpha} & \theta_{y\alpha} \end{matrix} \right\} \end{bmatrix} = \begin{bmatrix} \tilde{\mathbf{u}}^{\mathrm{T}}_{\alpha} & \tilde{\mathbf{w}}^{\mathrm{T}}_{\alpha} \end{bmatrix} \tag{3.62}$$

Grouping the stresses $\tilde{\mathbf{T}}$ and moments $\tilde{\mathbf{T}}$ terms into one variable

$$\bar{\boldsymbol{\sigma}} = \left\{ \begin{matrix} \tilde{\mathbf{T}}^{p} \\ \tilde{\mathbf{M}}^{b} \end{matrix} \right\} \tag{3.63}$$

and the deformations matrices in one term $\left(\bar{\mathbf{B}}_{\alpha}\right)$ as

$$\bar{\mathbf{B}}_{\alpha} = \begin{bmatrix} \mathbf{B}^{\alpha}_{P} & \mathbf{B}^{\alpha}_{L} \\ \mathbf{0} & \mathbf{B}^{\alpha}_{K} \end{bmatrix} \tag{3.64}$$

the virtual work (δW) can be written as follow

$$\delta W = \delta \mathbf{u}^{\mathrm{T}}_{\alpha} \int_{V} \bar{\mathbf{B}}^{\mathrm{T}}_{\alpha} \bar{\boldsymbol{\sigma}} \mathrm{d}V - \delta W_{ext} = 0 \tag{3.65}$$

and the stiffness element matrix $\mathbf{K}_{i}\left(\mathbf{u}\right)$ for the substructure, considering the Green deformations in the stress strain relation, is defined as

$$\mathbf{K}_{i}\left(\mathbf{u}\right) = \int_{V_s} \bar{\mathbf{B}}^{\mathrm{T}}_{\alpha} \begin{bmatrix} \mathbf{C}_{s} & \mathbf{0} \\ \mathbf{0} & z^{2}\mathbf{C}_{s} \end{bmatrix} \bar{\mathbf{B}}_{\alpha} \mathrm{d}V_{s} \tag{3.66}$$

A tangent stiffness matrix is required for nonlinear formulation of the plate. Thus, the derivative of the virtual work is described as:

$$\mathrm{d}(\delta W) = \delta \mathbf{u}_{\alpha}^{\mathrm{T}} \int_{V_s} \left[\mathrm{d}\left(\bar{\mathbf{B}}_{\alpha}^{\mathrm{T}}\right) \bar{\boldsymbol{\sigma}} + \bar{\mathbf{B}}_{\alpha}^{\mathrm{T}} \mathrm{d}(\bar{\boldsymbol{\sigma}}) \right] \mathrm{d}V_s - \mathrm{d}(\delta W_{ext}) = 0 \tag{3.67}$$

and assuming, for simplicity, that the loading is conservative ($\mathrm{d}(\delta W_{ext}) = 0$) only a linearization of the deformation-displacement matrix and the strain-stress relationship is necessary. Considering linear elastic behavior, the relations of forces and deformations becomes:

$$\bar{\boldsymbol{\sigma}} = \left\{ \begin{array}{c} \tilde{\mathbf{T}}^p \\ \tilde{\mathbf{M}}^b \end{array} \right\} = \begin{bmatrix} \mathbf{C}_s & \mathbf{0} \\ \mathbf{0} & z^2\mathbf{C}_s \end{bmatrix} \left\{ \begin{array}{c} \mathbf{S}^p \\ \mathbf{S}^b \end{array} \right\} \tag{3.68}$$

and the tangent stiffness matrix part related with the material $\mathbf{K}_M$ is given by

$$\begin{aligned} (\mathbf{K}_M)_{\alpha\beta} &= \int_{V_s} \begin{bmatrix} (\mathbf{B}_P^{\alpha})^{\mathrm{T}} & \mathbf{0} \\ (\mathbf{B}_L^{\alpha})^{\mathrm{T}} & (\mathbf{B}_K^{\alpha})^{\mathrm{T}} \end{bmatrix} \begin{bmatrix} \mathbf{C}_s & \mathbf{0} \\ \mathbf{0} & z^2\mathbf{C}_s \end{bmatrix} \begin{bmatrix} \mathbf{B}_P^{\beta} & \mathbf{B}_L^{\beta} \\ \mathbf{0} & \mathbf{B}_K^{\beta} \end{bmatrix} \mathrm{d}V_s \\ &= \int_{V_s} \bar{\mathbf{B}}_{\alpha}^{\mathrm{T}} \bar{\mathbf{C}} \bar{\mathbf{B}}_{\beta} \mathrm{d}V_s = \begin{bmatrix} \left(\mathbf{K}_M^P\right)_{\alpha} & \left(\mathbf{K}_M^L\right)_{\alpha} \\ \left(\mathbf{K}_M^L\right)_{\alpha}^{\mathrm{T}} & \left(\mathbf{K}_M^K\right)_{\alpha} \end{bmatrix} \end{aligned} \tag{3.69}$$

where $\bar{\mathbf{C}}$ is the effective elasticity matrix, which in the case of the substructure is given by

$$\bar{\mathbf{C}}_s = \begin{bmatrix} \mathbf{C}_s & \mathbf{0} \\ \mathbf{0} & z^2\mathbf{C}_s \end{bmatrix} \tag{3.70}$$

and note that the tangent matrix is composed by the terms obtained from small displacements assumption (linear case) except to the coupling between the membrane stiffness and the flexural strength, $\mathbf{K}_M^L$. It is necessary to linearize the geometric part of equation, in this way

$$\mathrm{d}\left(\bar{\mathbf{B}}_{\alpha}^{\mathrm{T}}\right)\bar{\boldsymbol{\sigma}}=\mathrm{d}(\mathbf{B}_L^{\alpha})^{\mathrm{T}}\tilde{\mathbf{T}}^{p}=\mathbf{G}_{\alpha}^{\mathrm{T}}\begin{bmatrix}\mathrm{d}(w_{,x}) & 0 & \mathrm{d}(w_{,y})\\ 0 & \mathrm{d}(w_{,y}) & \mathrm{d}(w_{,x})\end{bmatrix}\begin{Bmatrix}T_x\\ T_y\\ T_{xy}\end{Bmatrix}$$
$$=\mathbf{G}_{\alpha}^{\mathrm{T}}\begin{bmatrix}T_x & T_{xy}\\ T_{xy} & T_y\end{bmatrix}\begin{Bmatrix}\mathrm{d}(w_{,x})\\ \mathrm{d}(w_{,y})\end{Bmatrix} \tag{3.71}$$

thus the geometric part of the tangent matrix, $\mathbf{K}_G$, is defined as

$$\left(\mathbf{K}_G^L\right)_{\alpha\beta}=\int_{V_s}\mathbf{G}_{\alpha}^{\mathrm{T}}\begin{bmatrix}T_x & T_{xy}\\ T_{xy} & T_y\end{bmatrix}\mathbf{G}_{\beta}\mathrm{d}V_s \quad \text{and} \quad (\mathbf{K}_G)_{\alpha\beta}=\begin{bmatrix}\mathbf{0} & \mathbf{0}\\ \mathbf{0} & \left(\mathbf{K}_G^L\right)_{\alpha\beta}\end{bmatrix} \tag{3.72}$$

and this way, the tangent stiffness matrix, $\mathbf{K}_T$, is defined as:

$$\mathbf{K}_T=(\mathbf{K}_M)_{\alpha\beta}+(\mathbf{K}_G)_{\alpha\beta} \tag{3.73}$$

The electric model (linear or nonlinear) can be easily coupled with the presented model. To solve the nonlinear equations for the elastic or electroelastic cases, the Newton Raphson method (Appendix A) is adopted. This geometrically nonlinear model is associated with the nonlinear constitutive behavior of piezoelectric material, obtained from the nonlinear enthalpy (previously presented), in the next subsection.

3.3.3 Nonlinear resultant formulation

The nonlinear geometric stiffness matrix can also be evaluated in the regions of an electro-mechanically coupled system covered with MFC similarly as developed for the substructure in section 3.3.2. The geometrically nonlinear model presented can be associated with the nonlinear constitutive behavior of piezoelectric material, obtained from the nonlinear enthalpy (previously presented). The resultant nonlinear electroelastic stiffness element matrix is defined as

$$\mathbf{K}_i(\mathbf{u}) = \int_{V_s} \bar{\mathbf{B}}_\alpha^{\mathrm{T}} \begin{bmatrix} \mathbf{C}_s & \mathbf{0} \\ \mathbf{0} & z^2\mathbf{C}_s \end{bmatrix} \bar{\mathbf{B}}_\alpha \mathrm{d}V_s + \int_{V_p} \bar{\mathbf{B}}_\alpha^{\mathrm{T}} \begin{bmatrix} \mathbf{C}^* & \mathbf{0} \\ \mathbf{0} & z^2\mathbf{C}^* \end{bmatrix} \bar{\mathbf{B}}_\alpha \mathrm{d}V_p \tag{3.74}$$

where $\mathbf{C}^* = \mathbf{C}_p^{\mathrm{E}} \left(\mathbf{I} + \alpha \left\{\mathbf{I} - \mathrm{diag}\left[\exp\left(|\mathbf{S}|^\beta \tau\right)\right]\right\}\right)$ and the nonlinear coupling element matrix is defined as

$$\boldsymbol{\Theta}_i = -\int_{V_p} \bar{\mathbf{B}}_\alpha^{\mathrm{T}} \left(\mathbf{e}^{\mathrm{T}} + \mathrm{diag}\left(|\mathbf{S}|\right) \boldsymbol{\gamma}_{11}{}^{\mathrm{T}}\right) \bar{\mathbf{B}}_E \mathrm{d}V_p \tag{3.75}$$

where $\bar{\mathbf{B}}_E = \begin{bmatrix} 1/b_{mfc} & 0 & 0 & 0 & z/b_{mfc} \end{bmatrix}^{\mathrm{T}}$ which agrees to the nodal displacement vector order displayed in equation 3.62.

Therefore, an accurate representation of the problem investigated in this work is obtained. The electroelastic models developed so far are employed in this work to investigate the electroelastic behavior of electromechanically coupled structures considering linear and also nonlinear piezoelectricity. As previously defined, one of the goals is to investigate the effects of piezoelectric material nonlinearity on the behavior of wind energy harvesters. Therefore, the electroelastic models have to be combined to unsteady aerodynamic model, which is discussed in the next section.

3.4 Fluid-Structure interaction

As well as finite elements methods in the structural area, numerical simulations have also been used extensively in fluid mechanics. The Computational Fluid Dynamics (CFD) has been developed greatly over the last decades since the data processing equipment becoming faster and cheaper. Several methods have been derived to analyze the flow, some of these are based on discrete vortex (DVM - Discrete Vortex Method). The Vortex Particle Method (VPM) is similarly developed and is similar to the DVM because it uses a discretization in particles, or characteristics of them, having in common the principle of development of the theory being the vortex. However, computational efficiency is reduced compared to a simpler linear method such as the Vortex Lattice Method (VLM) and the Doublet Lattice Method (DLM).

Boutet and Dimitriadis (2018) presented Wagner lifting line (WLL) method to model the incompressible, attached, unsteady lift and pitching moment acting on a thin three-dimensional wing in the time domain. The model is the result of the combination of Wagner theory and lifting line theory through the unsteady Kutta Joukowski theorem. The linear method proposed was compared to VLM and lift line theory for rectangular plates showing good agreement with VLM method. The proposed method have lower computational effort when compared to the VLM method.

Considering the computational cost and the use of the method in dynamic unsteady oscillations analyzes, the DLM is chosen to represent the aerodynamic in the simulations of this work. Before further analysis of the proposed aerodynamic model, it is emphasized that the structural and aerodynamic models are treated separately, and the coupling between them is later discussed.

3.4.1 Doublet Lattice Method

The linearized formulation for the oscillatory, inviscid, subsonic lifting surface theory relates the normal velocity at the surface of a body (*e.g.*, an elastic wing) with the aerodynamic loads caused by the pressure distribution (ALBANO; RODDEN, 1969). The formulation is derived using the unsteady Euler equations of the surrounding fluid. The doublet singularity or a sheet of doublets is a solution of the aerodynamic potential equation. Unsteady aerodynamic loads as well as the resultant differential pressure across the surface of a wing can be represented with this solution.

The relation between the differential pressure across the surfaces and the velocity normal to the surface of a wing is given by a Kernel function (ALBANO; RODDEN, 1969). The Kernel function is a closed-form solution of the integro-differential equation based on the assumption of harmonic motion. The velocity field normal to the surface of a wing is given by the equation

$$\bar{w}(x,y,z) = \frac{-1}{4V_\infty \pi \rho_\infty} \int\int_{A_w} \Delta p(x,y,z)\, Ke(x-\xi, y-\eta, z)\, d\xi d\eta \tag{3.76}$$

where $\Delta p(x,y,z)$ is the differential pressure, V_∞ is the freestream velocity, ρ_∞ is the air density, and ξ and η are dummy variables of integration over the wing area A_w in the spanwise (x) and chordwise (y) directions, respectively. The transverse direction is represented as z, while Ke is the Kernel function given as

$$Ke(x-\xi, y-\eta, z) = \exp\left(\frac{-j\omega(x-\xi)}{V_\infty}\right) \frac{\partial^2}{\partial z^2} \left\{ \frac{1}{\bar{R}} \exp\left[\frac{j\omega}{V_\infty \ell^2}(\lambda - M\bar{R})\right] d\lambda \right\} \tag{3.77}$$

where $\ell^2 = 1 - M^2$ and $\bar{R} = \sqrt{(x-\xi)^2 + (y-\eta)^2 + z^2}$, ω is the excitation frequency, M is the Mach number, and λ is a dummy variable.

The DLM provides an approximated solution for the Kernel function. The wing is represented by a thin lifting surface divided into a number of elements (panels or boxes) associated with doublet singularities. The singularities have constant strength in the chordwise direction and parabolic strength in the spanwise direction. A line of doublets distribution of acceleration potential is assumed at the $1/4$ chord line of each panel, which is equivalent to a pressure jump across the surface. A control point, where the boundary condition is verified, is defined in the half span of each element at the $3/4$ chord line. The strengths of the oscillating potential placed at the $1/4$ chord lines are the unknowns of the problem.

The downwash, introduced by the lifting lines, is assumed to be harmonic and is checked at each control point. Integration over the surface gives the local and the total aerodynamic force coefficients (ALBANO; RODDEN, 1969). The solution of the resulting matrix equation is

$$\mathbf{f_{ae}} = \mathbf{AIC}^{-1}(\omega)\, \mathbf{w_{wa}} \tag{3.78}$$

where $\mathbf{AIC}^{-1}(\omega)$ is the matrix of aerodynamic influence coefficients (related to the Kernel function) at a specific frequency (ω) and $\mathbf{w_{wa}}$ is the downwash vector described in terms of the plate transversal displacement ($\mathbf{w}$) and freestream velocity (V_∞) as

$$\mathbf{w_{wa}} = \frac{\partial \mathbf{w}}{\partial t} + V_\infty \frac{\partial \mathbf{w}}{\partial x} \tag{3.79}$$

3.4.2 Aeroelastic coupling

The aerodynamic and the structural dynamics are obtained from distinct numerical methods with distinct meshes. Therefore, transformation matrices are determined using a surface spline scheme in order to interpolate the forces obtained in the doublet lattice mesh to the nodes of the FE mesh (HARDER; DESMARAIS, 1972). Therefore, the aerodynamic forces are evaluated as

$$\mathbf{f}(\omega) = \mathbf{\Phi}^{\mathrm{T}} G_{ma} \mathbf{AIC}^{-1} \left(\frac{\partial}{\partial t} + V_\infty \frac{\partial}{\partial \mathbf{x}} \right) G_{am} \mathbf{\Phi} \boldsymbol{\eta} \tag{3.80}$$

where G_{am} and G_{ma} are the splines connecting aerodynamic mesh and structural mesh, $\mathbf{\Phi}$ is the modal shape matrix and $\boldsymbol{\eta}$ is the modal coordinates vector.

The aerodynamic forces are converted from the frequency domain to the time domain by using the Roger's approximation method (ROGER, 1977). The method uses a minimum square approximation to obtain a rational polynomial formulation described in time domain to represent the aerodynamic forces, and subsequently the piezoaeroelastic coupled equations can be represented in the state-space form as

$$\begin{Bmatrix} \dot{\mathbf{X}}_1 \\ \dot{\mathbf{X}}_2 \\ \dot{\mathbf{v}}_p \\ \dot{\mathbf{X}}_S \end{Bmatrix} = \begin{bmatrix} \mathbf{0} & \mathbf{I} & \mathbf{0} & \mathbf{0} \\ -\bar{\mathbf{M}}_{ae}^{-1}\bar{\mathbf{K}}_{ae}(\mathbf{u}) & -\bar{\mathbf{M}}_{ae}^{-1}\bar{\mathbf{D}}_{ae} & \bar{\mathbf{M}}_{ae}^{-1}\bar{\mathbf{\Theta}} & \bar{\mathbf{M}}_{ae}^{-1}\mathbf{A} \\ \mathbf{0} & \frac{-\bar{\mathbf{\Theta}}^{\mathrm{T}}}{R_l} & \frac{-1}{R_l \mathbf{C}_p} & \mathbf{0} \\ \mathbf{0} & \mathbf{I} & \mathbf{0} & \frac{V_\infty}{b}\lambda_{ae}\mathbf{I} \end{bmatrix} \begin{Bmatrix} \mathbf{X}_1 \\ \mathbf{X}_2 \\ \mathbf{v}_p \\ \mathbf{X}_S \end{Bmatrix} \tag{3.81}$$

where $\mathbf{X}_1$ is the modal amplitudes vector, $\mathbf{X}_2$ is the first time derivative of the modal amplitudes vector, $\mathbf{X}_S$ is the aerodynamic lag state vector, $\mathbf{I}$ is the identity matrix, b is the semi-chord of the wing, λ_{ae} is the lag aerodynamic root, the overbar represents modal matrices and the subscript *ae* represent the aeroelastic modified matrices.

For the present research, as mentioned before, the doublet method was implemented in MATLAB as well as the structural model. Once obtained the matrices in equation 3.81 for the linear electroelastic wing case, the stiffness and coupling terms are updated with the nonlinear matrices at each time step.

CHAPTER

4

Results

This chapter describes model validations and analyses for the different cases of this dissertation. First, manufacturing and experiments as well as model nonlinear finite element model validation are discussed for a double bimorph structure. Later, the nonlinear finite element model is validated for nonlinear MFC actuation and energy harvesting experimental results from the literature. In the end, nonlinear wind energy harvesting cases are discussed.

4.1 Nonlinear geometric verification

The nonlinear geometric model (without piezoelectric elements) was first verified against a static solution obtained from ABAQUS finite element analysis with large displacements assumption activated. A square plate (100 mm at each side and 1 mm thick) composed by Fatigue-Resistant 301 Stainless Steel was modeled. In the simulations, the plate was assumed clamped at one side and subjected to a normal force of 150 N in one of the free tip edges. Then the transversal displacement at this edge was calculated for increasing applied force until 150 N. Figure 8 displays the linear and nonlinear results. A good match is observed between the nonlinear model of this work and the solution obtained from ABAQUS.

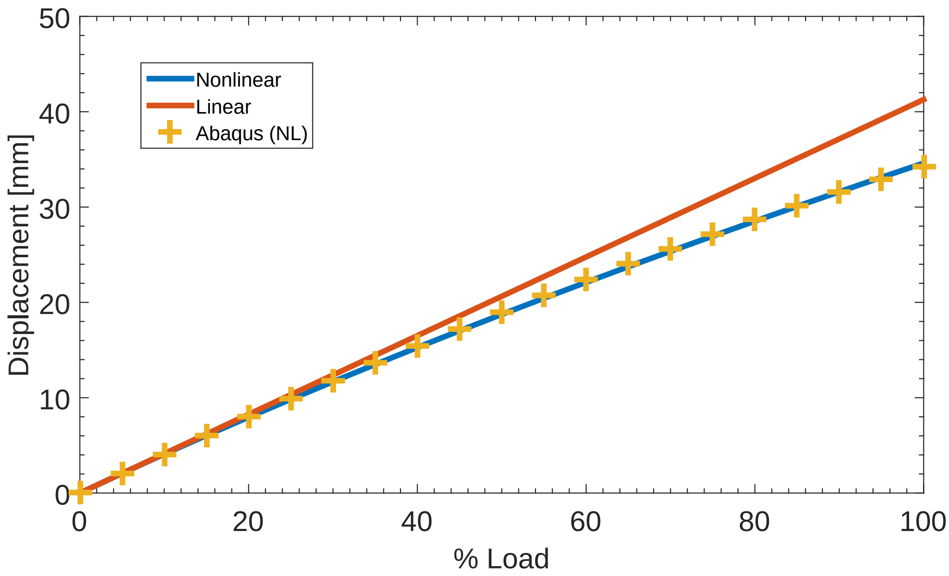

Figure 8 – Linear and nonlinear static maximum displacement for a clamped stainless steel square plate ($100x100x1mm$) under increasing force applied transversely at one free tip corner

4.2 Double bimorph Structure (manufacturing process)

This section describes the double bimorph structure composed by a flexible metallic substrate and the combination of two pairs of MFC actuators. The manufacturing process and experimental procedures are described in details as well as numerical model validation for actuation cases. This electromechanically coupled structure is also used in wind energy harvesting simulations - although two other model validations considering different MFC based structures presented in the literatures are discussed.

As displayed in Figure 9, four 0° MFC laminates (M8514-P1, Smart Material Corp. - see Table. 1) were bonded onto a flexible spring steel substrate (Fatigue-Resistant 301 Stainless Steel Sheets). With this configuration, two bimorphs are formed with a chord wise spacing of 33 mm to constitute a double bimorph system. The length of the steel plate is 84.4 mm, width of 73 mm and a thickness of 0.0508 mm. Each MFC have an overall size of 84.4 mm x 20 mm and an active region of 76.35 mm x 14 mm and a thickness of 0.30 mm and a clamped free capacitance of each MFC is 4 nF. A schematic of the double bimorph structure is shown in Figure 10 considering only the active region of the MFCs.

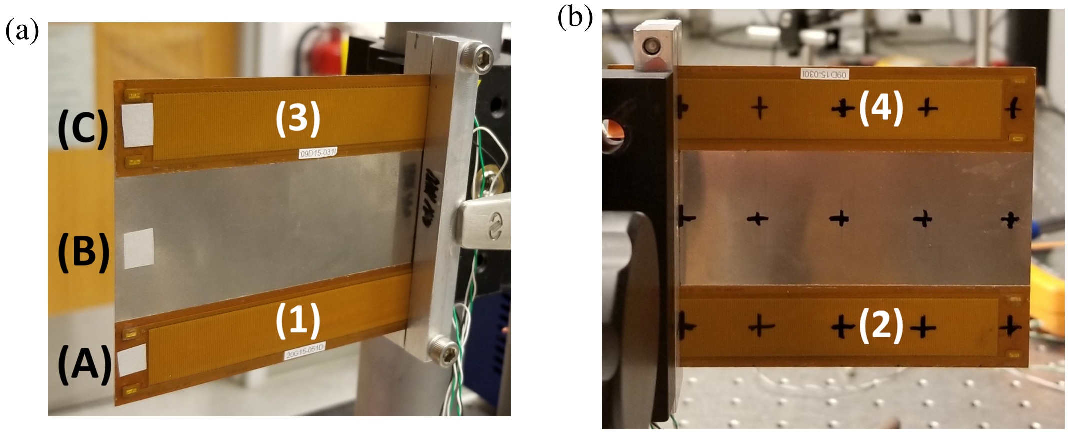

Figure 9 – Double-bimorph (84.4*x*73.0*x*0.0508 mm) architecture with MFC laminates and stainless-steel substrate: (a) top view along with the tip velocity measurement points and (b) bottom view along with displacement measurement points and labeling detail of the four laminates. The samples are clamped with an aluminum clamp at the wing root.

Table 1 – M8514-P1, Smart Material Corp. dimensions.

Property	Dimension [mm]		
Active Length	85		
Active Width	14		
Overall Length	101		
Overall Width	20		
Clamped Free Active Length	76.35		
Layer	Kapton	Copper	PZT
Thickness	0.040	0.018	0.180
Fiber Width	N/A	0.0977	0.3555
Fiber Spacing	N/A	0.3094	0.0344

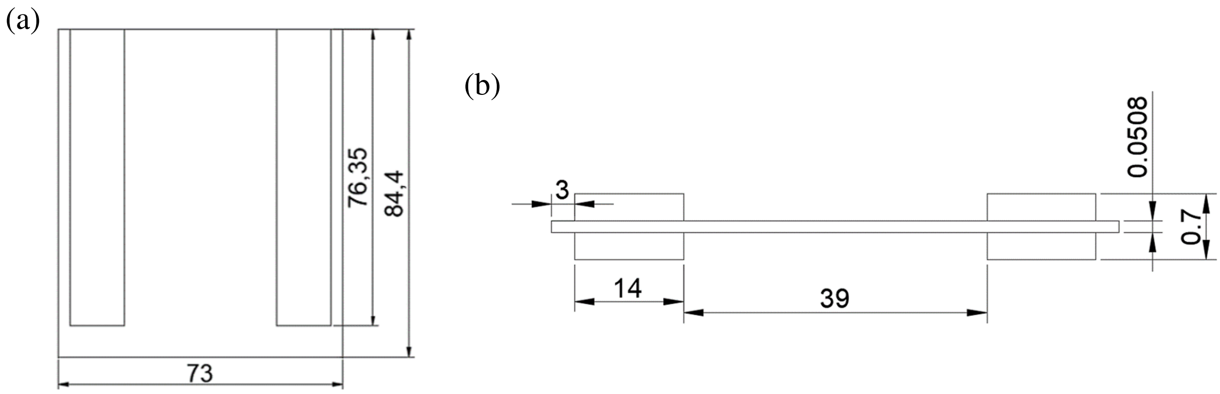

Figure 10 – Double-bimorph schematic with dimensions considering MFCs active areas and stainless-steel substrate: (a) top view and (b) front view (not to scale). Dimensions in mm.

Since the double bimorph will be later used in aeroelastic simulations, this structure is also considered an electromechanically coupled plate-like wing in this work. The leading edge bimorph is composed by the MFCs labeled as (1) and (2) while the trailing edge bimorph is composed by the MFCs labeled as (3) and (4). The points of transverse velocity measurement (labeled A, B and C in Figure 9) are placed on one of the sides of the plate (that will be referred as top side in this section). These points are selected to capture the bending and twisting motions and are placed at the mid-point of the tip of each MFC active region (10 mm from the leading and trailing edge) as well as at the center line of the wing. The distances from the tip of the plate to the points are 5 mm, 25 mm, 45 mm, 65 mm and 83 mm. The overall thickness on the active area in the final structure is 0.70 mm.

The geometric properties for the active (PZT fibers) and passive (epoxy, electrodes, and Kapton film) layers of MFCs are shown in Figure 11 for both xz-plane and yz-plane active area of the double bimorph structure. The element properties are evaluated based on the mixing rules (Appendix B).

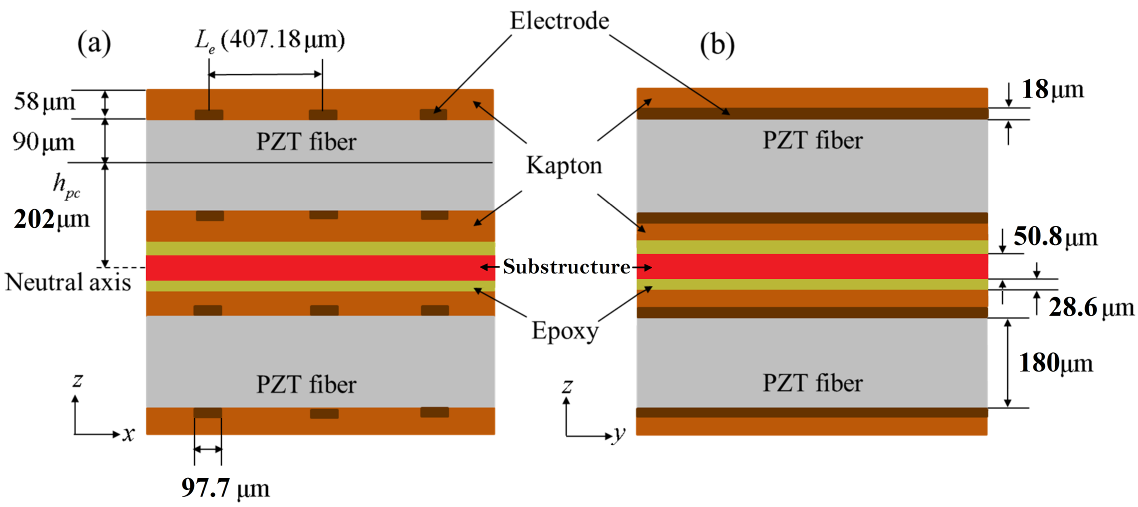

Figure 11 – Two-dimensional representation of the MFC bimorph area (made from two identical MFC laminates bonded using high-shear strength epoxy to the substructure with electrodes, epoxy and copper fibers, perpendicular to the PZT fibers embedded in Kapton film). (a) Geometric parameters in the xz-plane and (b) sequence of layers in the cross-sectional area (yz-plane: not to scale). Approximate data provided by manufacturer and (SHAHAB; ERTURK, 2017).

4.2.1 Experimental setups and procedures

As previously discussed, the double bimorph structure is used in this work for actuation tests and also numerical model validation. For the actuation tests, three Polytec PDV -100 portable digital vibrometers were used to measure the velocity at three measurement points simultaneously (reducing differences between results due different shapes). Data was acquired using a National Instruments NI USB-4431 board. The structure was mounted on the vertical direction to reduce the gravity effects in the results (figure 12a). One vibrometer was directly pointed at the wing while mirrors were used for the other two measurement points (figure 12b). Base acceleration experiments were conducted using an APS-113 seismic shaker driven by an APS-125 amplifier and controlled by a SPEKTRA VCS-201 controller. These devices allow the sample to be subjected to harmonic base acceleration at specified amplitudes and frequencies. Tests were conducted making an up and down frequency sweeps at a constant base acceleration amplitude.

(a) (b)

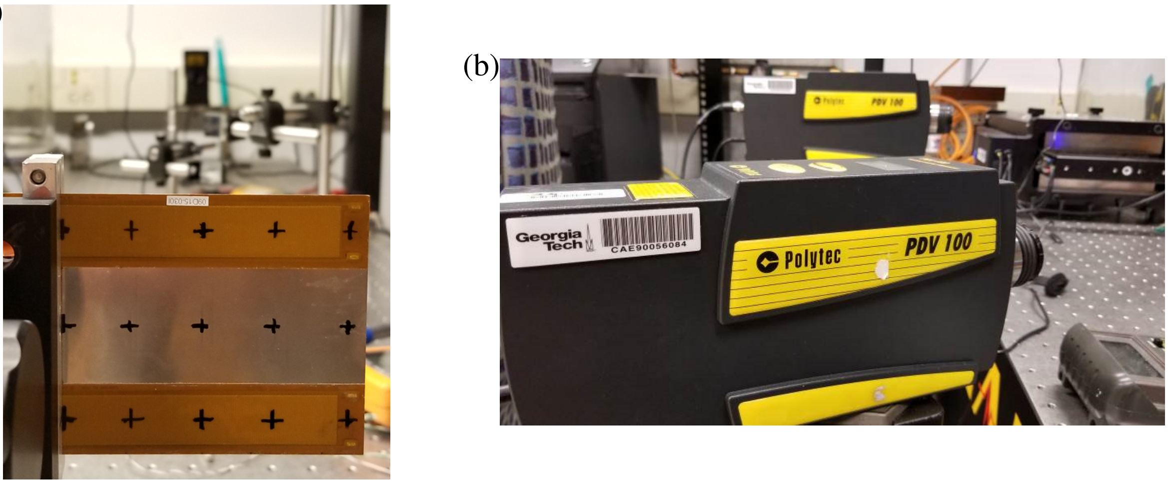

Figure 12 – Overview of experimental setup (a) double bimorph wing (84.4x73.0x0.0508mm) mounted with Vibrometer and mirror at the background and (b) two other vibrometers pointing at the structure through mirrors

4.2.2 Preliminary results

In the first attempt to manufacture the double bimorph system, a hardened easy-to-form highly corrosion-resistant 1100 aluminum sheets with a thickness of 0.0762 mm from McMaster was employed as substructure. The material was available at the laboratory and seemed to be sturdy enough visually and in the computational model.

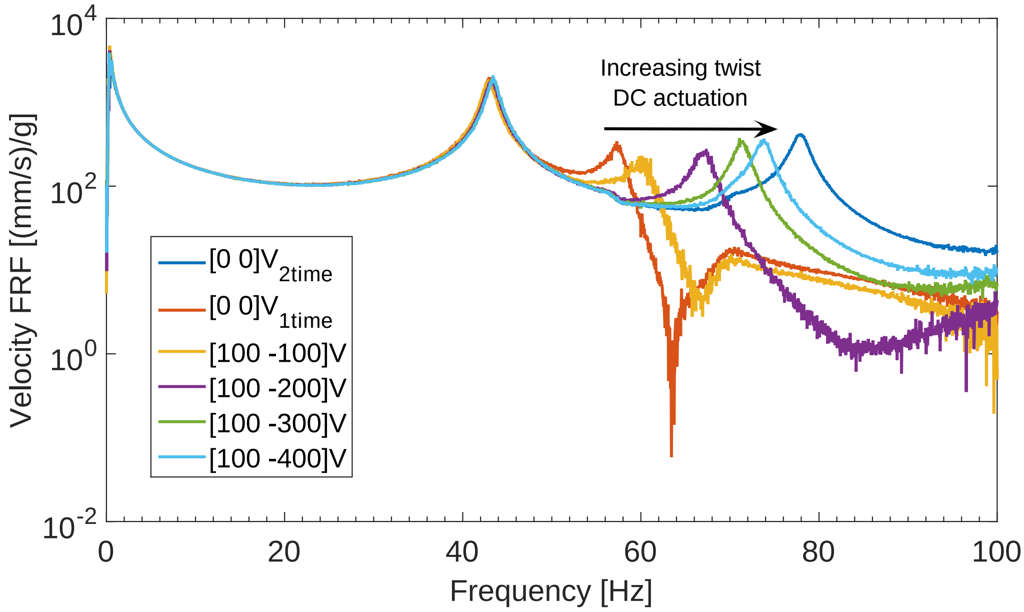

Figure 13 – Peak-to-peak velocity per base acceleration FRF of the double bimorph (considering the aluminum substrate - 84.4x73.0x0.0762mm) measured at point (A) for different levels of static actuation on the MFCs and base excitation of the wing

During the first bench top tests, the plate was clamped to the shaker and submitted to base excitation. In these first experiments the velocity response was measured at point (A) of Figure 12(a). Piezoelectric actuation tests (DC actuation) were also performed simultaneously to the base excitation tests. As a consequence, it is observed that the experimentally identified frequencies of the resonances changed from the original base excitation test (before piezoelectric actuation) to the base excitation tests after actuation tests. Therefore, to investigate such behavior, base excitation and simultaneous DC actuation tests were performed and the results are displayed in Figure 13. Initially, frequency response was measured without piezoelectric actuation ($[0\ 0]V_{1time}$ curve in Figure 13). Later, DC voltage was applied to the MFCs, 100 V was always applied to one MFC bimorph (in all tests) while -100, -200, -300 and -400 Volts applied to the other MFC bimorph in each test. After these experiments, the voltage input was set again to zero, and the frequency response function (FRF) measured in the absense of piezoelectric actuation (dark blue color on Figure 13 - $[0\ 0]V_{2time}$). It is interesting to note that while the bending frequency changes from 42.9 Hz to 43.5 Hz the twist frequency vary between 57.3 Hz to 77.9 Hz. The numerical models (linear electric with or without geometric nonlinearity) could not predict the behavior experimentally observed in Fig. 13. Therefore, we decided to perform some additional model verification and also try a deeper investigation of the experimetal behavior that will discussed in section 4.2.3.

The linear and nonlinear numerical models predicted reasonably well (less than two percent difference) the bending resonance frequency, but was underestimating the twist resonance frequency, as observed in Fig 13. Therefore, we started a finite element model verification against results obtained from a commercial FE program. The finite element program, developed during the current research, was analyzed to search for any type of error and was compared successfully with a model made in COMSOL Multiphysics (in both programs were assumed a plate of 301 stainless steel with the same dimensions of the double bimorph previously described, the comparison is shown in table 2). The first bending and torsion modes acquired with MATLAB program are close to the ones obtained in COMSOL, for the second modes, the frequency comparison start to separate. It is important to notice that in COMSOL the plate was modeled with solid elements while in MATLAB the program was developed based on Kirchhoff plate as mentioned before.

Table 2 – Resonance frequency comparison between COMSOL and MATLAB model of a 301 stainless steel plate (with dimensions: $84.4x73.0x0.0508mm$).

Mode	COMSOL	MATLAB
1st Bending	5,2461	5,808
1st Torsion	16,286	15,8019
2nd Bending	38,631	35,9692
2nd Torsion	62,649	55,8321

A more complex approach to describe the MFC layer by layer was also considered. Despite better results, the twist frequency did not match the experimental behavior. After studying the nonlinearities of the MFCs and the nonlinear geometric program developed, it was decided to make the frequency analysis with a deformed shape since creeping effects in the bimorphs could lad to changes on the initial stiffness matrix. With this approach the results were closer to the ones observed in the experiments as will be presented next. Just remembering that the model considers the MFCs only at the active area, neglect the side electrodes on the MFCs and consider an equivalent material, obtained by mixing rules (DERAEMAEKER et al., 2009).

4.2.3 Pre-deformed analysis

To prevent any type of nonlinearity like plastic deformations on the substrate (since the last substrate presented some small shrinks after bounding), a new plate with spring steel substrate was considered. The dimensions are the same previously described. The new double bimorph was clamped and placed on the vertical (as shown in the figure 9, figure 12). The actuation was performed only by applying sinusoidal voltage inputs in each MFC separately. To actuate the system and not induce any sort of change in the stiffness of the bimorph spars, the voltage levels are the same with opposite signal between MFCs 1 and 2 and between the MFCs 3 and 4. If the two bimorphs are actuated symmetrically, only bending is introduced, if they are actuated with opposite signals, only twist is introduced to the structure. Otherwise, any other combination will result in a combination between bend and twist. In the analysis proposed in this section, the voltage level applied is set to 1 V to reduce the softening of piezoelectric materials.

Taking a deeper look in the experiment, model and in the analysis proposed, it was noticed that any sort of initial deformation changes the behavior of the double bimorph. First, the overall structure, as well as the substrate thickness are thin compared with other dimensions. Secondly, when considering the nonlinear geometric elastic model simulation, the stiffness depends on the initial deformation. In this way, it was decided to apply a small deformation in the simulations (applying a small voltage in the bimorphs generating a small twist), obtaining the initial stiffness matrix accordingly with the nonlinear method proposed, and consider this initial stiffness matrix as the base for the modal analysis.

With an initial pure twist deformation with maximum transverse displacement of 0.08 mm (distance of the wing in relation to the reference plane) the model predicted a resonance frequency closer to the one obtained in the experiments. At this point is important to mention that due to the creeping (as discussed later), the deformations change between different experiments and they make a huge influence in the behavior. The overall thickness on the active area of the bimorphs is 0.7 mm, thicker than the initial deformation that the plate was subjected. The deformation displacement is barely noticeable and can be generated by a mix between bend and twist of the wing making this hard to predict the position in each single experiment, once it depends on the creeping history since the initial manufacturing. Taking this in consideration, the following experimental results are compared with numerical results with different initial deformations.

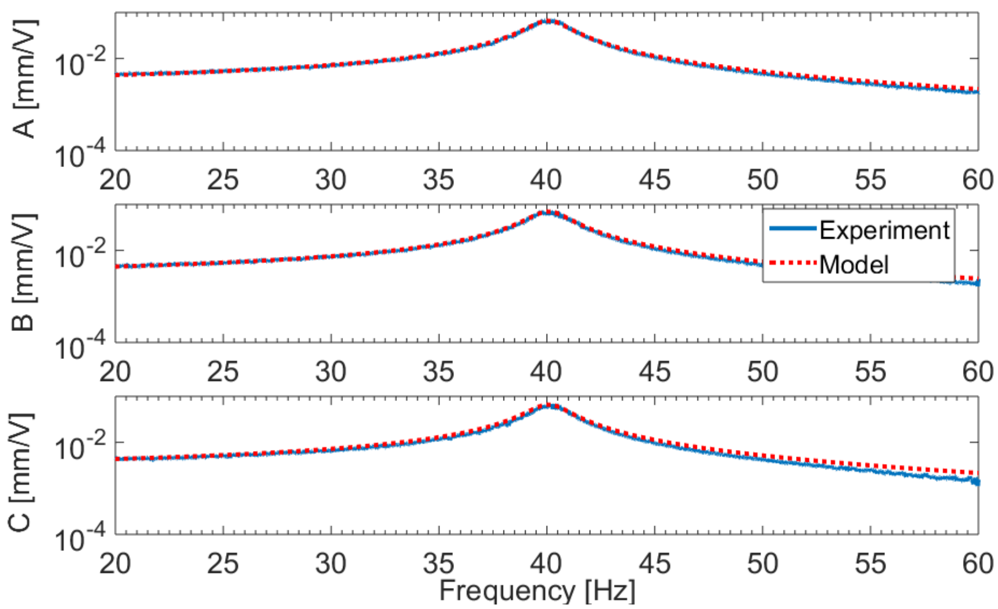

Figure 14 – Peak-to-peak displacement per Volt FRF of the double bimorph (considering the stainless steel substrate - 84.4x73.0x0.0508mm) measured at points A, B and C due pure bending actuation on the MFCs

First it is considered the actuation in pure bending for the double bimorph wing with stainless steel substrate, the results are shown in figure 14 for the left (point A), center (point B) and right (point C) measuring points. The experimental results are shown in the blue continuous line and the numerical model results shown in the dashed red line. DC voltage is applied on the simulations in order to obtain a twist with maximum displacement of 0.069 mm on the model. One important fact is that the nonlinearity due to the piezoelectric actuation was neglected at this point and will be studied in the next section. The modal analysis considers only the first five modes of vibration of the wing and this reduction will be used on the next analysis. As mentioned before, the hysteresis behavior of the piezoelectric materials are not considered and the model is reduced to a linear actuation.

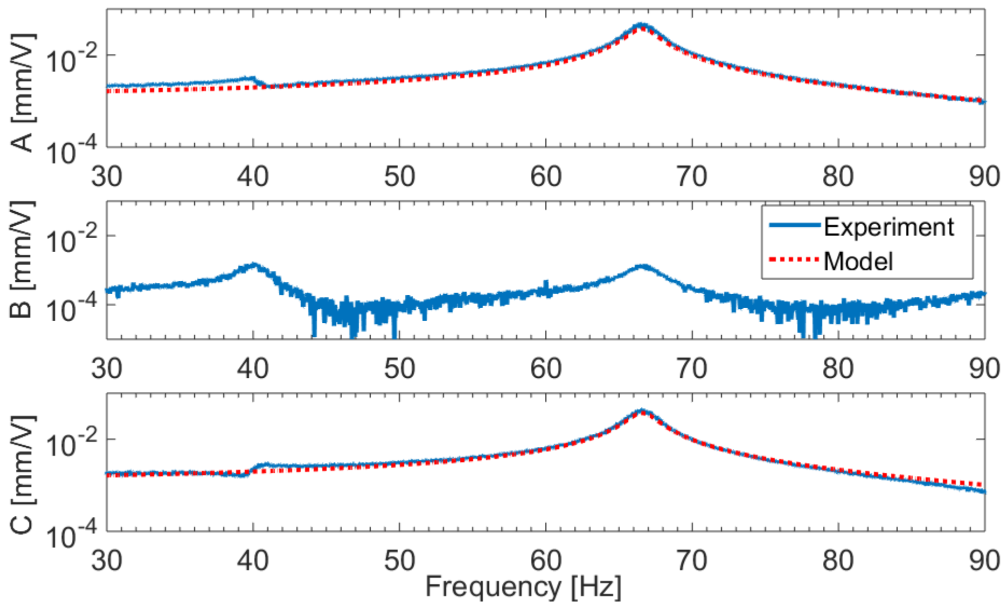

Figure 15 – Peak-to-peak displacement per Volt FRF of the double bimorph (considering the stainless steel substrate - 84.4x73.0x0.0508mm) measured at points A, B and C due pure twist actuation on the MFCs

Another important point is in the pure twist actuation, to reproduce the experimental behavior an actuation with 180° of phase between the bimorphs were applied to the MFCs. The results are shown in Figure 15 for the left (point A), center (point B) and right (point C) measuring points. The experimental results are shown in blue continuous line and the numerical model results shown in dashed red line. It was applied an initial twist with maximum displacement of 0.088 mm on the model to consider the creeping effect present in the experiments. In the experimental results it is noticeable a small peak around 40 Hz for the frequency response at points A and C. Further analysis had shown that one of the MFCs, that compose the leading edge bimorph, had a higher capacitance than the other three after the bounding at the substrate. This non-symmetric property generates some bending while considering only twist actuation, as well as the opposite. It is interesting to notice that for the second plot of figure 15 the model predicts an amplitude around 10^{-13} while the experiments show an amplitude around 10^{-3}, this can be explained by the resolution of the lasers pointed to the 3 measurement points as well as the non-symmetric capacitance mentioned.

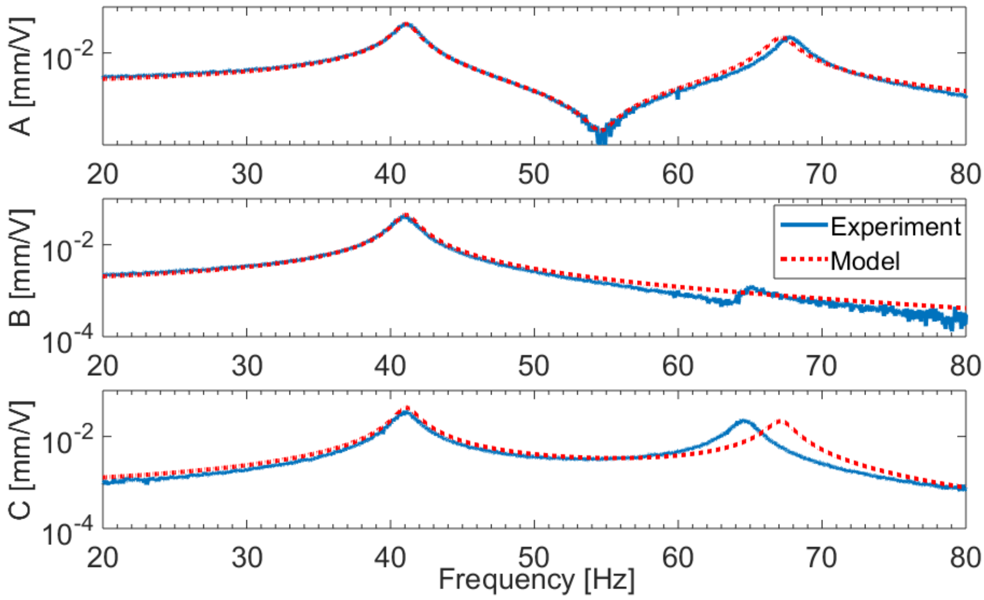

Figure 16 – Peak-to-peak displacement per Volt FRF of the double bimorph (considering the stainless steel substrate - $84.4x73.0x0.0508mm$) measured at points A, B and C due actuation on the MFCs 1 and 2 (leading edge bimorph)

To show the bending and twist behavior in the same analysis, an excitation of one of the two bimorphs were made independently (without actuation of the other bimorph). The results are shown in figure 16 and figure 17 for the measuring points (A, B and C) for the actuation on the leading (left bimorph) and trailing edge bimorphs (right bimorph) respectively with one-volt excitation. The experimental results are shown in the blue continuous line and the numerical model results shown in the dashed red line. It was applied an initial twist with maximum displacement of 0.090 mm on the model to consider the creeping effect present in the experiments. A small peak on the B measurement point close to the twist resonance frequency can be noticed. This peak appears on a frequency smaller than the twist resonance frequency. It is important to remember that the previous deformation on each MFC due creeping can be different from each other. This non-symmetry is shown clearly on the measurements on the B point shown in figure 16 and figure 17. For a perfect symmetric structure the responses should be exactly the

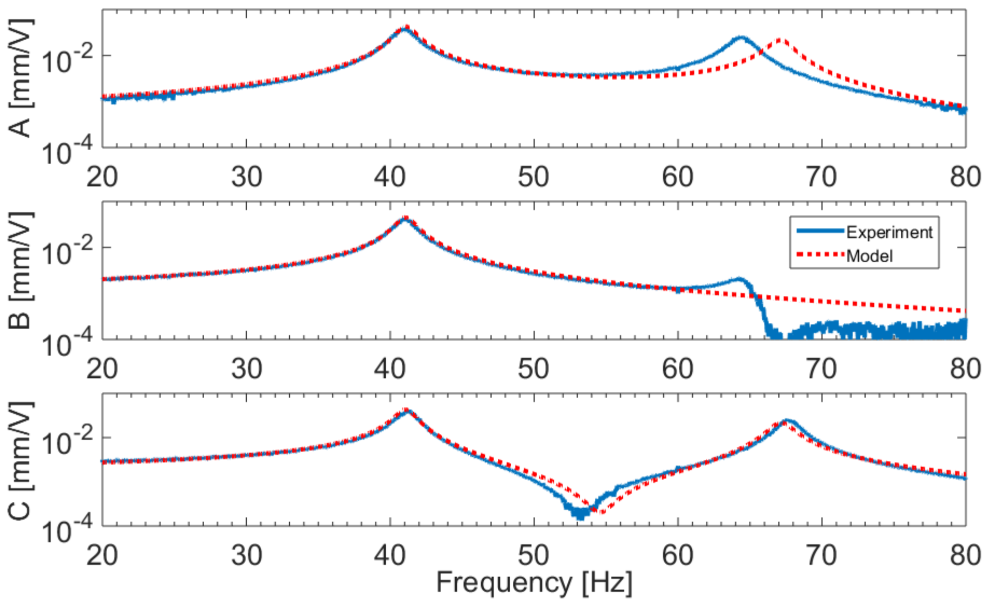

Figure 17 – Peak-to-peak displacement per Volt FRF of the double bimorph (considering the stainless steel substrate - 84.4*x*73.0*x*0.0508*mm*) measured at points A, B and C due actuation on the MFCs 3 and 4 (trailing edge bimorph)

same, however as shown in the experimental response, near the twist resonance frequency, the behavior in both cases are different in relation with each other and with the linear behavior.

Despite some changes in the behavior due to previous deformation caused from creeping and some simplifications, the nonlinear geometric model can predict the behavior of the double bimorph during actuation. The cases investigated so far consider linear piezoelectricity, nonlinear cases will be investigated later.

4.2.4 Nonlinear displacement analysis (creeping)

Displacement tests were also performed with the double bimorph structure in order to check the creeping behavior. Some deflections were measured at the points A, B and C defined in figure 9. As mentioned before, creeping occurs in piezoelectric materials and has significant effects on the behavior of the electromechanically coupled structure.

As discussed in the previous section, an initial deformation changes the behavior of the wing by changing resonance frequencies of bending and torsion modes, although it is more

(a)

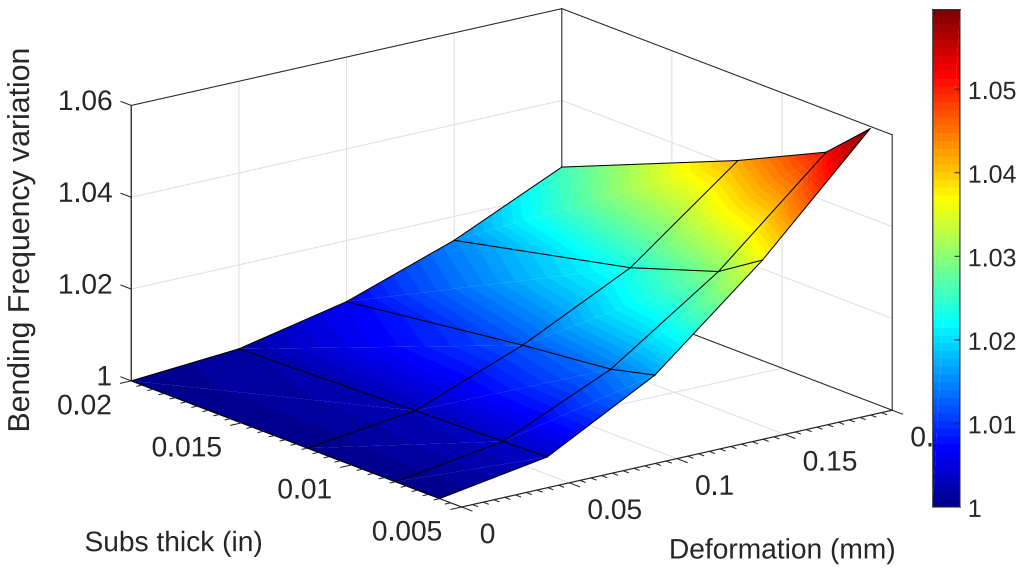

(b)

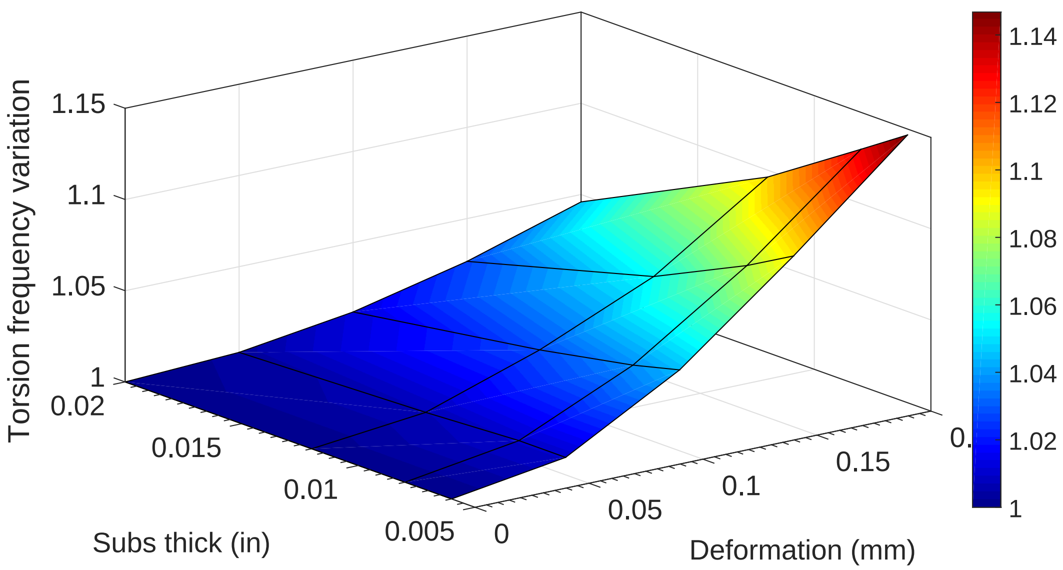

Figure 18 – (a) Bending and (b) Torsion resonance frequency response for the stainless steel wing plate ($84.4x73.0x0.0508mm$) double bimorph for different thickness and twist deformations compared with the wing without any previous deformation.

evident for the torsion modes. Simulations were performed in order to check this behavior as well as the effects of substructure thickness and deformation level on the resonance frequencies and the results are shown in figure 18. The frequency variation shows the ratio of the natural frequency modified by the initial displacement and the frequency of the system without displacements. For the bending mode, the main source of the stiffness is the MFCs, since they are significantly thicker than the substrate. On the other hand, thickness of the substrate has great effects on torsion mode, although the stiffness of the MFCs is also relevant. If the thickness of the substrate is reduced, the resonance of the torsion mode decreases and tends to the resonance of bending mode. Since the displacements are out of the plane, deformations increase the amount of substrate material between the bimorphs. In this way, the creeping is important for the frequency response of the wing.

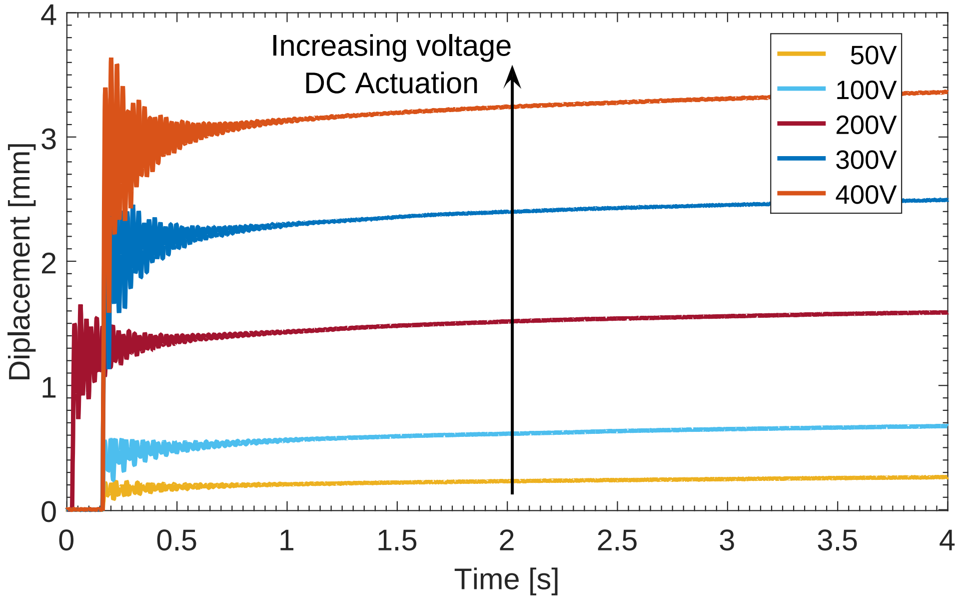

Figure 19 – Time response of the double bimorph (considering the stainless steel substrate - $84.4x73.0x0.0508mm$) measured at point A due bending actuation on both bimorphs.

Creeping time histories are shown in figure 19 (step responses at the point A of the wing for different levels of actuation) for further analyses in the next steps of the research. As mentioned before, the final deformation is not obtained directly, the increasing deformation due to the actuation of the MFCs (creeping) extends sometimes for more than one minute. Moreover, after the actuation of the MFCs is released, a residual deformation is always observed.

Another important creep analysis is relate to the voltage level and number of cycles of actuation. For instance, figure 20 shows the permanent deformation of the structure after 20 cycles of actuation for different voltage levels applied during 45 seconds, and then released. The result can be approximate linearly alongside the actuation levels. It is important to notice that even for 400 V of actuation a permanent deformation around 1.5 mm (remember that the twist pre-deformations considered during the frequency response was at the most 0.09 mm) is observed.

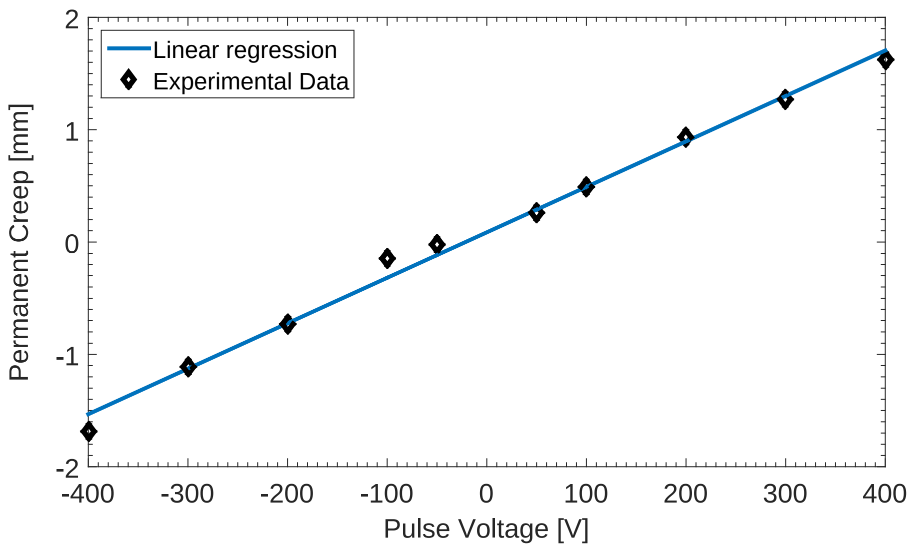

Figure 20 – Permanent deformation after 20 pulse oscillations of 45 seconds (considering the stainless steel substrate - $84.4x73.0x0.0508mm$) measured at point A due to the bending actuation on both bimorphs.

The effects of the number of cycle of is shown in figure 21. The permanent deformation increases with the number of pulses and this behavior is more evident for high voltage actuations, although even for one oscillation a permanent deformation is observed.

For the creeping analyses it is important to investigate the history of actuations on the structure, since each one has effects on the future behavior of the structure. Models that completely describe all the nonlinearities involved in the creeping behavior have not been found in the literature and are also out of the scope of the present work. In the previous cases (structural response), an initial deformation was imposed to the model through a small actuation using the MFCs.

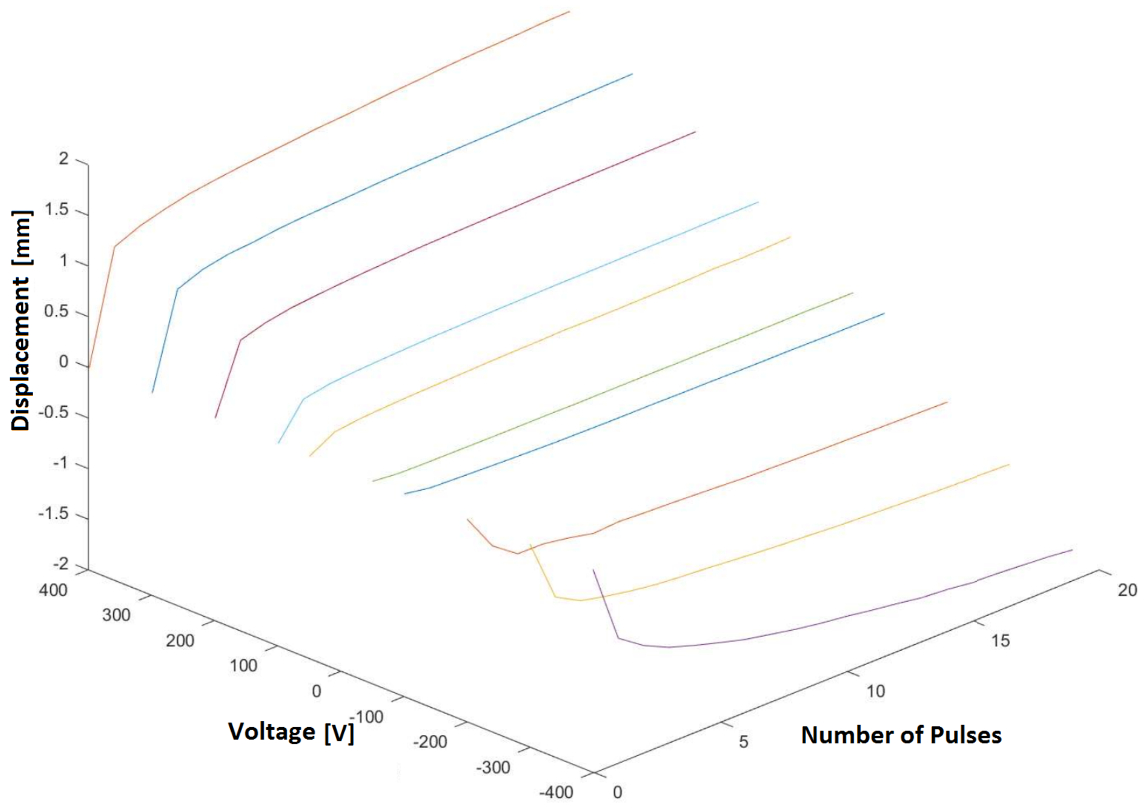

Figure 21 – Permanent deformation after 45 seconds pulse oscillations (considering the stainless steel substrate - $84.4x73.0x0.0508mm$) measured at point A for bending actuation on both bimorphs with different actuation levels.

4.3 Nonlinear electroelastic model validation

In this section, the nonlinear numerical model presented in this work (nonlinear finite element model combined to nonlinear piezoelectric model) is validated for two different cases. The coupled ordinary differential equations (ODEs) given by equations 3.31 and 3.32 considering the nonlinear stiffness matrix given by equation 3.74 and nonlinear coupling presented in equation 3.75 are solved using the method of harmonic balance (NAYFEH; MOOK, 2008) for all acceleration and voltage actuation levels considered in the experiments. Since the excitation is assumed to be harmonic, the mechanical response solution is expected to have the same period as the electrical excitation and can be approximated by truncated Fourier series expansions. Seven harmonics are considered to predict the electroelastic response in both cases. First, numerically predicted behavior of the double bimorph structure under piezoelectric actuation is verified against experimental results. Later, the model predictions are verified against experimental results presented in the literature for a MFC bimorph cantilever under base excitation in a vibration based energy harvesting problem.

4.3.1 Nonlinear MFC actuation tests

As mentioned in the literature review, nonlinear piezoelectric behavior has been noticed even at low actuation levels. Therefore, during the experiments to be discussed in this section, actuation levels from 0.5 V to 50 V were considered for both pure bending and pure twisting cases of the double bimorph structure discussed in the previous section.

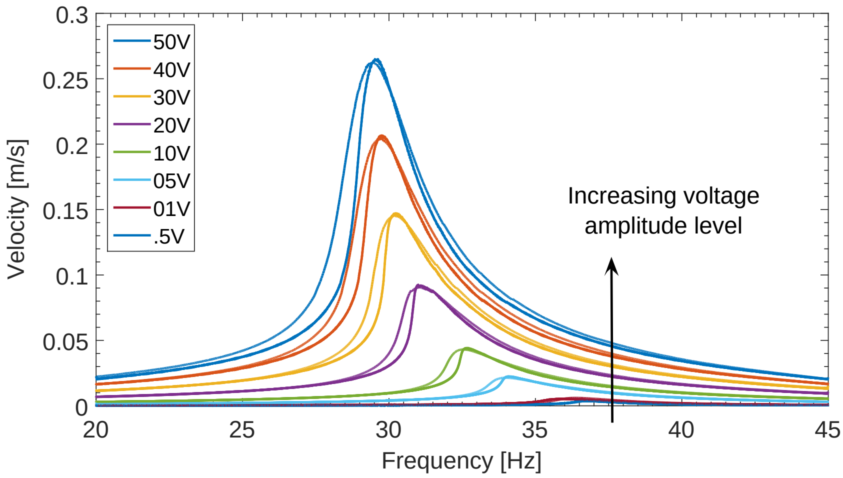

Figure 22 – Velocity frequency response of the double bimorph (considering the stainless steel substrate - $84.4x73.0x0.0508mm$) measured at point A due to the bending actuation on both bimorphs. Frequency sweep up response represented by continuous line and frequency sweep down by dashed lines.

For the actuation in pure bending, the measurement along the chord (points A, B and C) resulted in similar responses. Therefore, the frequency responses will be displayed only for the leading edge measurement point (point A). Figure 22 displays the tip velocity response for harmonic piezoelectric excitation. In this figure, continuous lines stand for frequency sweep up while dashed lines are for sweep down. In both cases, softening behavior is observed with increasing applied voltage. It is important to note that the linear behavior of the previous section was obtained (numerically and experimentally) for excitation level of 1V. One should also note in figure 22 that the backbone curve (which connects the peaks of frequency response curves at all excitation amplitudes) is different from the ones previously reported in the literature (mostly due to complex behavior of the MFCs) justifying the new nonlinear model for the piezoelectric material discussed in section 2.1.3 of this work.

Figure 23 displays the ratio of measured tip velocity (as in figure 22) to the voltage input. In such case, the softening behavior is clearly observed for all excitation levels. As in the previous case, continuous lines are for the sweep up cases and dashed lines represent for sweeping down. The resonance frequency changes from 37 Hz to 29.7 Hz with increasing actuation voltage, what is related to the softening behavior of the piezoelectric material.

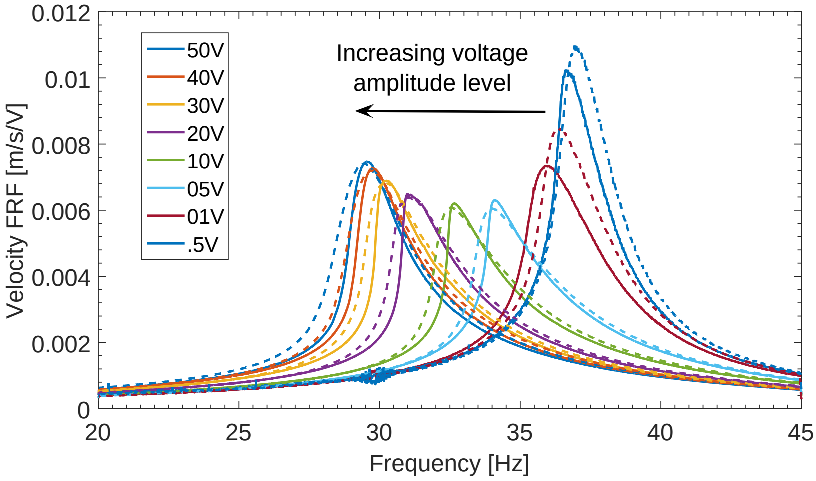

Figure 23 – Velocity per actuation voltage of the double bimorph (considering the stainless steel substrate - $84.4x73.0x0.0508mm$) measured at point A due to the bending actuation on both bimorphs. Frequency sweep up response with continuous line and frequency sweep down on dashed lines.

The frequency behavior of the ratio of electrical current to voltage input is displayed in figure 24. Once again, the continuous lines represent the response with increasing frequency actuation and the dashed lines represent the response with decreasing frequency actuation. Expectedly, the softening behavior is also observed in the respose.

In a recent paper, Tan, Yavarow and Erturk (2018) presented the nonlinear modeling of electromechanically coupled systems with MFCs. In their work, piezoelectric nonlinearity is considered proportional to the modulus of the strain and a quadratic hardening nonlinearity

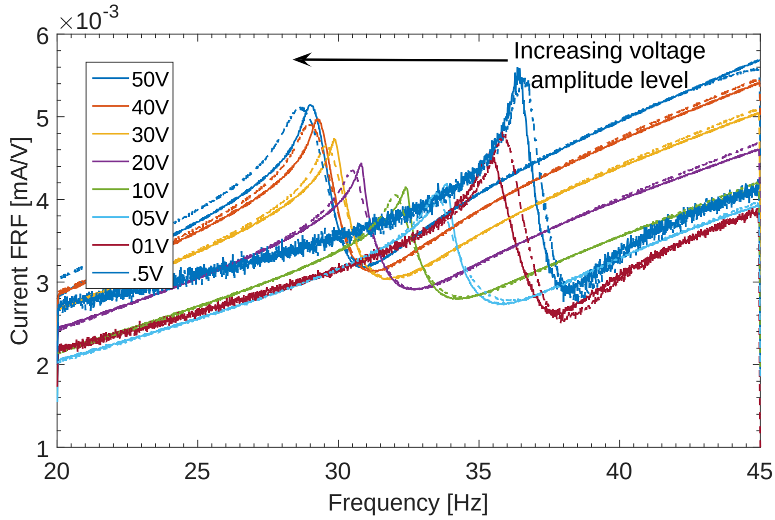

Figure 24 – Electrical current per actuation voltage FRF of the double bimorph (considering the stainless steel substrate - $84.4x73.0x0.0508mm$) measured at point A due to the bending actuation on both bimorphs. Frequency sweep up response with continuous line and frequency sweep down on dashed lines.

assigned to geometric hardening. When the same model is considered in the present analysis (combining their enthalpy for nonlinear MFC behavior with the nonlinear FE model of our work) the model can predict the behavior only for lower voltage levels. However, the model predictions overestimate the softening behavior at higher voltage input levels.

The first approach in this work was to model the nonlinear behavior of the MFCs behavior using a power function (in the form of $\alpha|S|^{\beta}$). In such case, the same backbone curve of Figure 22 is obtained for low and medium strain values although the nonlinear geometric hardening was not enough to predict higher actuation levels behavior. At this point was proposed the exponential enthalpy model presented in section 3.1. The comparison between numerical and experimental results for the proposed model are shown in figure 25.

The backbone is properly predicted for all voltages considered as well as the velocity amplitudes are correctly predicted. Since the creeping does not affect significantly the bending frequency, an estimation of the parameters could be performed. The terms that compose the nonlinear stiffness matrix ($\int_{V_p} z^2 \mathbf{B}_K{}^{\mathrm{T}} \mathbf{C}_p^{\mathrm{E}} \left(\mathbf{I} + \alpha \left\{ \mathbf{I} - \mathrm{diag}\left[\exp\left(|\mathbf{S}|^{\beta}\tau\right)\right]\right\}\right) \mathbf{B}_K \mathrm{d}V_p$) were obtained as $\alpha = 0.437$, $\beta = 0.75$ and $\tau = -7.71$.

In the same way that the pure bending case was investigated, the pure twisting actuation

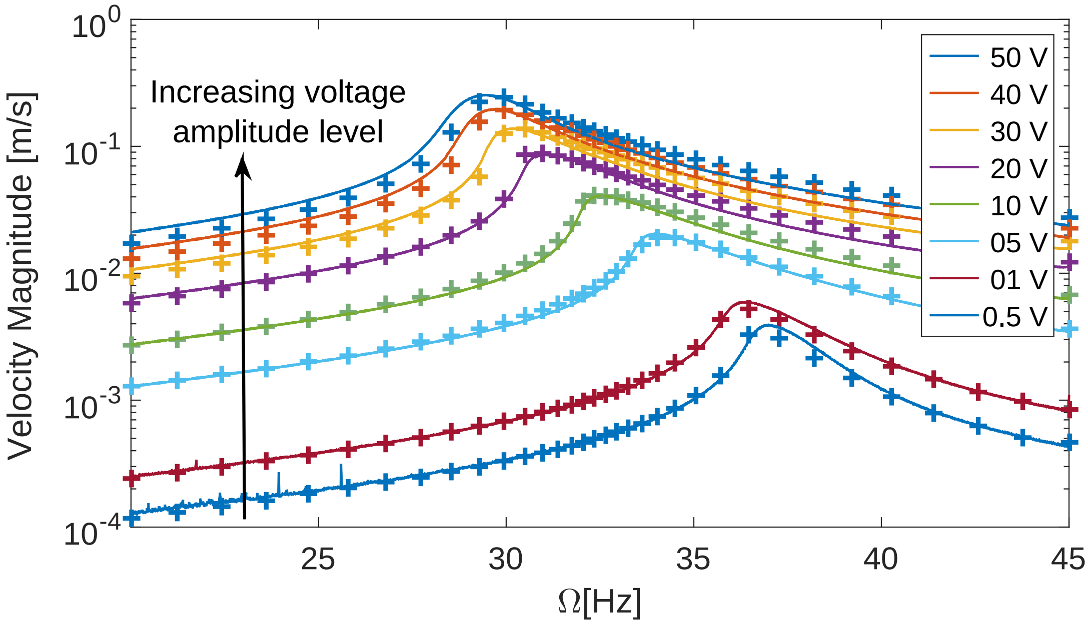

Figure 25 – Velocity frequency response of the double bimorph (considering the stainless steel substrate - $84.4x73.0x0.0508mm$) measured at point A due to the bending actuation on both bimorphs. Experimental results with continuous line and numerical results are presented with a $'+'$ marker.

is discussed next. However as mentioned before, the resonance frequency is more affected by deformation due to the creeping of the structure than in the bending case. The experiments were conducted making all the up sweep tests with increasing actuation voltage followed by the down sweep experiments. The results for up sweep and down sweep will be displayed separately, once some of the creeping residual deformations influence the frequency response of the structure.

The analysis of the velocity response (by applying a signal with 180° of phase between bimorphs) is displayed in figure 26 and figure 27 for the up sweep and the down sweep, respectively. Despite some differences in the frequency and amplitude in both cases it is possible to observe an initial softening behavior of the structure that is replaced by a hardening behavior for voltages larger than $10V$. The softening observed in figure 26 and figure 27 is due to the MFCs nonlinear behavior while the hardening is related to the nonlinear geometric behavior of the plate. The nonlinear geometric behavior is more pronounced for the twist where the internal stresses of the plate generate a higher rise in the stiffness than in the bending case. Moreover, the jump behavior observed in the results are related to the geometric nonlinearity.

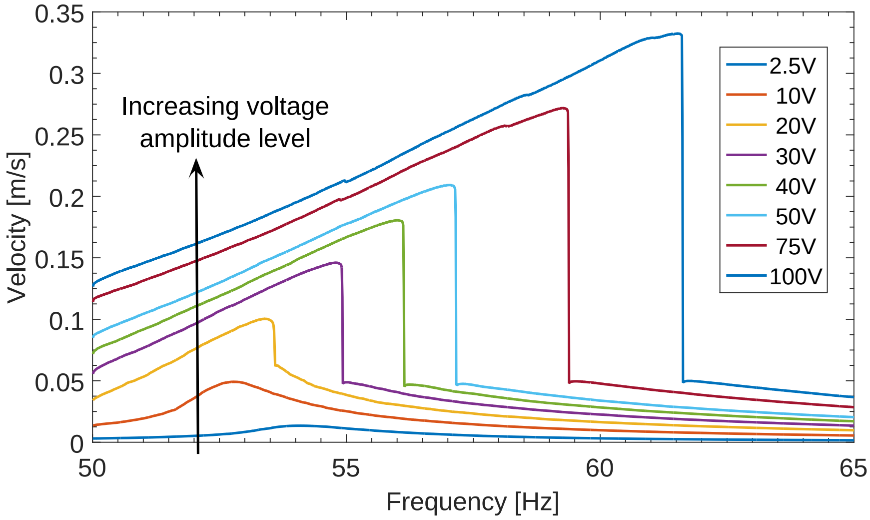

Figure 26 – Experimental up sweep velocity frequency response of the double bimorph (considering the stainless steel substrate - 84.4x73.0x0.0508mm) measured at point A due to the twisting actuation between bimorphs.

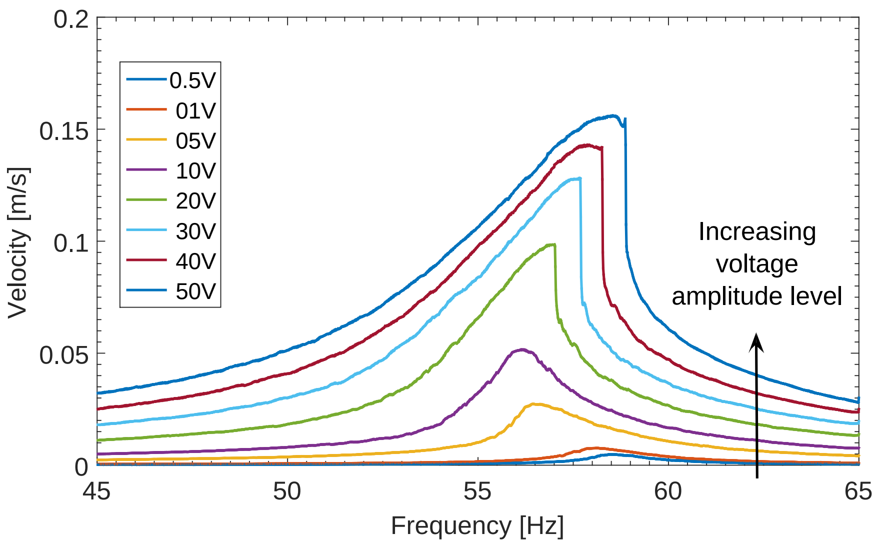

Figure 27 – Experimental down sweep velocity frequency response of the double bimorph (considering the stainless steel substrate - 84.4x73.0x0.0508mm) measured at point A due to the twisting actuation between bimorphs.

Again, it is important to show the velocity per actuation voltage frequency response. The response for frequency up sweep and down sweep of the leading edge (point A) for different voltage level inputs is shown in figure 28. In the twist actuation case, the softening behavior is present even for low voltage actuation levels of the MFCs bimorphs. It is important to notice the difference between both up and down sweep cases, there is a clear variation of the stiffness besides from geometric hardening or piezoelectric softening. Therefore, is experimentally observed that the creeping changes the behavior of the structure (and as commented before this behavior is less perceptible for the pure bending case). The electrical current response is displayed in figure 29, where figure 29a represents the response with up-sweep excitation and figure 29b represents the down-sweep excitation response.

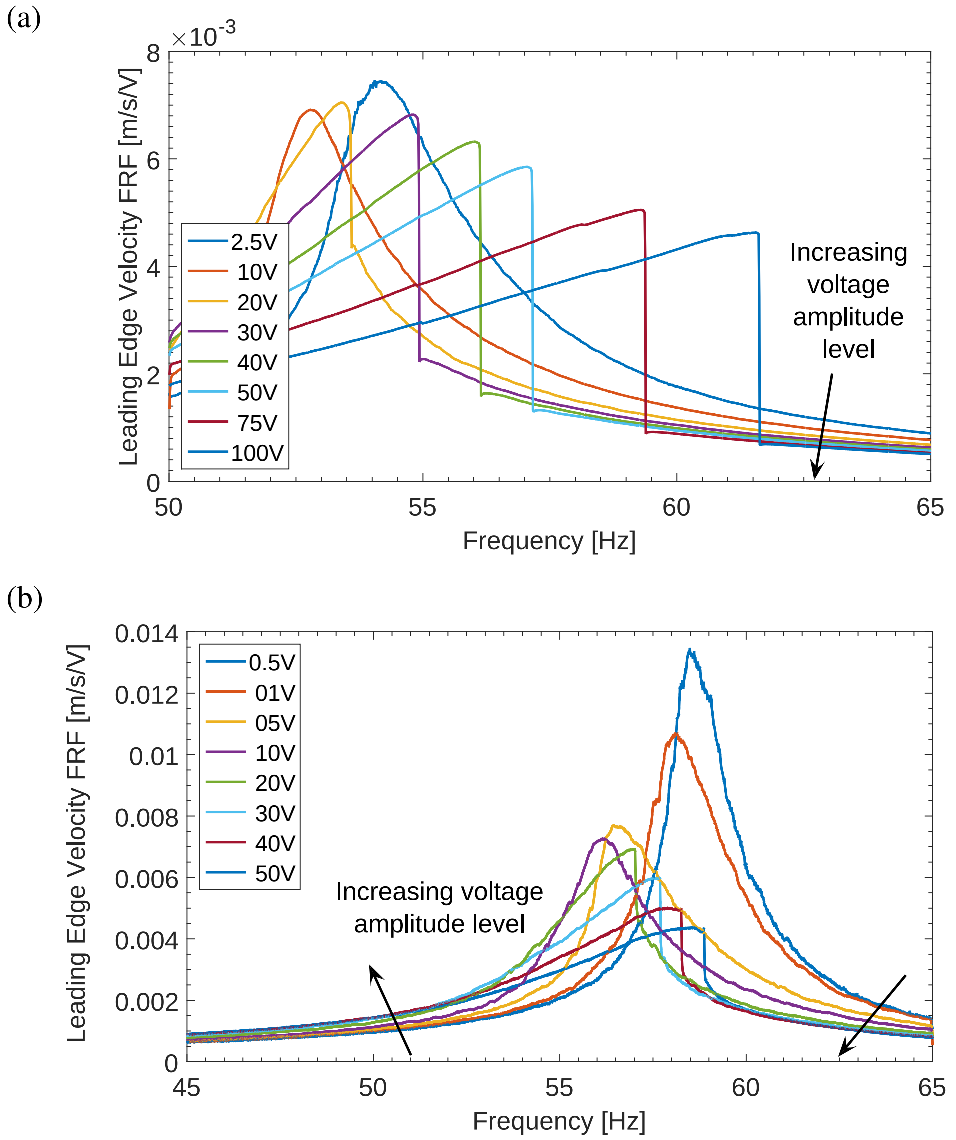

Figure 28 – Velocity per actuation voltage of the double bimorph (considering the stainless steel substrate - $84.4x73.0x0.0508mm$) measured at point A due to the twisting actuation between bimorphs generate for analysis with (a) frequency sweep up response and (b) frequency sweep down results.

(a)

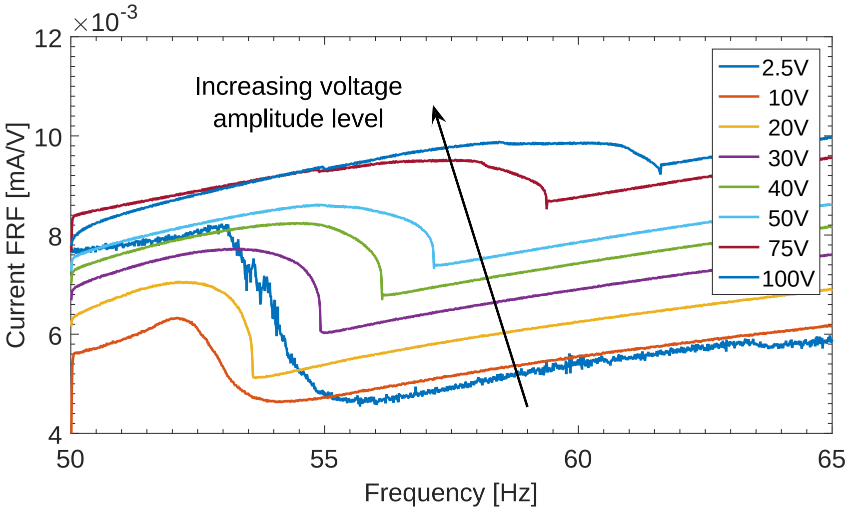

(b)

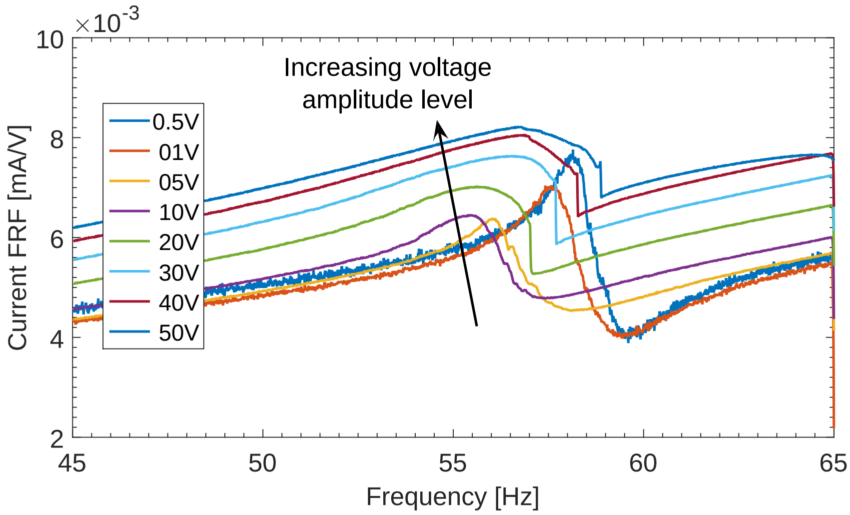

Figure 29 – Electrical current per actuation voltage of the double bimorph (considering the stainless steel substrate - 84.4*x*73.0*x*0.0508*mm*) measured at point A due to the twisting actuation between bimorphs generate for analysis with (a) frequency sweep up response and (b) frequency sweep down results.

The experimental backbone has an initial softening and then, for higher voltage levels, a hardening. Such behavior is also obtained in the numerical approach, as displayed in Figure 30. Also, one should note in Figure 30 that the first resonance frequency in torsion is lower than the one obtained experimentally. Several factors contribute to this behavior especially the creeping as commented before. It's important to mention that creeping has not been considered in the numerical model.

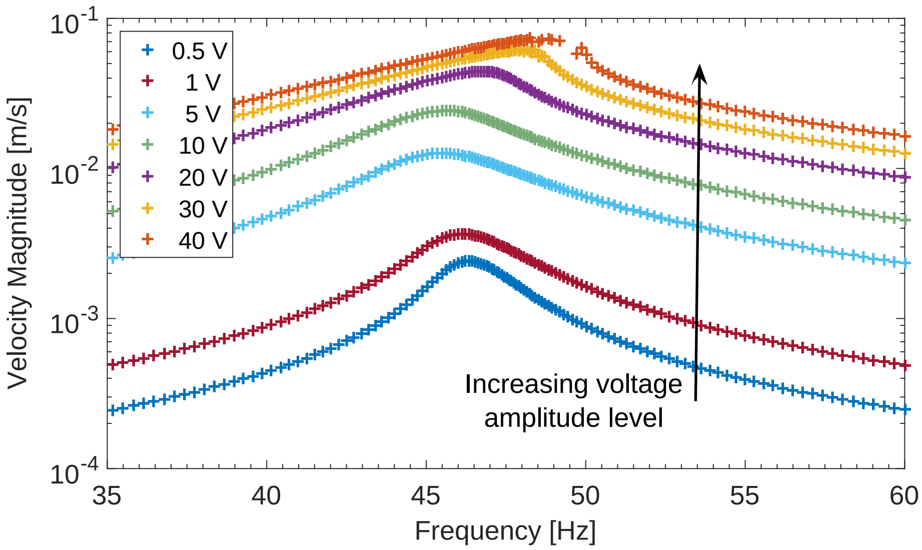

Figure 30 – Numerical velocity frequency response of the double bimorph (considering the stainless steel substrate - $84.4x73.0x0.0508mm$) measured at point A due to the pure torsion actuation on both bimorphs.

4.3.2 Nonlinear MFC energy harvesting tests

Recently, Tan, Yavarow and Erturk (2018) presented the nonlinear modeling and experimental results of electromechanically coupled systems with MFCs as showed in Section 2.1. To experimentally validate the theoretical model of chapter 3 in an energy harvesting case, the experimental results for a bimorph structure presented by Tan, Yavarow and Erturk (2018) is used as a reference. Two MFC laminates (M8507-P1, from Smart Material Corp.) were vacuum bonded together without a substrate to form a bimorph structure (figure 31). The structure has an overall dimensions of $83.50mm$ (length), $10.00mm$ (width), $0.61mm$ (thickness) and the active area has a clamped length of $75.50mm$ and width of $7.00mm$. The measured capacitance of the structure was $3.40nF$.

The bimorph structure was tested in base excitation, the root mean-square (RMS) acceleration level was set to $0.5g$ and sweeping the excitation frequency up and down was performed around the first short circuit natural frequency of the beam. The frequency sweep was repeated for $0.4g$, $0.3g$, $0.2g$, and $0.1g$ RMS base acceleration levels. The tip velocity of the MFC bimorph was measured around the mid point (in the length direction) of the cantilever. Although the authors tested the nonlinear electroelastic behavior of the cantilever considering several different resistances connected to the MFCs (for electrical power estimation in their energy harvesting case), the resistance of 1.3 MΩ was observed as the optimum one (for maximum electrical power output) and will be considered in this section.

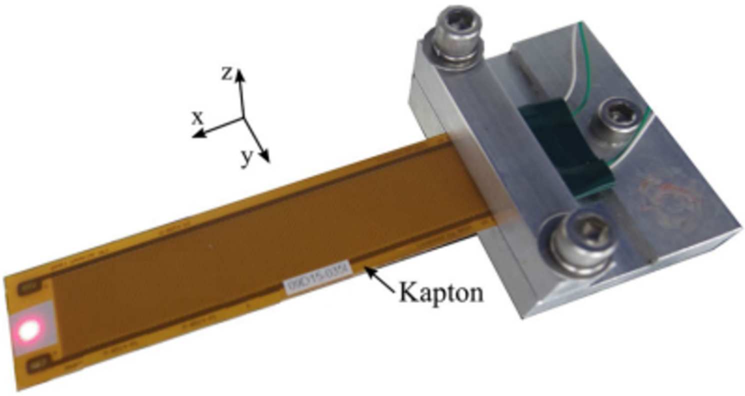

Figure 31 – MFC bimorph cantilever presented in Tan, Yavarow and Erturk (2018).

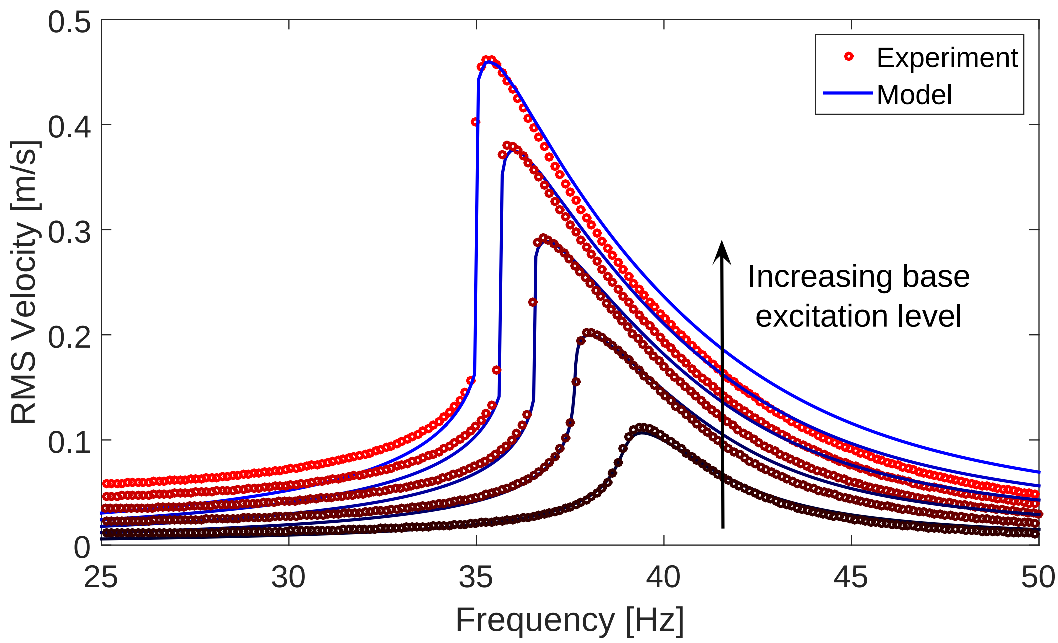

Figure 32 – Measured RMS tip velocity of the MFC bimorph versus frequency at RMS base acceleration levels of 0.1g, 0.2g, 0.3g, 0.4g, and 0.5g using a downward frequency sweep (increasing base acceleration level from black to red dots - (TAN; YAVAROW; ERTURK, 2018)) compared to numerical model results (increasing base acceleration level from black to blue lines) considering a 1.3 MΩ resistance in the electrical circuits.

Figures 32 and 33 displays the frequency response of tip displacement and electrical power output when the optimum load resistance is considered and for increasing base acceleration. To properly predict the nonlinear backbone in the experiments, the nonlinear terms that compose the nonlinear stiffness matrix (equation 3.52) were adjusted as $\alpha = 0.365$, $\beta = 1.15$ and $\tau = -1.3$.

Figure 32 displays the experimental tip velocity (TAN; YAVAROW; ERTURK, 2018) and the numerical predictions from the nonlinear numerical model of this work (nonlinear geometric model and nonlinear piezoelectricity). The softening behavior is clearly observed for all excitation levels. The resonance frequency decreased from $40.5Hz$ to $30.3Hz$ with increasing base acceleration level due to the softening behavior of the piezoelectric material. Clearly in figure 32, the backbone curve is different from the ones previously reported in the literature for typical piezoceramics mostly due to complex behavior of the MFCs. One should note that the numerical predictions successfully represent the experimental responses. The backbone was properly predicted for the complete range of considered base excitation levels.

The electrical power output (defined as $P_{avg} = v_{p,RMS}^2/R_l$) is displayed in figure 33 for the optimal resistance (R=1.3 MΩ) and increasing base acceleration levels. Once again the backbone curve is predicted and the numerical results are in good agreement with the experimental ones. The numerical model slightly overpredicts power the output for higher base aceleration levels. This discrepancy is likely due to other dissipative terms in the electrical domain (e.g., dielectric loss) not accounted for in the present model. In all cases showed here, large displacements model considering Green-Lagrange strain was considered.

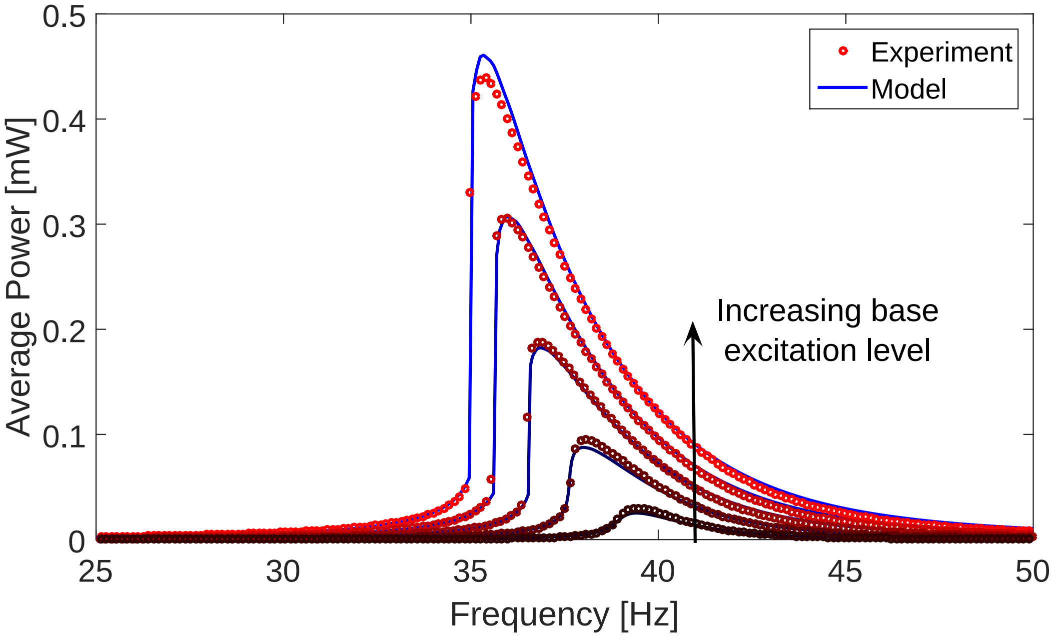

Figure 33 – Measured average power output of the MFC bimorph versus frequency at RMS base acceleration levels of 0.1g, 0.2g, 0.3g, 0.4g, and 0.5g using a downward frequency sweep compared to numerical model predictions considering a 1.3 MΩ resistance in the electrical domain.

4.4 Wind energy harvesting results

Having validated the nonlinear numerical model presented in this work in the previous section, a wind energy harvesting investigation is performed in this section. The nonlinear parameter for the piezoelectric material used in section 4.3.1 are also considered in this study with a double bimorph structure under wind excitation. The nonlinear piezoaeroelastic model is obtained by combining the Doublet Lattice Model for unsteady aerodynamics presented in section 3.4.1 with the nonlinear electroelastic model (nonlinear structure and nonlinear piezoelectricity). Once calculated the aerodynamic matrices with the linear structural model, the linear model is replaced by the nonlinear finite element model with a geometric nonlinearity (related to large displacements) as well as considering nonlinear piezoelectricity. The nonlinear stiffness (equation 3.74) is combined to the piezoaeroelastic equation 3.81 for numerical simulations, which is updated at each time step. In such case, nonlinear aeroelastic system is obtained and the model predicts limit cycle oscillations (LCOs) for a range of airflow speeds starting at 45.40 m·s^{-1} when a load resistance of 1 MΩ is considered.

The nonlinear stiffness (equation 3.74) is combined to the piezoaeroelastic equation 3.81 for numerical simulations, which is updated at each time step. In all cases investigated in this section, the initial conditions remain constant and they are considered as a combination of 1 mm amplitude of the first bending linear modal shape and 0.1 mm amplitude of the first torsion linear modal shape of each analyzed structure. Also, the aerodynamic coefficient matrix is obtained considering the first ten linear modes. The main motivation in this section is to verify the effects of piezoelectric nonlinearities on the wind energy harvesting performance of plate-like wings. First, a low aspect ratio wing is considered and then, a different wing (with higher aspect ratio) is investigated.

4.4.1 Wind energy harvesting considering a low aspect ratio plate

In the numerical studies of this subsection, the flexible plate presented in subsection 4.2 is considered. The resulting nonlinear electroaeroelastic structure are investigated for a range of airflow speeds by combining a structural model with the DLM. When a linear structural model

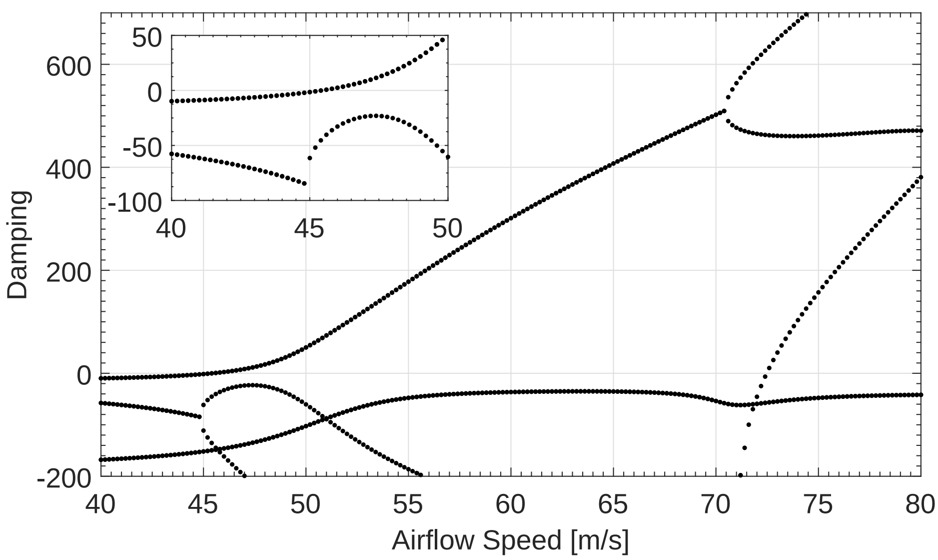

Figure 34 – Theoretical damping behavior of the linear plate-like wing model (84.4*x*73.0*x*0.0508*mm*) for increasing airflow speeds considering a load resistance of 1 MΩ.

is considered, the linear electroaeroelastic behavior of the system can be predicted for different airflow speeds. In particular, the damping behavior of different model with increasing airflow speed can be obtained, as displayed in Figure 34. The damping behavior, provided by the real part of the system eigenvalues and obtained from the the linear numerical model (Kircchhoff assumptions and linear piezoelectricity), for increasing airflow speed is displayed in figure 34. In such case, a load resistance of 1 MΩ was assumed as the electrical boundary condition of each MFC. The linear flutter speed of the plate, which corresponds to the neutral stability boundary of the system and refers to a hard crossing, is 45.40 $\mathrm{m{\cdot}s^{-1}}$(displayed at the zoomed area in figure 34).

The main motivation here, however, is to investigate the effects of piezoelectric nonlinearity on the electroaeroelastic behavior. Therefore, the linear structural model was replaced by the nonlinear finite element model with a geometric nonlinearity (related to large displacements) as well as considering nonlinear piezoelectricity. The nonlinear model was then combined to the DLM model for numerical simulations. In such case, nonlinear aeroelastic system is obtained and the model predicts limit cycle oscillations (LCOs) for a range of airflow speeds starting at 45.4 m/s when a load resistance of 1 MΩ is considered. Later in the simulations, several different load resistances are assumed individually connected to each MFC for energy harvesting to estimate the electrical power output. The considered resistance values were 1 Ω, 100 kΩ, 1 MΩ, and 10 MΩ. The predicted displacements (measured at the tip leading edge) are shown in figure 35(a) and (b) for the assumed load resistances considering linear and nonlinear MFC models, respectively. The main difference is observed around the cut in speed for LCOs when different load resistances are considered. The critical airflow speeds for LCOs slightly changes for different load resistances. The Hopf bifurcations for each resistance case are supercritical (DIMITRIADIS, 2017).

(a)

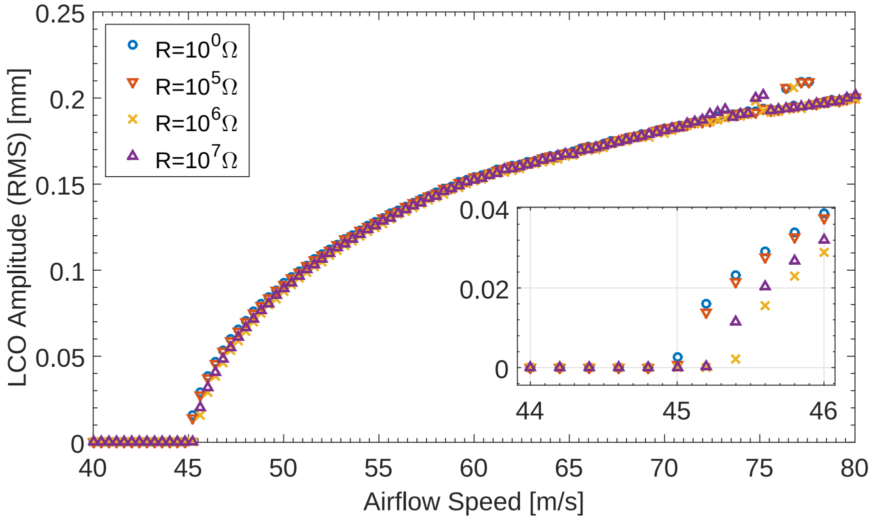

(b)

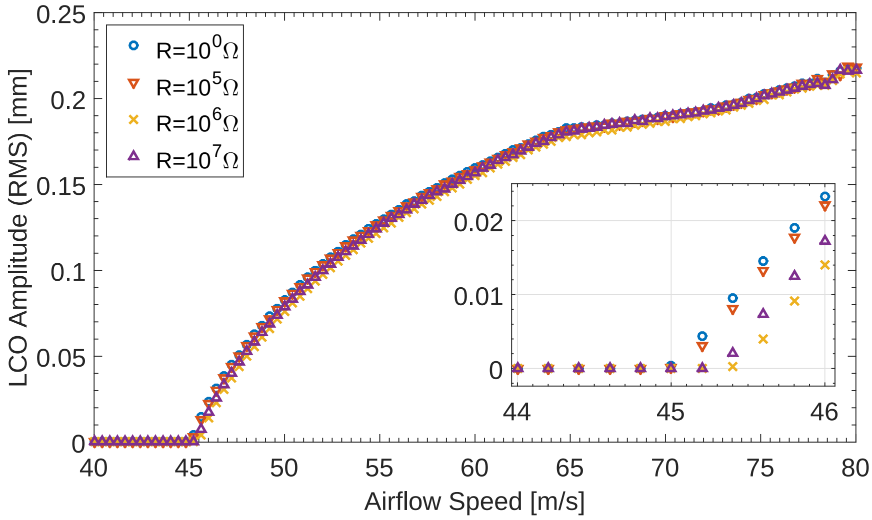

Figure 35 – Predicted RMS tip displacement (84.4*x*73.0*x*0.0508*mm* wing) for increasing airflow speeds, considering (a) linear and (b) nonlinear MFC models for load resistances of 1 Ω, 100 kΩ, 1 MΩ, and 10 MΩ.

Figure 36 displays the tip displacement for the optimum load resistance of 1 MΩ for maximum power output. The optimum load was determined from Figure 37 that will be later discussed. Linear and nonlinear electrical cases are shown in Figure 36 for comparison purposes (in both cases the nonlinear geometric model is considered). Tip displacement are smaller for the nonlinear piezoelectric case then for the nonlinear piezoelectric case for airflow speeds smaller than 57.00 m·s^{-1}. For larger airflow speeds, tip displacement for the nonlinear case are larger than for the linear case.

The power output strongly depends on the load resistance assumed in the electrical domain,

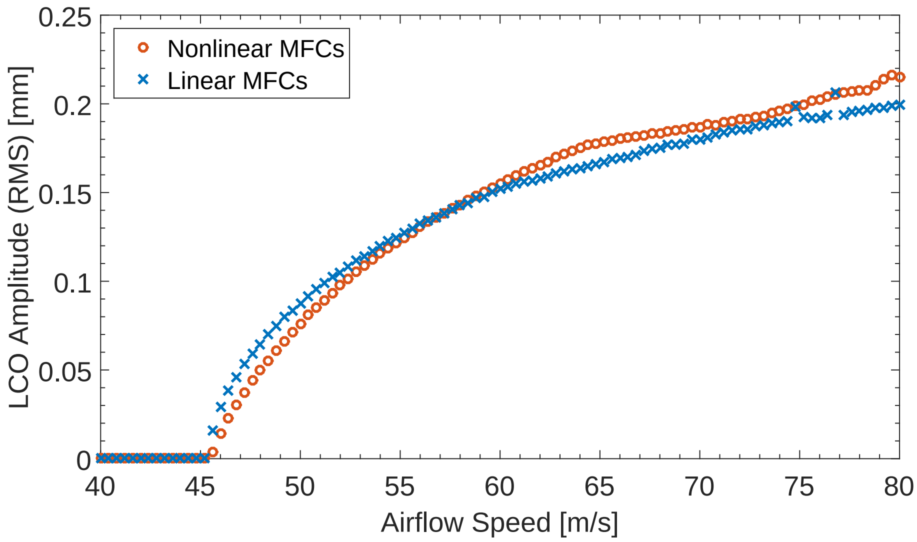

Figure 36 – RMS wing (84.4x73.0x0.0508mm) tip displacement comparison between linear and nonlinear MFC models for increasing airflow speeds considering a load resistance of 1 MΩ.

as shown in figures 37(a) for linear MFC model and 37(b) for nonlinear MFC model. The reported values of power output represent the total power obtained from the summation of all four circuits. In both (linear and nonlinear) cases, the maximum average power output was predicted for the load resistance of 1 MΩ. For the same load resistance of 1 MΩ, figure 38 shows that the maximum average power output is larger when the nonlinear MFC model is considered. Clearly, the maximum power output from this wind energy harvesting case is significantly affected by nonlinear piezoelectricity.

(a)

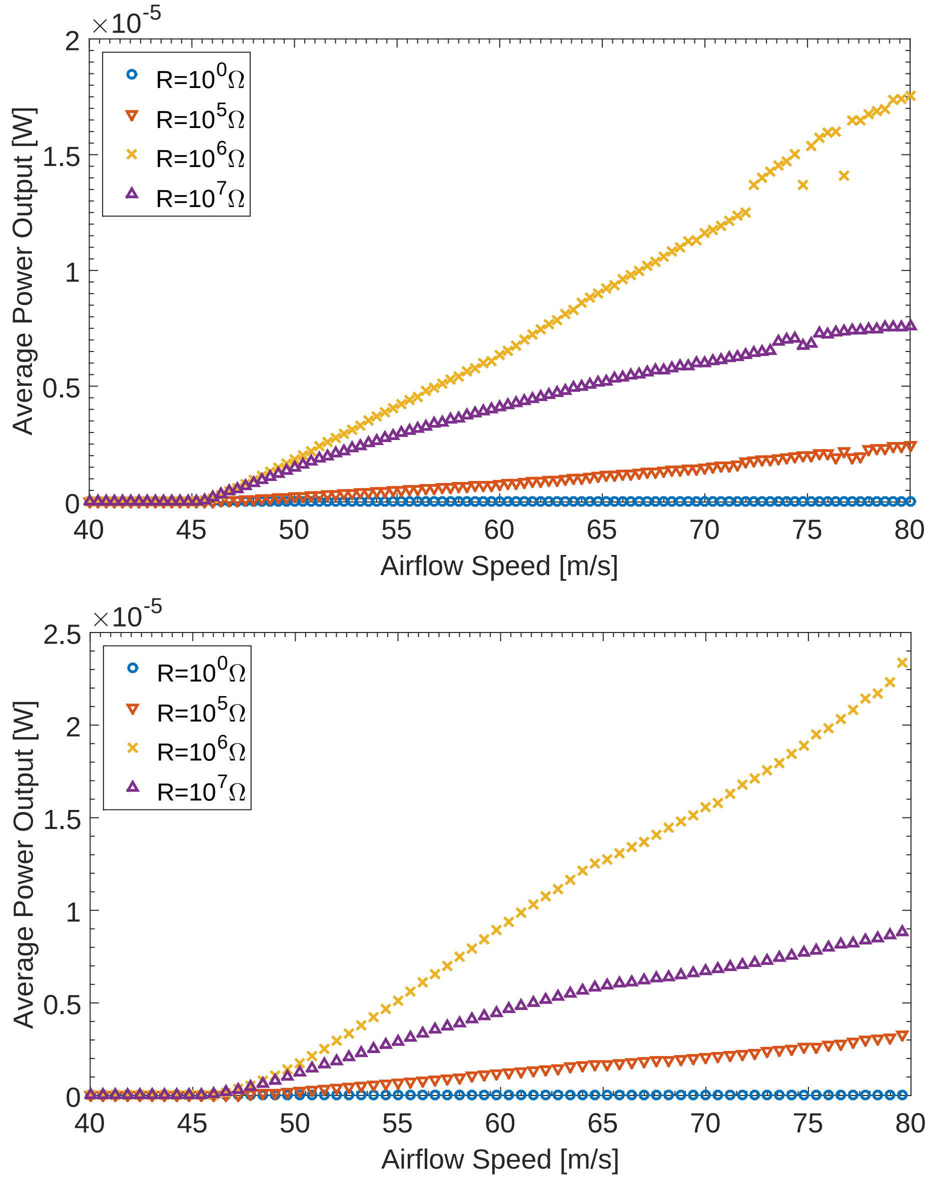

Figure 37 – Predicted average power output in the energy harvesting case (84.4*x*73.0*x*0.0508*mm*), considering (a) linear and (b) nonlinear MFC models.

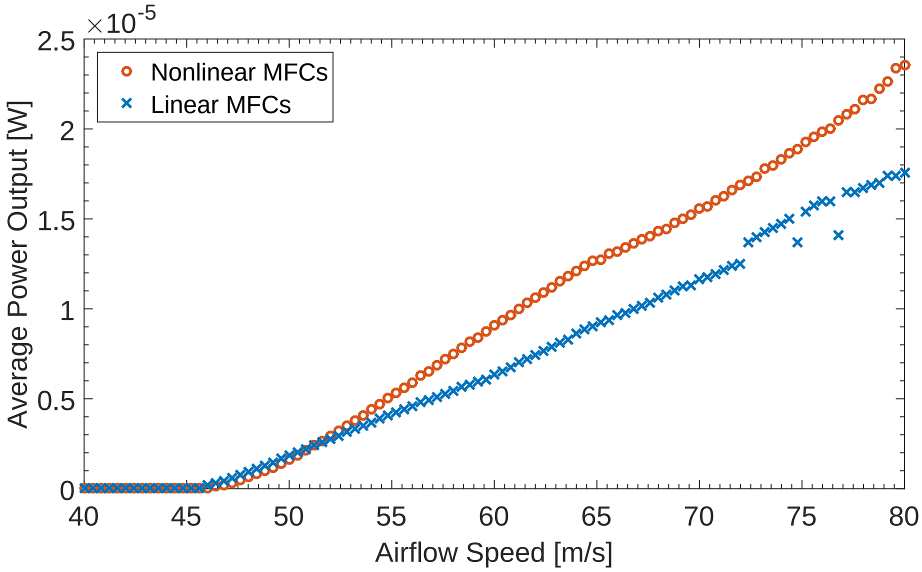

Figure 38 – Average power output comparison between linear and nonlinear MFC models in the energy harvesting case (84.4*x*73.0*x*0.0508*mm* wing) for the load resistance of 1 MΩ.

4.4.2 Higher aspect ratio aeroelastic analysis

The model considered in this subsection is a clamped-free stainless steel plate with $193GPa$ elastic modulus, $7850kg/m^3$ density, and dimensions $168.8x56x0.0508mm$. The span is chosen to be two times the span considered in the previous subsection and the thickness remains the same as studied in the previous subsection (4.4.1). The chord was chosen as four times the size of the MFC active area, resulting in an aspect ratio close to three. As mentioned, the same nonlinear parameters considered in the previous section are assumed in the present case.

Theoretical MFC bimorphs (with same properties of $M8514-P1$) are considered bounded to the wing surfaces at the leading and trailing edges. The length of the bimorphs are considered in the same way as the span of the wing resulting in $152.7mm$ of length, while the width remains the same as the MFC active area ($14mm$). Once again the same initial conditions are applied to the system and the results are analyzed considering linear and nonlinear behavior of the piezoelectric material.

First, Figure 39 presents the evolution of the damping (real part of the system eigenvalue) with increasing airflow speed for a load resistance of 1 MΩ in each electric circuit. The damping

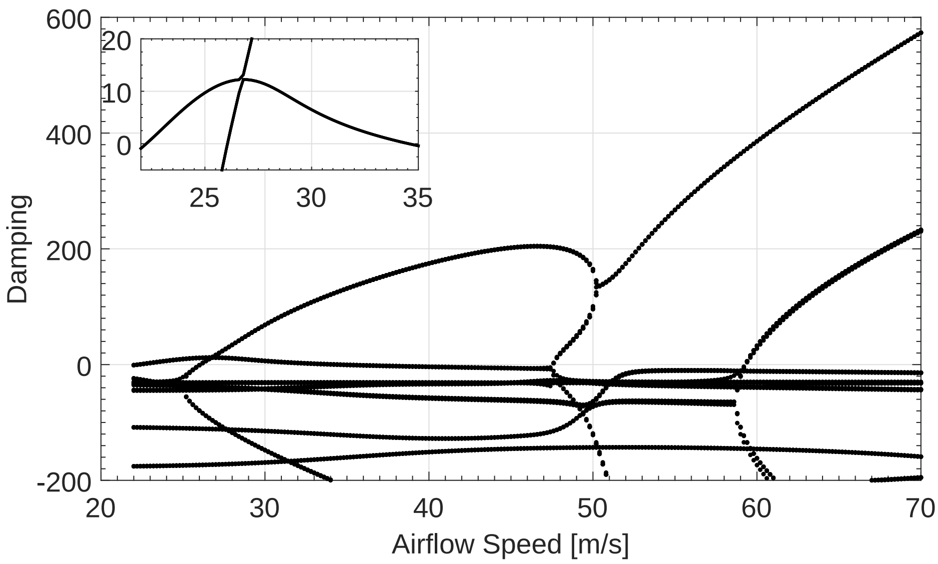

Figure 39 – Damping variation with the increment of flow speed for the linear model of stainless steel wing plate ($168.8x56x0.0508mm$) double bimorph considering the highest power output resistance, 1 MΩ.

is zero for the velocity of $22.30m/s$, defined as the critical velocity of flutter for this wing. In this case, the first crossing refers to a hump mode, and a hard crossing can be observed at $26.05m/s$ (displayed at the zoomed area in Figure 39).

LCOs are predicted when the nonlinaear geometric model is considered. The critical airflow speed for LCOs is observed at the linear flutter speed. The load resistances, in each electric circuit, are chosen as 10 Ω, 10 KΩ, 100 KΩ, 1 MΩ, 10 MΩ. It is worthy to mention here

(a)

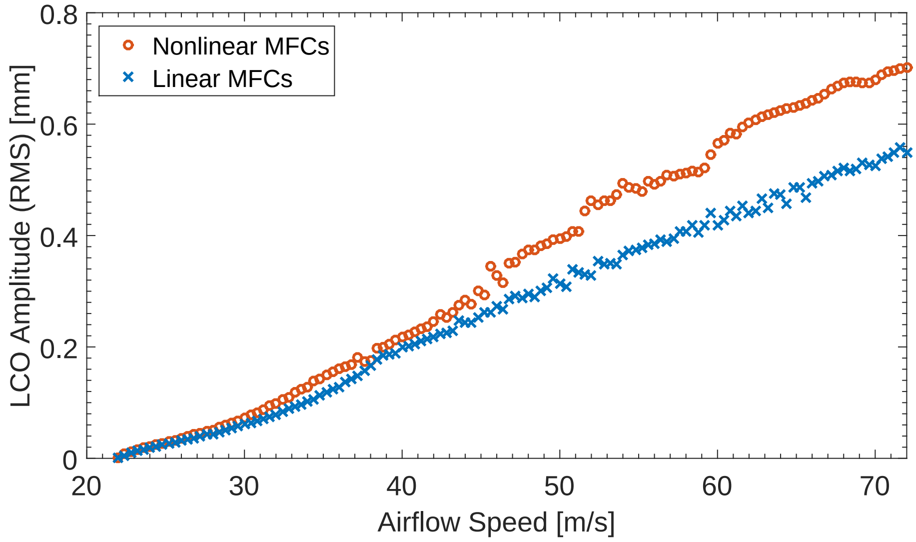

(b)

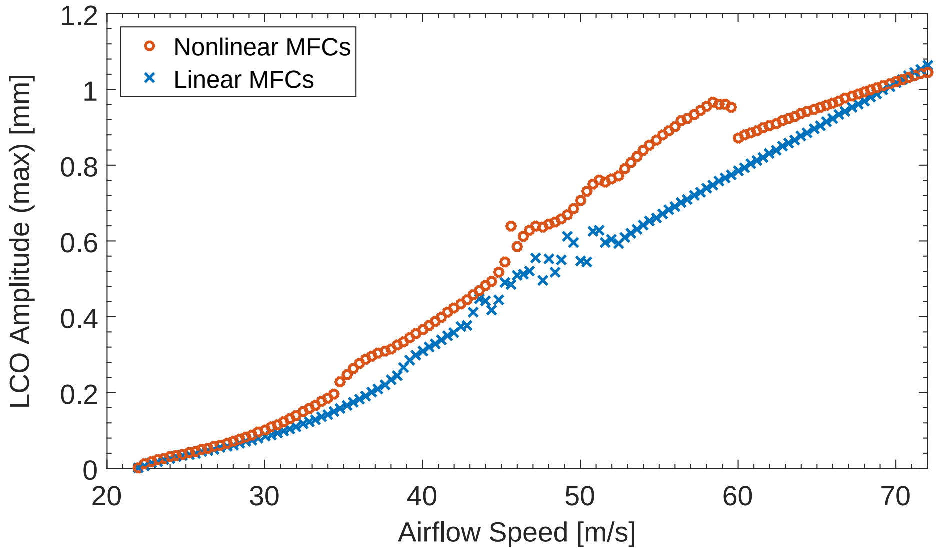

Figure 40 – (a) RMS and (b) maximum trailing edge tip corner transverse displacement comparison between linear and nonlinear MFC with the increment of flow speed for the stainless steel wing plate ($168.8x56x0.0508mm$) double bimorph considering the highest power output resistance, 1 MΩ.

that other circuits and electrical component configurations have a better output results (SILVA; JUNIOR, 2016), however this is not the main goal in this research.

Figures 40(a) and (b) displays the RMS and maximum tip displacement for increasing airflow speed and load resistenances of 1 MΩ connected to the MFCs. In this case, the simulations assuming linear piezoelectricity underestimates the amplitude of LCOs (when compared to the results assuming nonlinear piezoelectricity). The softening behavior of MFCs leads to larger

(a)

(b)

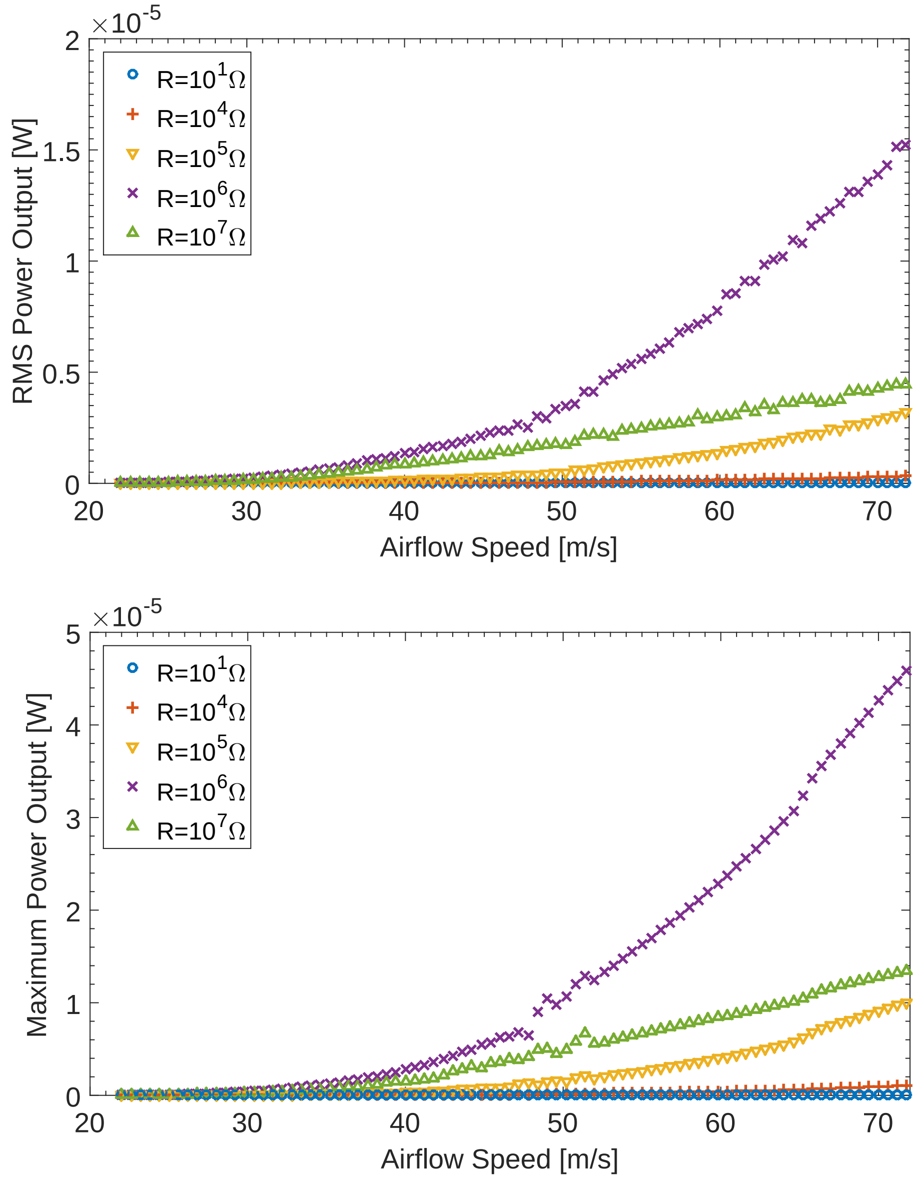

Figure 41 – LCO energy harvesting (a) RMS and (b) maximum power output considering linear MFCs and the stainless steel wing plate ($168.8x56x0.0508mm$) double bimorph for the variation of flow speed and electrical resistances.

mechanical amplitudes.

Figures 41 and 42 displays the power output with increasing airflow speeds and for a set of load resistances when linear (Figure 41) and nonlinear piezoelectricity (Figure 42) are considered. As in the previous case, power output increases (in both cases of linear and nonlinear piezoelectricity) with increasing airflow speed. For each airflow speed, power increases with increasing load resistance until the optimum load of 1 MΩ is considered. Then, power decrea-

(a)

(b)

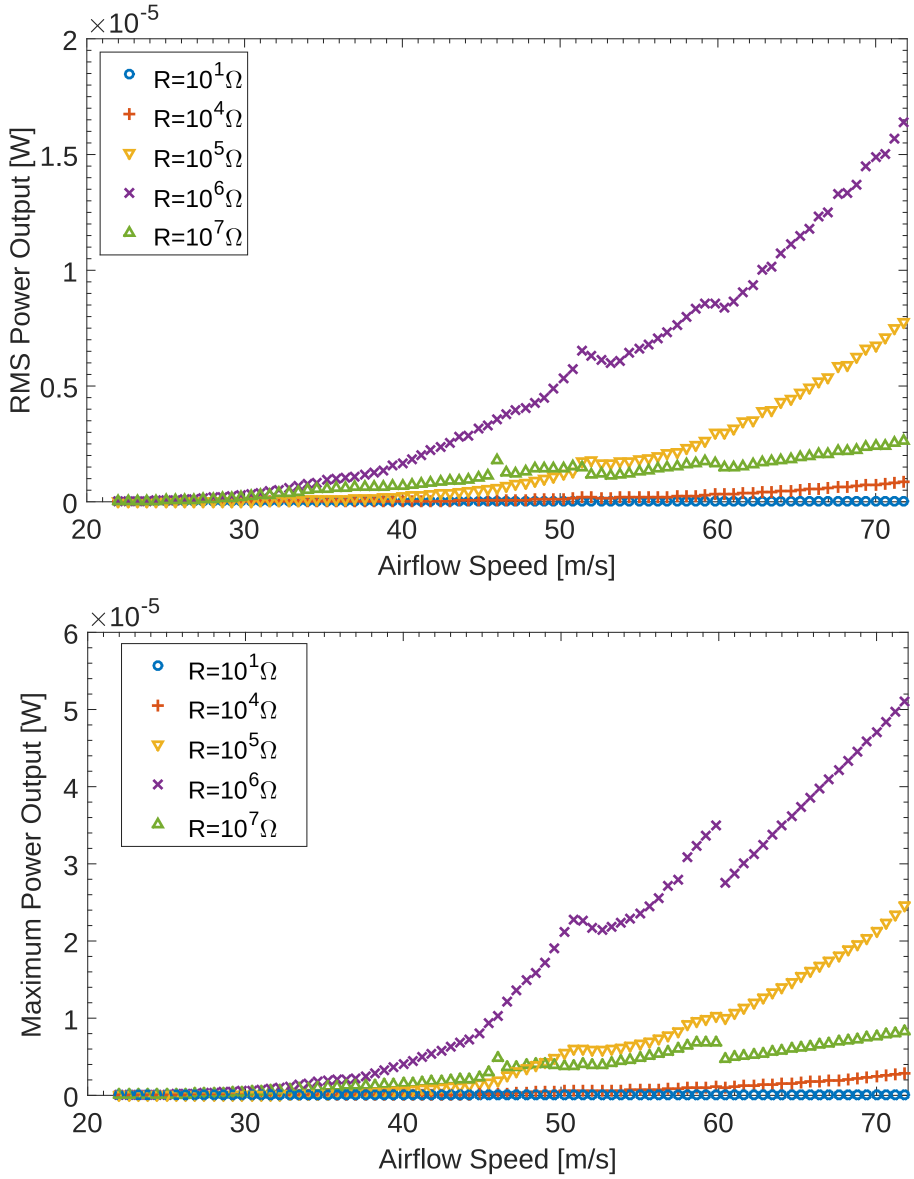

Figure 42 – LCO energy harvesting (a) RMS and (b) maximum power output considering nonlinear MFCs and the stainless steel wing plate (168.8*x*56*x*0.0508*mm*) double bimorph for the variation of flow speed and electrical resistances.

ses with further increase of load resistance. Therefore, the optimum load resistance that delivers the maximum power output is 1 MΩ for both linear and nonlinear piezoelectricity. For speeds higher than $50m/s$ the system displays some Torus bifurcations (DIMITRIADIS, 2017) when nonlinear piezoelectricity is considered.

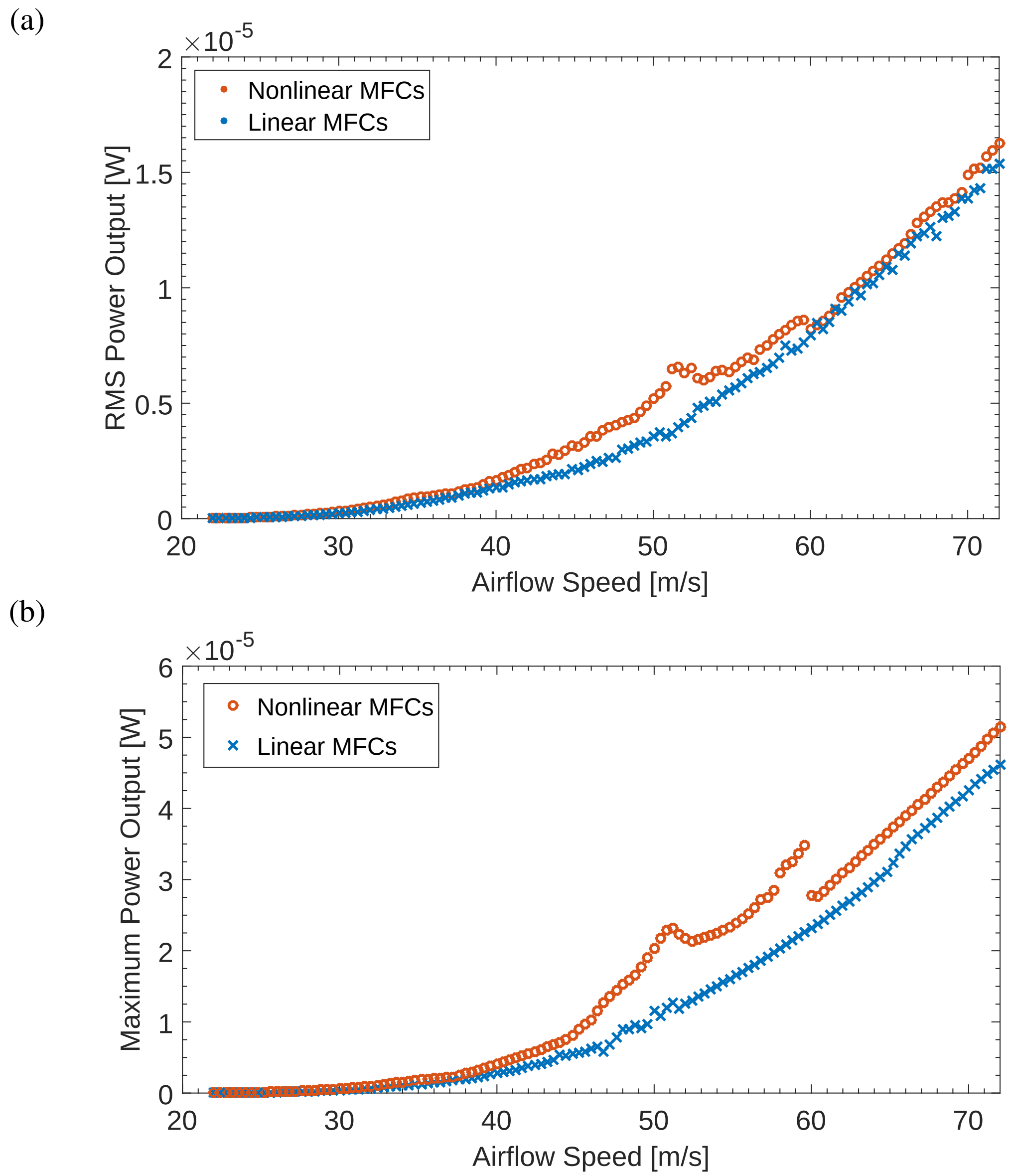

Figure 43 – LCO energy harvesting (a) RMS and (b) maximum power output comparison between linear and nonlinear MFC behavior for the stainless steel wing plate ($168.8x56x0.0508mm$) double bimorph with the increment of flow speed for the optimal resistance, 1 MΩ.

Figure 43(a) and 43(b) shows the power output with increasing airflow speed considering linear and nonlinear piezoelectricity, respectively, and considering the optimum load resistance of 1 MΩ. A noticeable increase of the power harvested is observed around $51m/s$ for the maximum and RMS values for the nonlinear MFC behavior. This behavior results from the combination of MFC exponential softening and geometric quadratic hardening that induces bifurcations increasing the power output of the system. On the other hand, power output drops around the airflow speed of $60m/s$ due to Pitchfork bifurcations (DIMITRIADIS, 2017) when nonlinear piezoelectricity is considered. For the range of airflow speeds considered, the predicted power output is always larger when nonlinear pieozoelectricity is considered.

As an example of Pitchfork bifurcation, the phase projection of the LCO for the linear and nonlinear MFC behavior at the airflow speed of $72m/s$ is displayed in figure 44. Note that in figure 44 that the system oscillates around the equilibrium point that is different from zero when nonlinear piezoelectricity is assumed while the system oscillates around zero for the linear piezoelectricity assumption

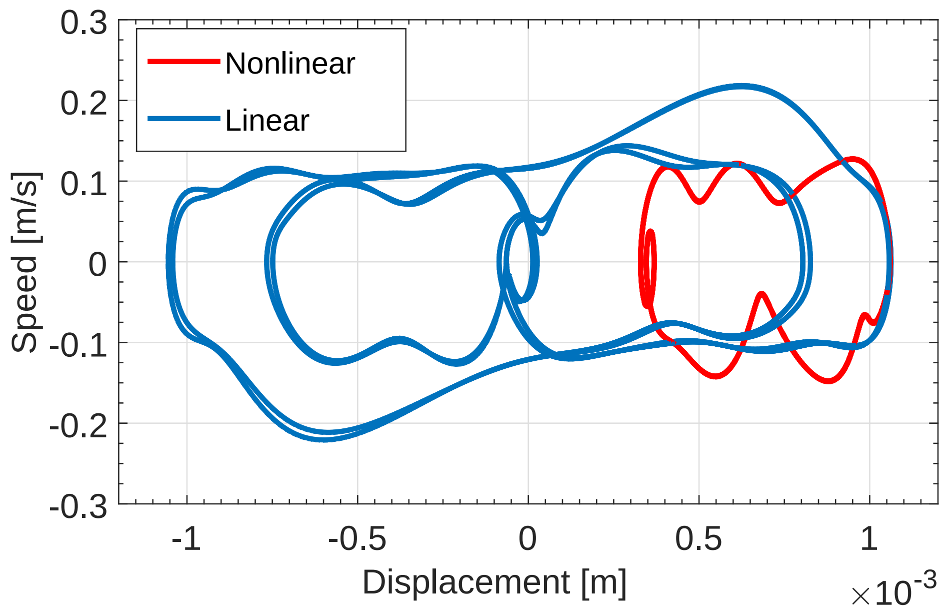

Figure 44 – Phase projection comparison of the leading edge tip corner stainless steel wing plate ($168.8x56x0.0508mm$) double bimorph considering linear and nonlinear MFC behavior for flow speed of $72m/s$ with electrical circuits connected to 1 MΩ resistances.

4.5 Aeroelastic control using active stiffness change

In this section, stiffness variation without shape change due to DC voltage input applied to the MFCs of the double bimorph structure reported in section 4.2 is investigated. Positive DC voltage input acts as a tensile load while negative DC voltage input represents a compressive load on the overall structure. In the first case the effect is stiffness increase while in the second is stiffness reduction. The main goal in this section is to numerically investigate the effects of stiffness change induced by MFCs actuation on the aeroelastic behavior of the double bimorph. Initially in this section the finite element model results are verified agaist the experimental results of Samur (2013). The author investigated the same double bimorph structure considered in this section by applying different in phase and constant DC voltage levels to all MFCs. Therefore, stiffness is modified and shape is not changed.

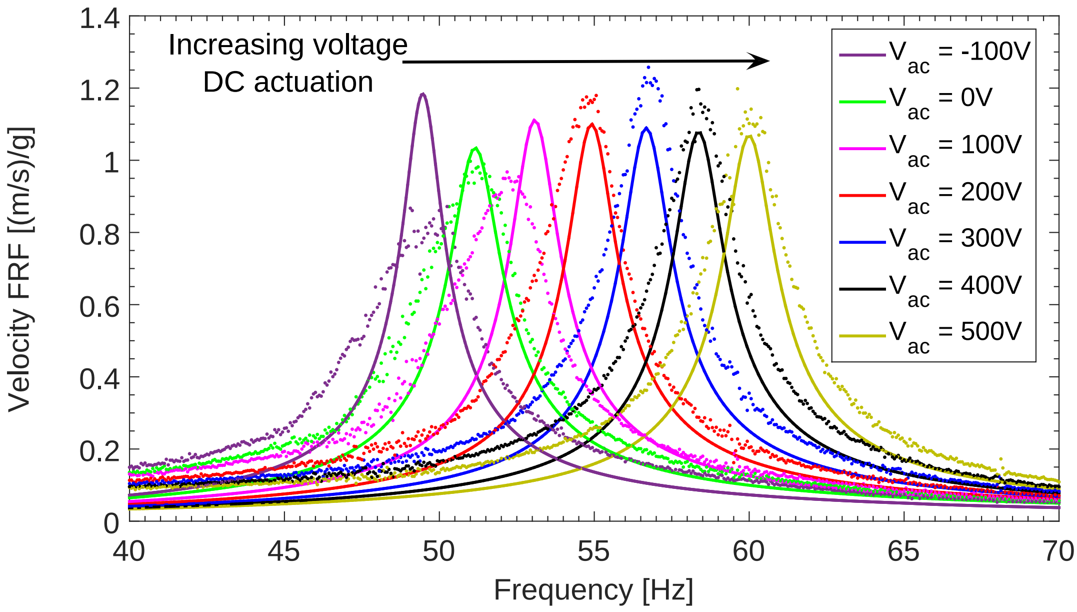

Figure 45 – Tip velocity to base acceleration FRFs for each level of DC voltage input to the double bimorph with solar panel substrate to change the stiffness. Dots are experimental results presented by (SAMUR, 2013) while solid lines represent model results from this work.

Figure 45 shows the velocity FRF (defined in this work as the ratio of tip velocity to base acceleration) for different DC voltage input to the MFCs. For each DC voltage input, the double bimorphs was base excited and the velocity response on the tip was experimentally obtained by

Samur (2013). Base excitation was provided by electromagnetic shaker, and an accelerometer was attached to the clamp to measure the base acceleration simultaneously while a laser doppler vibrometer was used to measure tip velocity. A good match between numerical predictions and experimental behavior is observed in Figure 45 for a certain range of DC voltage inputs. As the DC voltage input to MFC increases, the natural frequency changes significantly as a result of the stiffness change.

4.5.1 Active aeroelastic control

In this subsection, the effects of active stiffness control on the aeroelastic behavior of the double bimorph is investigated. Therefore, the finite element model is combined to the unsteady aerodynamic model (DLM) to obtain the piezoaeroelastic model. In this case, the DLM method is used to generate the aerodynamic influence matrix (as described in section 3.4.1) that has to be recalculated due to plane stresses induced by the DC voltage input to the MFCs bimorphs. The variation on the stress matrix (induced by actuation) results in a change in the tangent stiffness matrix which is used to calculate the aerodynamic influence matrix in the DLM.

The model considered in this subsection is the double bimorph with stainless steel substrate ($84.4x73.0x0.0508mm$). Two MFC bimorph (with $M8514-P1$) are considered bounded to the wing surfaces at the leading and trailing edges. This configuration is the same presented in subsection 4.2 however the $3mm$ borders (innactive width arround the MFCs) are neglected and the MFC active area is considered at the leading and trailing edge. The linear flutter speed of this configuration was numerically obtained as $41.5m/s$. Geometric nonlinearity will be considered in all cases in this subsection. The initial conditions remains constant and will be considered as a combination of $1mm$ amplitude of the first bending linear modal shape and $0.1mm$ amplitude of the first torsion linear modal shape for each configuration proposed in this subsection.

In order to investigate the effects of stiffness change on the aeroelastic behavior of the double bimorph, DC voltage inputs of $-100V$, $100V$, $200V$, $300V$, and $400V$ were considered. Moreover, the case without DC voltage input was assumed as the reference case. For each DC input voltage, the nonlinear displacements were evaluated and then the tangent stiffness (eq.

3.73) updated. The tangent stiffness for each actuation is used to calculate the aerodynamic coefficients for airflow speeds ranging from $40m/s$ to $50m/s$.

Figure 46 shows the variation of tip displacement calculated at the leading edge corner of the structure with increasing airflow speed and different DC input voltages ($-100V$, $0V$, $100V$, $200V$, $300V$, and $400V$) when both the linear and nonlinear MFC models are considered (Figure 46 a and b, respectively). One should note that the aeroelastic behavior is less sensitive to DC

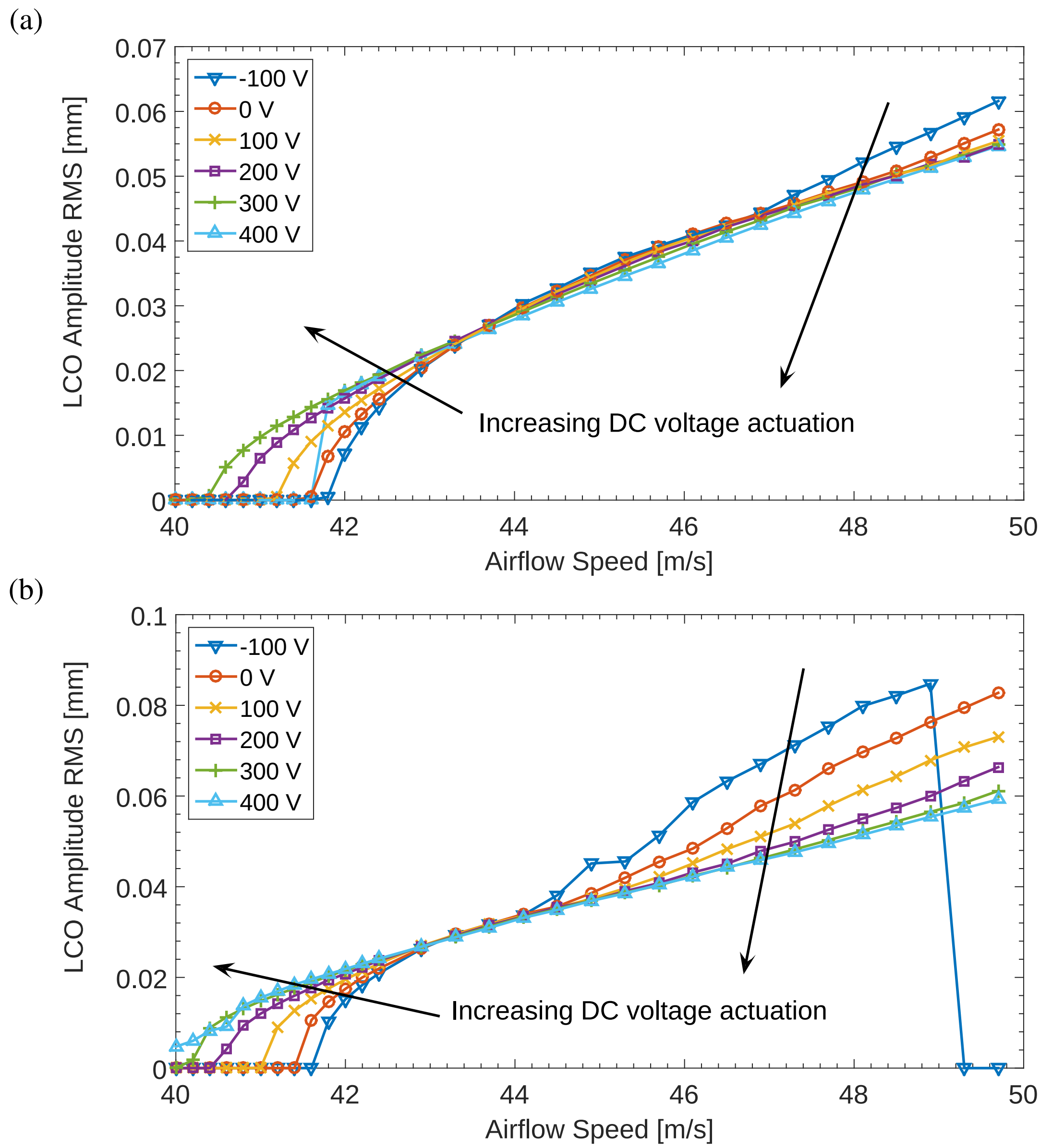

Figure 46 – RMS wing ($84.4x73.0x0.0508mm$) tip displacement considering (a) linear and (b) nonlinear MFC behavior for increasing airflow speeds and increasing in plane actuation of $-100V$, $0V$, $100V$, $200V$, $300V$, and $400V$.

input voltage when linear piezoelectricity is considered. In both cases (linear and nonlinear piezoelectricity), increasing positive DC input voltages reduces the cut in speeds for LCOs while negative DC input voltage slightly increases the cut in speed. On the other hand, the increasing stiffness due to positive input DC voltages in the nonlinear case (nonlinear piezoelectricity) reduces the amplitude of LCOs for larger airflow speeds.

Having verified the effects of DC input voltage on the elastic behavior of the double bimorph, the aeroelastic behavior is then investigated. The aeroelastic behavior in the absence of DC input voltage is assumed as the reference case. Figure 46b shows that the cut in speed of the reference case is close to $41.5m/s$ as well as shows that this cut in speed only increases when $-100V$ is considered. Therefore, Figure 47 displays the time response of tip displacement (leading and trailing edges) for the airflow speed of $41.7m/s$. For the first 5 seconds no DC input was applied to the MFCs, therefore, according to Figure 46 the system should present LCOs (as displayed in Fig. 47). After the time of 5 seconds in Fig. 47, $-100V$ was applied to the MFCs. According to Figure 46, the cut in speed for LCOs for $-100V$ is slightly larger than $41.7m/s$. Therefore, LCOs are suppressed in Figure 47 after 5 seconds. Since the effect of negative DC input voltage is to reduce bending stiffness, we believe that this effect justifies the enhanced

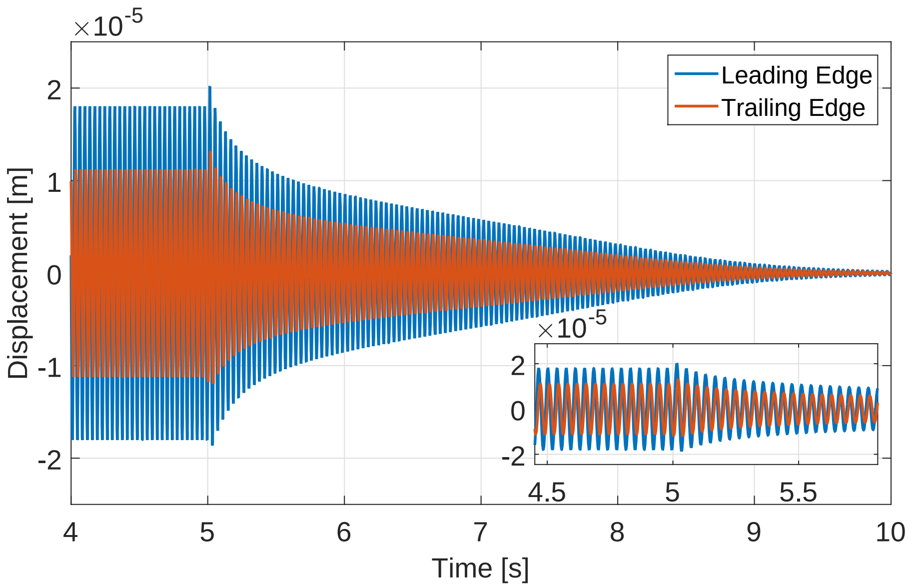

Figure 47 – Time response of tip displacement considering nonlinear MFC behavior, flow speed of $41.7m/s$ and $-100V$ actuation at $5s$ (stainless steel substrate - $84.4x73.0x0.0508mm$).

aeroelastic behavior since increasing the distance (in frequency) between bending and torsion modes in general results in coalescence at higher airflow speeds. Although not shown the motions in the LCOs are due to combined bending and torsion motions. Therefore, the effects of increasing negative DC inputs on the cut in speed should be investigated. Furthermore, out of phase DC inputs to the MFCs (not investigated in this work) could result in combined effects of aeroelastic control and also shape control, leading to morphing wind cases.

Figure 46b also shows that the LCOs amplitudes of the reference case are larger compared with the 400V actuated case for airflow speeds higher than 43m/s. Figure 48, for example, displays the time response of tip displacement (leading and trailing edges) for the airflow speed of 50.0m/s. For the first 5 seconds no DC input was applied to the MFCs, then 400V was applied to the MFCs. Therefore, LCOs amplitudes are reduced in Figure 48 after 5 seconds. Furthermore, an increase in the frequency of the aeroelastic response is also observed since the wing undergoes a hardening actuation.

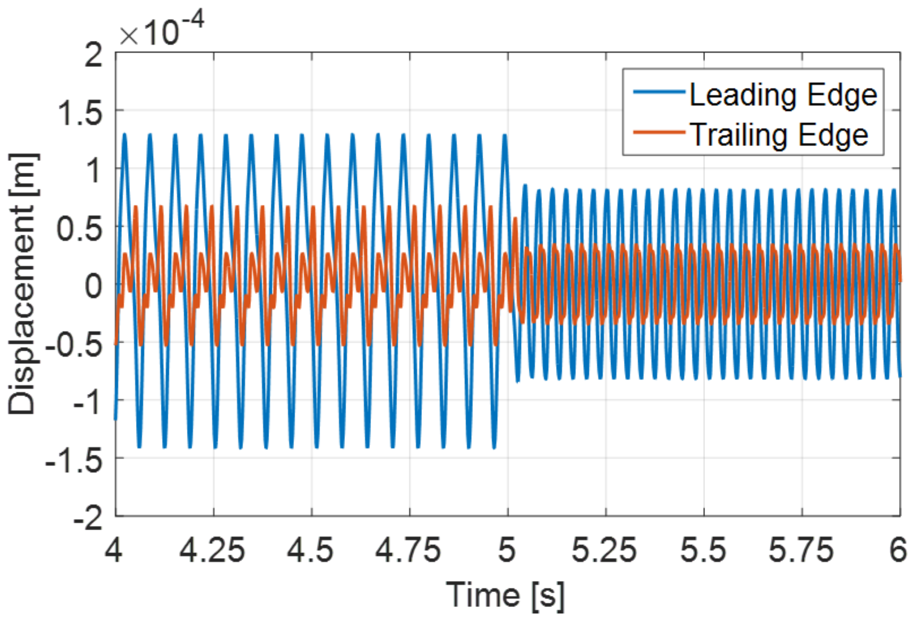

Figure 48 – Time response of tip displacement considering nonlinear MFC behavior, flow speed of 50.0m/s and 400V actuation at 5s (stainless steel substrate - 84.4x73.0x0.0508mm).

Another interesting point displayed in Figure 46b is that LCOs are not present when the $-100V$ actuation is considered for airflow speeds higher than 49m/s, within the studied values and accounting with nonlinear MFC behavior. As an example, Figure 49 displays the time response of tip displacement (leading and trailing edges) for the airflow speed of $50.0m/s$. Once again, the first 5 seconds no DC input was applied to the MFCs, after the time of 5 seconds $-100V$ was applied to the MFCs. Therefore, LCOs are suppressed in Figure 49 after 5 seconds and the wing converge to a deformed shape.

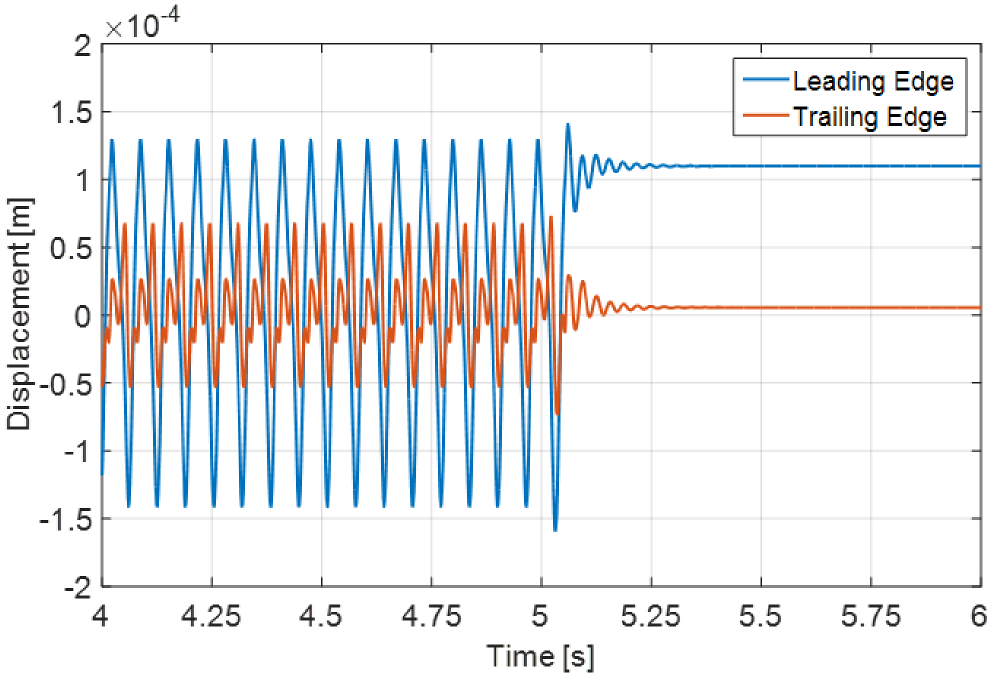

Figure 49 – Time response of tip displacement considering nonlinear MFC behavior, flow speed of $50.0m/s$ and $-100V$ actuation at $5s$ (stainless steel substrate - $84.4x73.0x0.0508mm$).

CHAPTER 5

Summary and Conclusions

5.1 Conclusions and Reccomendations for Future Work

This dissertation present a linear and a nonlinear electroelastic model developed based on finite element analysis for electromechanically coupled structures. A finite element model was developed considering linear (considering Kirchhoff plate assumptions) and nonlinear (using Von Karman's approximation) geometric model. The aerodynamic is modeled with the Doublet Lattice method and the aeroelastic coupling is presented. The most relevant point presented in this work is the modeling of the nonlinear behavior of MFCs.

Most of the nonlinear piezoelectric models presented in the literature considered beam model. In this work, nonlinear piezoelectricity was expanded to plate models. Moreover, a new model for the MFC nonlinear behavior based a new expression for enthalpy, was presented. Numerical results for pure bending actuation case were successfully verified against experimental data. Results for a bimorph base excited energy harvester (from the literature) were also successfully predicted by the nonlinear proposed model. The nonlinear geometric finite element developed was also tested against nonlinear Comsol and Abaqus results (well know available commercial softwares).

The nonlinear model was combined to an unsteady aerodynamic model and aeroelastic simulations were performed for wind energy harvesting and wing stiffness change cases. First, wind energy harvesting cases were simulated. The MFCs were connected to separate load resistance in order to estimate the power output from limit cycle oscillations. This is a relevant contribution since all the previous wind energy harvesting cases in the literature assumed linear piezoelectricity. According to model predictions, piezoelectric softening increases the electrical power output due to larger oscillations. The exponential softening also induces the appearance of Hopf bifurcations, leading to larger displacements. The softening behavior is reduced when the substructure becomes thicker. The experimental verification (wind tunnel tests) of the nonlinear wind energy harvesting behavior is recommended as a future work.

The effects of active stiffness control on the aeroelastic behavior were also investigated. Different stiffness levels induced in each bimorph changed the flutter behavior. Negative DC input voltages to the MFCs increased the cut in speed for LCOs. On the other hand, the amplitude of LCOs at higher airflow speeds was reduced due to positive DC input voltages. Therefore, the active stiffness control can be used to modify the cut in speed of LCOs as well as to modify the amplitude of LCOs. As future work, wind tunnel tests should be performed in order to verify the numerical predictions presented in this dissertation. Moreover, in addition to the aeroelastic control case explored in this work, out of phase DC actuation of the MFCs should be investigated as a morphing wing (or adaptive geometry) technique. In order to induce optimized aerodynamic shapes due to the MFCs actuation, one should consider the use of MFCs actuators as a way to keep certain shapes induced by aerodynamic loads at different airflow speeds. Furthermore, the double bimorph configuration explored in this work could be employed for flapping wing cases to mimic the behavior of birds or insects.

References

ABDELKEFI, A.; HAJJ, M. R. Performance enhancement of wing-based piezoaeroelastic energy harvesting through freeplay nonlinearity. *Theoretical and Applied Mechanics Letters*, v. 3, n. 4, p. 41001, 2013. ISSN 2095-0349. Disponível em: <http://www.sciencedirect.com/science/article/pii/S2095034915302439>.

ABDELKEFI, A.; NAYFEH, A. H.; HAJJ, M. R. Design of piezoaeroelastic energy harvesters. *Nonlinear Dynamics*, v. 68, n. 4, p. 519–530, jun 2012. ISSN 1573-269X. Disponível em: <https://doi.org/10.1007/s11071-011-0233-x>.

ABDELKEFI, A.; NAYFEH, A. H.; HAJJ, M. R. Effects of nonlinear piezoelectric coupling on energy harvesters under direct excitation. *Nonlinear Dynamics*, v. 67, n. 2, p. 1221–1232, jan 2012. ISSN 0924-090X. Disponível em: <http://link.springer.com/10.1007/s11071-011-0064-9>.

ABDELKEFI, A.; NAYFEH, A. H.; HAJJ, M. R. Global nonlinear distributed-parameter model of parametrically excited piezoelectric energy harvesters. *Nonlinear Dynamics*, v. 67, n. 2, p. 1147–1160, jan 2012. ISSN 0924-090X. Disponível em: <http://link.springer.com/10.1007/s11071-011-0059-6>.

ABDELKEFI, A.; NAYFEH, A. H.; HAJJ, M. R. Modeling and analysis of piezoaeroelastic energy harvesters. *Nonlinear Dynamics*, v. 67, n. 2, p. 925–939, jan 2012. ISSN 1573-269X. Disponível em: <https://doi.org/10.1007/s11071-011-0035-1>.

ALBANO, E.; RODDEN, W. P. A doublet-lattice method for calculating lift distributions on oscillating surfaces in subsonic flows. *AIAA Journal*, American Institute of Aeronautics and Astronautics, v. 7, n. 2, p. 279–285, feb 1969. ISSN 0001-1452. Disponível em: <https://arc.aiaa.org/doi/abs/10.2514/3.5086>.

AURELLE, N.; GUYOMAR, D.; RICHARD, C.; GONNARD, P.; EYRAUD, L. Nonlinear behavior of an ultrasonic transducer. *Ultrasonics*, v. 34, n. 2-5, p. 187–191, jun 1996. ISSN 0041624X. Disponível em: <http://linkinghub.elsevier.com/retrieve/pii/0041624X9500077G>.

BAE, J. S.; INMAN, D. J. Aeroelastic characteristics of linear and nonlinear piezo-aeroelastic energy harvester. *Journal of Intelligent Material Systems and Structures*, v. 25, n. 4, p. 401–416, 2014. Disponível em: <https://doi.org/10.1177/1045389X13498312>.

BHATTI, M. A. *Fundamental Finite Element Analysis and Applications: With Mathematica and Matlab Computations*. 1. ed. [S.l.]: John Wiley & Sons, 2005. ISBN 9780471648086.

BISPLINGHOFF, R. L.; ASHLEY, H.; HALFMAN, R. L. *Aeroelasticity*. Dover Publications, 1996. (Dover Books on Aeronautical Engineering Series). ISBN 9780486691893. Disponível em: <https://books.google.com.br/books?id=jtqDQ2nTvvcC>.

BOUTET, J.; DIMITRIADIS, G. Unsteady Lifting Line Theory Using the Wagner Function for the Aerodynamic and Aeroelastic Modeling of 3D Wings. *Aerospace*, v. 5, p. 92, 2018.

BRUNI, C.; GIBERT, J.; FRULLA, G.; CESTINO, E.; MARZOCCA, P. Energy harvesting from aeroelastic vibrations induced by discrete gust loads. *Journal of Intelligent Material Systems and Structures*, v. 28, n. 1, p. 47–62, 2017. ISSN 15308138.

CASTRO, B. A. de; BRUNINI, D. de M.; BAPTISTA, F. G.; ANDREOLI, A. L.; ULSON, J. A. C. Assessment of Macro Fiber Composite Sensors for Measurement of Acoustic Partial Discharge Signals in Power Transformers. *IEEE Sensors Journal*, v. 17, n. 18, p. 6090–6099, 2017. ISSN 1530-437X.

COBB, R.; BROWNING, J.; CANFIELD, R.; MILLER, S. F-16 Ventral Fin Buffet Alleviation Using Piezoelectric Actuators. In: *50th AIAA/ASME/ASCE/AHS/ASC Structures, Structural Dynamics, and Materials Conference*. Reston, Virigina: American Institute of Aeronautics and Astronautics, 2009. ISBN 978-1-60086-975-4. Disponível em: <http://arc.aiaa.org/doi/10.2514/6.2009-2538>.

COMSTOCK, R. H. Charge control of piezoelectric actuators to reduce hysteresis effects. n. 19, 1979. Disponível em: <https://patents.google.com/patent/US4263527A/en>.

CRISFIELD, M. A. *Non-Linear Finite Element Analysis of Solids and Structures: Advanced Topics*. 1st. ed. New York, NY, USA: John Wiley & Sons, Inc., 1997. ISBN 047195649X.

De Marqui Junior, C.; ERTURK, A.; INMAN, D. J. Piezoaeroelastic Modeling and Analysis of a Generator Wing with Continuous and Segmented Electrodes. *Journal of Intelligent Material Systems and Structures*, v. 21, n. 10, p. 983–993, jul 2010. ISSN 1045-389X. Disponível em: <http://journals.sagepub.com/doi/10.1177/1045389X10372261>.

DERAEMAEKER, A.; NASSER, H.; BENJEDDOU, A.; PREUMONT, A. Mixing Rules for the Piezoelectric Properties of Macro Fiber Composites. *Journal of Intelligent Material Systems and Structures*, v. 20, n. 12, p. 1475–1482, aug 2009. ISSN 1045-389X. Disponível em: <http://journals.sagepub.com/doi/10.1177/1045389X09335615>.

DIAS, J. A. C.; JUNIOR, C. D. M.; ERTURK, A. Hybrid piezoelectric-inductive flow energy harvesting and dimensionless electroaeroelastic analysis for scaling. *Applied Physics Letters*, v. 102, n. 4, p. 044101, jan 2013. ISSN 0003-6951. Disponível em: <http://aip.scitation.org/doi/10.1063/1.4789433>.

DIMITRIADIS, G. *Introduction to Nonlinear Aeroelasticity*. Wiley, 2017. (Aerospace Series). ISBN 9781118613474. Disponível em: <https://books.google.com.br/books?id=pelcvgAACAAJ>.

DOWELL, E. H.; TANG, D. Nonlinear Aeroelasticity and Unsteady Aerodynamics. *AIAA Journal*, v. 40, n. 9, p. 1697–1707, 2002. ISSN 0001-1452. Disponível em: <http://arc.aiaa.org/doi/10.2514/2.1853>.

DUNNMON, J. A.; STANTON, S. C.; MANN, B. P.; DOWELL, E. H. Power extraction from aeroelastic limit cycle oscillations. *Journal of Fluids and Structures*, v. 27, n. 8, p. 1182–1198, 2011. ISSN 08899746.

ERTURK, A.; VIEIRA, W. G. R.; JUNIOR, C. D. M.; INMAN, D. J. On the energy harvesting potential of piezoaeroelastic systems. *Applied Physics Letters*, v. 96, n. 18, 2010. ISSN 00036951.

GOLDSCHMIDTBOEING, F.; EICHHORN, C.; WISCHKE, M.; KROENER, M.; WOIAS, P. The influence of ferroelastic hysteresis on mechanically excited PZT cantilever beams. *PowerMEMS*, p. 114–117, 2011.

HARDER, R. L.; DESMARAIS, R. N. Interpolation using surface splines. *Journal of Aircraft*, American Institute of Aeronautics and Astronautics, v. 9, n. 2, p. 189–191, feb 1972. ISSN 0021-8669. Disponível em: <https://doi.org/10.2514/3.44330>.

HASSANI, V.; TJAHJOWIDODO, T.; DO, T. N. A survey on hysteresis modeling, identification and control. *Mechanical Systems and Signal Processing*, v. 49, n. 1-2, p. 209–233, dec 2014. ISSN 08883270. Disponível em: <https://linkinghub.elsevier.com/retrieve/pii/S0888327014001186>.

HU, Y.; XUE, H.; YANG, J.; JIANG, Q. Nonlinear behavior of a piezoelectric power harvester near resonance. *IEEE Transactions on Ultrasonics, Ferroelectrics and Frequency Control*, v. 53, n. 7, p. 1387–1391, jul 2006. ISSN 0885-3010. Disponível em: <http://ieeexplore.ieee.org/document/1665088/>.

HUDEK, M. *Modeling and control of a piezoelectric actuator for active and adaptive optics*. Tese (B.S. Thesis) — Czech Technical University, 2013. Disponível em: <https://support.dce.felk.cvut.cz/mediawiki/images/2/21/Bp_2013_hudec_marek.pdf>.

IEEE. IEEE Standard on Piezoelectricity. *ANSI/IEEE Std 176-1987*, p. 1–74, 1988.

JAVED, U.; DAI, H. L.; ABDELKEFI, A. Nonlinear dynamics and comparative analysis of hybrid piezoelectric-inductive energy harvesters subjected to galloping vibrations. *The European Physical Journal Special Topics*, v. 224, n. 14, p. 2929–2948, nov 2015. ISSN 1951-6401. Disponível em: <https://doi.org/10.1140/epjst/e2015-02599-y>.

JUNIOR, C. D. M.; TAN, D.; ERTURK, A. On the electrode segmentation for piezoelectric energy harvesting from nonlinear limit cycle oscillations in axial flow. *Journal of Fluids and Structures*, v. 82, p. 492–504, 2018. ISSN 0889-9746. Disponível em: <http://www.sciencedirect.com/science/article/pii/S0889974618300628>.

JUNIOR, C. D. M.; VIEIRA, W. G. R.; ERTURK, A.; INMAN, D. J. Modeling and Analysis of Piezoelectric Energy Harvesting From Aeroelastic Vibrations Using the Doublet-Lattice Method. *Journal of Vibration and Acoustics*, v. 133, n. 1, p. 011003, 2011. ISSN 07393717. Disponível em: <http://vibrationacoustics.asmedigitalcollection.asme.org/article.aspx?articleid=1471531>.

KARMAN, T. V. *Festigkeitsprobleme im maschinenbau*. Leipzig: [publisher not identified], 1910.

KOVALOVS, A.; BARKANOV, E.; GLUHIHS, S. Active twist of model rotor blades with D-spar design. *Transport*, Taylor & Francis, v. 22, n. 1, p. 38–44, 2007. Disponível em: <https://www.tandfonline.com/doi/abs/10.1080/16484142.2007.9638094>.

KUSHNIR, U.; RABINOVITCH, O. Advanced Ferroelectric MFC Actuators: The Effect of Ferro-Elastic Domain Switching. In: *Volume 1: Advanced Energy Systems; Advanced and Digital Manufacturing; Advanced Materials; Aerospace*. ASME, 2008. p. 595–600. ISBN 978-0-7918-4835-7. Disponível em: <http://proceedings.asmedigitalcollection.asme.org/proceeding.aspx?articleid=1636576>.

LEADENHAM, S.; ERTURK, A. Unified nonlinear electroelastic dynamics of a bimorph piezoelectric cantilever for energy harvesting, sensing, and actuation. *Nonlinear Dynamics*, v. 79, n. 3, p. 1727–1743, feb 2015. ISSN 0924-090X. Disponível em: <http://link.springer.com/10.1007/s11071-014-1770-x>.

MAHMOODI, S. N.; JALILI, N.; DAQAQ, M. F. Modeling, Nonlinear Dynamics, and Identification of a Piezoelectrically Actuated Microcantilever Sensor. *IEEE/ASME Transactions on Mechatronics*, v. 13, n. 1, p. 58–65, feb 2008. ISSN 1083-4435. Disponível em: <http://ieeexplore.ieee.org/document/4453927/>.

MATT, H. M.; SCALEA, F. L. di. Macro-fiber composite piezoelectric rosettes for acoustic source location in complex structures. *Smart Materials and Structures*, v. 16, n. 4, p. 1489–1499, aug 2007. ISSN 0964-1726. Disponível em: <http://stacks.iop.org/0964-1726/16/i=4/a=064?key=crossref.31e314c2e7645715b16873011973531f>.

MAUGIN, G. A. *Nonlinear Electromechanical Effects and Applications*. WORLD SCIENTIFIC, 1986. (Series in Theoretical and Applied Mechanics, v. 1). ISBN 978-9971-978-43-3. Disponível em: <https://www.worldscientific.com/worldscibooks/10.1142/0165>.

MICHELIN, S.; DOARÉ, D. Energy harvesting efficiency of piezoelectric flags in axial flows. *Journal of Fluid Mechanics*, v. 714, p. 489–504, 2013. ISSN 00221120.

MUDUPU, V.; TRABIA, M. B.; YIM, W.; WEINACHT, P. Design and validation of a fuzzy logic controller for a smart projectile fin with a piezoelectric macro-fiber composite bimorph actuator. *Smart Materials and Structures*, v. 17, n. 3, p. 035034, jun 2008. ISSN 0964-1726. Disponível em: <http://stacks.iop.org/0964-1726/17/i=3/a=035034?key=crossref.d6751570806282a7ad07da04df28dd3d>.

NAYFEH, A.; MOOK, D. *Nonlinear Oscillations*. Wiley, 2008. (Wiley Classics Library). ISBN 9783527617593. Disponível em: <https://books.google.com.br/books?id=sj3ebg7jRaoC>.

REDDY, J. N. *Energy Principles and Variational Methods in Applied Mechanics*. Wiley, 2002. ISBN 9780471179856. Disponível em: <https://books.google.com.br/books?id=3gw5rxLQdaQC>.

ROGER, K. L. Airplane Math Modeling Methods for Active Control Design. *AGARD-CP-228*, p. 4.1–4.11, 1977. Disponível em: <https://ci.nii.ac.jp/naid/10003115109/en/>.

SALINAS, D.; KWON, Y.; RITTER, B. A study of linearisation techniques in nonlinear FEM. *Mathematical Modelling and Scientific Computing*, v. 1, n. 5, p. 480–493, 1993.

SAMUR, A. *Flexible Piezoelectric Composites and Concepts for Bio-inspired Dynamic Bending-twisting Actuation*. Tese (Thesis) — Georgia Institute of Technology, 2013. Disponível em: <https://books.google.com.br/books?id=97ApnQAACAAJ>.

SHAHAB, S.; ERTURK, A. Coupling of experimentally validated electroelastic dynamics and mixing rules formulation for macro-fiber composite piezoelectric structures. *Journal of Intelligent Material Systems and Structures*, v. 28, n. 12, p. 1575–1588, 2017. Disponível em: <https://doi.org/10.1177/1045389X16672732>.

SHI, Y.; HALLETT, S. R.; ZHU, M. Energy harvesting behaviour for aircraft composites structures using macro-fibre composite: Part I - Integration and experiment. *Composite Structures*, Elsevier, v. 160, p. 1279–1286, jan 2017. ISSN 0263-8223. Disponível em: <https://www.sciencedirect.com/science/article/pii/S0263822316321377>.

SHINDO, Y.; NARITA, F.; SATO, K.; TAKEDA, T. Nonlinear electromechanical fields and localized polarization switching of piezoelectric macrofiber composites. *Journal of Mechanics of Materials and Structures*, v. 6, n. 7-8, p. 1089–1102, dec 2011. ISSN 1559-3959. Disponível em: <http://msp.org/jomms/2011/6-7/p10.xhtml>.

SILVA, T. M. P.; JUNIOR, C. D. M. Energy analysis of semi-passive control for an aeroelastic plate-like wing using shunted piezoelectric materials. *Journal of Intelligent Material Systems and Structures*, v. 27, n. 19, p. 2599–2615, 2016. Disponível em: <https://doi.org/10.1177/1045389X16635842>.

SMITH, R. C.; OUNAIES, Z. A Domain Wall Model for Hysteresis in Piezoelectric Materials. *Journal of Intelligent Material Systems and Structures*, v. 11, n. 1, p. 62–79, jan 2000. ISSN 1045-389X. Disponível em: <http://journals.sagepub.com/doi/10.1106/HPHJ-UJ4D-E9D0-2MDY>.

SMITH, R. C.; SEELECKE, S.; DAPINO, M.; OUNAIES, Z. A unified framework for modeling hysteresis in ferroic materials. *Journal of the Mechanics and Physics of Solids*, v. 54, n. 1, p. 46–85, 2006. ISSN 0022-5096. Disponível em: <http://www.sciencedirect.com/science/article/pii/S0022509605001456>.

SODANO, H. A.; PARK, G.; INMAN, D. J. An investigation into the performance of macro-fiber composites for sensing and structural vibration applications. *Mechanical Systems and Signal Processing*, v. 18, n. 3, p. 683–697, 2004. ISSN 0888-3270. Disponível em: <http://www.sciencedirect.com/science/article/pii/S0888327003000815>.

SOUSA, V. C.; De M Anicézio, M.; JUNIOR, C. D. M.; ERTURK, A. Enhanced aeroelastic energy harvesting by exploiting combined nonlinearities: Theory and experiment. *Smart Materials and Structures*, v. 20, n. 9, 2011. ISSN 09641726.

SOUSA, V. C. D.; JUNIOR, C. D. M. Airfoil-based piezoelectric energy harvesting by exploiting the pseudoelastic hysteresis of shape memory alloy springs. *Smart Materials and Structures*, IOP Publishing, v. 24, n. 12, p. 125014, 2015. ISSN 1361665X. Disponível em: <http://dx.doi.org/10.1088/0964-1726/24/12/125014>.

STANTON, S. C.; ERTURK, A.; MANN, B. P.; INMAN, D. J. Nonlinear piezoelectricity in electroelastic energy harvesters: Modeling and experimental identification. *Journal of Applied Physics*, v. 108, n. 7, p. 074903, oct 2010. ISSN 0021-8979. Disponível em: <http://aip.scitation.org/doi/10.1063/1.3486519>.

STANTON, S. C.; ERTURK, A.; MANN, B. P.; INMAN, D. J. Resonant manifestation of intrinsic nonlinearity within electroelastic micropower generators. *Applied Physics Letters*, v. 97, n. 25, p. 254101, dec 2010. ISSN 0003-6951. Disponível em: <http://aip.scitation.org/doi/10.1063/1.3530449>.

TAN, D.; YAVAROW, P.; ERTURK, A. Resonant nonlinearities of piezoelectric macro-fiber composite cantilevers with interdigitated electrodes in energy harvesting. *Nonlinear*

Dynamics, v. 92, n. 4, p. 1935–1945, jun 2018. ISSN 0924-090X. Disponível em: <http://link.springer.com/10.1007/s11071-018-4172-7>.

TANG, L.; PAÏDOUSSIS, M. P.; JIANG, J. Cantilevered flexible plates in axial flow: Energy transfer and the concept of flutter-mill. *Journal of Sound and Vibration*, v. 326, n. 1-2, p. 263–276, 2009. ISSN 0022460X.

THEODORSEN, T. *General theory of aerodynamic instability and the mechanism of flutter*. 1935. 24 p.

TIERSTEN, H. F. Electroelastic equations for electroded thin plates subject to large driving voltages. *Journal of Applied Physics*, v. 74, n. 5, p. 3389–3393, sep 1993. ISSN 0021-8979. Disponível em: <http://aip.scitation.org/doi/10.1063/1.354565>.

WAGNER, U. V.; HAGEDORN, P. Piezo-beam systems subjected to weak electric field: experiments and modelling of non-linearities. *Journal of Sound and Vibration*, v. 256, n. 5, p. 861–872, oct 2002. ISSN 0022460X. Disponível em: <http://linkinghub.elsevier.com/retrieve/pii/S0022460X02950248>.

WANG, Y.; INMAN, D. J. Composites With Simultaneous Vibration Control , Energy Harvesting and Self-Sensing Capabilities. *Proceedings of the 18th International Conference on Composite Materials (ICCM)*, 2011.

WILLIAMS, R. B. Nonlinear Mechanical and Actuation Characterization of Piezoceramic Fiber Composites. *Assembly*, PhD, p. 1–361, 2004. Disponível em: <http://scholar.lib.vt.edu/theses/available/etd-04052004-095526/>.

WOLF, K.; GOTTLIEB, O. *Nonlinear dynamics of a cantilever beam actuated by piezoelectric layers in symmetric and asymmetric configuration*. [S.l.: s.n.], 2001.

XIANG, J.; WU, Y.; LI, D. Energy harvesting from the discrete gust response of a piezoaeroelastic wing: Modeling and performance evaluation. *Journal of Sound and Vibration*, v. 343, p. 176–193, 2015. ISSN 10958568.

YANG, Y.; TANG, L.; LI, H. Vibration energy harvesting using macro-fiber composites. *Smart Materials and Structures*, v. 18, n. 11, p. 115025, nov 2009. ISSN 0964-1726. Disponível em: <http://stacks.iop.org/0964-1726/18/i=11/a=115025?key=crossref.b1e4f021eabfb570dcc41eeb088859c8>.

ZHAO, L.; HUANG, Q.; DENG, X.; SANE, S. P. Aerodynamic effects of flexibility in flapping wings. *Journal of The Royal Society Interface*, v. 7, n. 44, p. 485–497, 2010.

ZHOU, J.; XU, M.; YANG, Z. Aeroelastic stability analysis of curved composite panels with embedded Macro Fiber Composite actuators. *Composite Structures*, v. 208, p. 725–734, 2019. ISSN 0263-8223. Disponível em: <http://www.sciencedirect.com/science/article/pii/S0263822318334949>.

ZIENKIEWICZ, O. C.; TAYLOR, R. L. *The Finite Element Method*. Butterworth-Heinemann, 2000. (Fluid Dynamics). ISBN 9780750650557. Disponível em: <https://books.google.com.br/books?id=wmDQ_3qzvmIC>.

ZIPPO, A.; FERRARI, G.; AMABILI, M.; BARBIERI, M.; PELLICANO, F. Active vibration control of a composite sandwich plate. *Composite Structures*, v. 128, p. 100–114, 2015. ISSN 0263-8223. Disponível em: <http://www.sciencedirect.com/science/article/pii/S026382231500210X>.

APPENDIX A - Newton Raphson Method

To solve the nonlinear system presented, it is necessary to adopt a linearization method. As an initial approach, the set of equations is solved using the classical linearization method (SALINAS; KWON; RITTER, 1993). The method consists of taking as initial approximation the linear matrices from the system as initial approximation. With the displacements, new secant stiffness matrix are obtained and the system can be evaluated until the system converges. In order to increase the speed of convergence of the system Newton Raphson's method is used, where after the first iteration with the secant stiffness matrix, the other iterations occur with the tangent stiffness matrix. The process is represented in fig. 50.

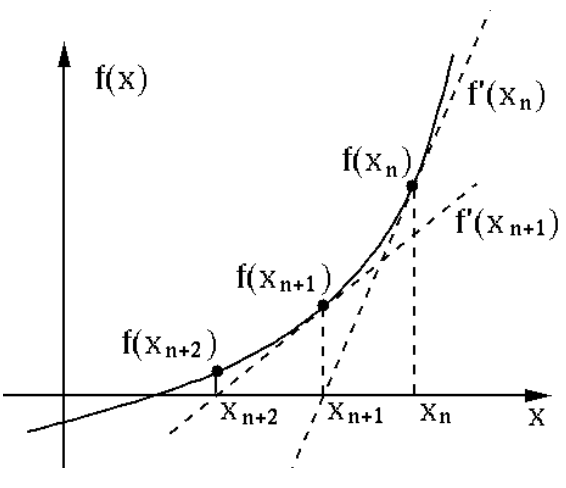

Figure 50 – Newton Raphson method.

The method consists in an iterative algorithm to solve a set of nonlinear equations.

$$x_{n+1} = x_n - \frac{\mathrm{f}(\mathrm{x_n})}{\mathrm{f}'(\mathrm{x_n})} \tag{A.1}$$

where the subscripts indicate the iteration count. Basically the equation is obtained through the linearization:

$$f(x_{n+1}) - f(x_n) = f'(x_n)(x_{n+1} - x_n) \tag{A.2}$$

The main goal is to seek the roots of the equation ($f(x) = 0$). As eq. A.2 is an approximation, successive Newton Raphson iterations yields to better approximation to the solution. The iteration is geometrically represented in fig. 50. Since the solution is approximated, a tolerance is set to check system convergence.

The Newton-Raphson algorithm will converge quadratically if the functions have continuous first derivatives in the neighborhood of the solution. The method is also sensitive to the behavior of the function $f(x)$ and sometimes can diverge. The more linear the function is, the more rapidly and reliably Newton's method converges.

APPENDIX B - Mixing Rules for MFCs

Figure 51(a) shows the electric field for a d_{33} mode MFC with interdigitated electrodes. For this type of piezocomposites, although the electric field lines do not have a constant direction (Figure 51(a)), it is reasonable to consider that the poling direction is the same of the fibers (length direction), and that the electric field is in the same direction.

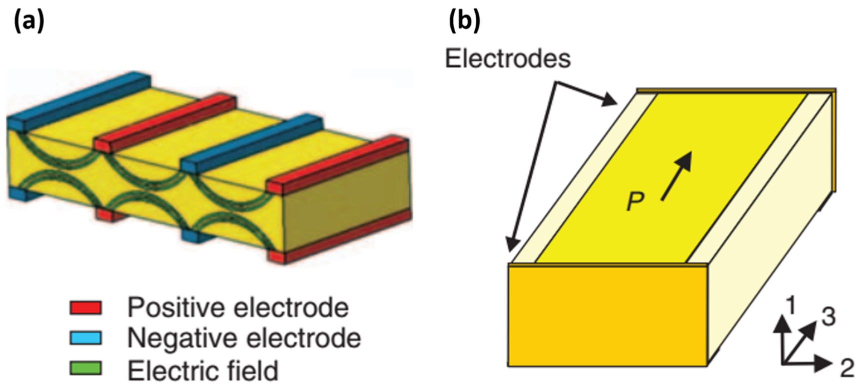

Figure 51 – (a) Electric field distribution and (b) representative volume element (RVE) for a d_{33} mode MFC.

Considering the superscript m and p for the matrix and piezoceramic fibers elements, respectively and the subscripts L and T for the longitudinal and transverse direction, respectively (3 and 2 in Figure 51(b)) the equivalent mechanical properties can be defined as:

$$E_L = \rho E_L^p + (1-\rho) E_L^m \tag{B.1}$$

$$\frac{1}{E_T} = \frac{\rho}{E_T^p} + \frac{1-\rho}{E_T^m} \tag{B.2}$$

$$\upsilon_{LT} = \rho\,\upsilon^p_{LT} + (1-\rho)\,\upsilon^m_{LT} \tag{B.3}$$

$$\frac{1}{G_{LT}} = \frac{\rho}{G^p_{LT}} + \frac{1-\rho}{G^m_{LT}} \tag{B.4}$$

The equivalent piezoelectric properties are defined as:

$$d_{33} = \frac{1}{E_L}\left(\rho d^p_{33} E^p_L\right) \tag{B.5}$$

$$d_{32} = -d_{33}\,\upsilon_{LT} + \rho\left(d^p_{32} + d^p_{33}\,\upsilon^p_{LT}\right) \tag{B.6}$$

$$\varepsilon^{\mathrm{T}}_{33} = \rho\,\varepsilon^{\mathrm{T}p}_{33} + (1-\rho)\,\varepsilon^{\mathrm{Tm}}_{33} \tag{B.7}$$

where E is young modulus, G the transverse modulus, ρ the volume fraction of fibers, υ is the poisson's ratio, d is the piezoelectric charge constant and ε the dieletric constant.

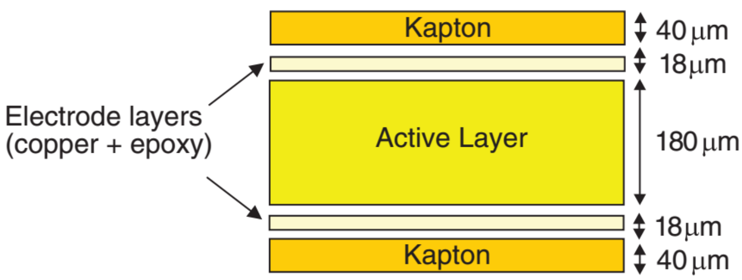

Figure 52 – Sequence of layers for the MFC (data provided by Smart Material).

Figure 52 shows the sequence of layers for a MFC (approximate data provided by manufacturer Smart Material and Williams (2004)). The dimensions shown are used to calculate the equivalent mechanical properties at each layer as well as the representative volume element (RVE) showed in Figure 51(b). Considering the model proposed presented in this appendix based on the plane-stress assumption, the properties obtained for the active area of the MFC are shown in table 3.

Table 3 – Properties of representative volume element (RVE - layer with piezoceramic fibers), electrode layer, passive layer (kapton) and d_{33}-mode MFCs using analytical mixing rules formulation (DERAEMAEKER et al., 2009).

Property	RVE	Electrode	Kapton	MFC
E_1 $[Pa]$	43.78×10^9	30.48×10^9	2.8×10^9	27.87×10^9
E_2 $[Pa]$	20.45×10^9	4.05×10^9	2.8×10^9	16.89×10^9
G_{12} $[Pa]$	7.35×10^9	1.49×10^9	1.04×10^9	4.94×10^9
ν_{12}	0.31	0.34	0.34	0.32
ν_{21}	0.15	0.045	0.34	0.18
ρ $[Kg/m^3]$	6859	2964	1420	4915